UNIVERSITY OF CALIFORNIA, SAN DIEGO

Photoelectrodes Using Low Cost and Earth Abundant Materials for Practical Photoelectrochemical (PEC) Water Splitting

A dissertation submitted in partial satisfaction of the

requirements for the degree Doctor of Philosophy

in

Materials Science and Engineering

by

Sun Young Noh

Committee in Charge:

Professor Deli Wang, Chair
Professor Sungho Jin, Co-Chair
Professor Renkun Chen
Professor Shadi Dayeh
Professor Ratnesh Lal

2014

The dissertation of Sun Young Noh is approved, and it is acceptable in quality and form for publication on microfilm:

Co-Chair

Chair

University of California, San Diego

2014

DEDICATION

Dedicated to my loving family and Billy

who have always shown unfailing love and support

TABLE OF CONTENTS

LIST OF FIGURES

ACKNOWLEDGEMENTS

I would like to express my heartfelt gratitude to Professor Deli Wang for giving the opportunity to join and work in his group and encouraging and supporting me in the right direction as the chair of my committee. Particularly, I would like to thank him for sharing his vision and thoughts which always inspire me.

I am truly grateful to Professor Sungho Jin for providing me all the valuable suggestions with an enjoyable conversation and discussion as my co-advisor. I appreciate helpful discussions and suggestions on my dissertation I received from all the committee members, Professor Ratnesh Lal, Professor Renkun Chen, and Professor Shadi Dayeh.

Also, I would like to thank all my former and present Wang group members who are my colleagues as well as good friends. In particular, I am truly grateful to Dr. Ke Sun for being a reliable friend and giving me the indispensable foundation of my studies on PEC water splitting projects. Without his help, I would not have been able to succeed. I am also thankful to Namseok Park for teaching me using the Nano3 facilities and giving me strong support both physically and mentally/spiritually.

I would truly like to thank my wonderful friends who are like family and made this incredible journey possible: Jaeyun Moon, Dr. Chulmin Choi, Dr. Yongsung Hwang, Dr. Younghak Park, Geuntak Lee, Sejung Kim, Guipeun Kang, Sungje Byun, Jungok Choi, Esther Chun, Asuelim Kim, Joohwan Kim, Hyojung Yoon, Kimoon Um, Sungwoon Kim, Jihye Bak, Jeanne Khamwannah, Cyrus Rustomji, Micheal Frank, Changshin-dong old friends, Konkuk Univ. queens, and KIST old teammates for their prayer and friendship.

Lastly, I would like to express my deepest gratitude and love to my lover, Billy Chun, and my family, especially my mom for their unfailing love, support, and prayer.

Chapter 2, in full, is currently being prepared for submission for publication of the Journal of Physical Chemistry C. Sun Young Noh, Ke Sun, Shaohua Shen, Sung J. Kim, Xiaoqing Pan, Sungho Jin, and Deli Wang. The dissertation author was the primary researcher and the first author of this paper.

Chapter 3, in full, is a reprint of the material as it appears in Nano Energy, Volume 2, 2013. Sun Young Noh, Ke Sun, Chulmin Choi, Mutong Niu, Ke Xu, Muchuan Yang, Sungho Jin, and Deli Wang. The dissertation author was the primary researcher and first author of this paper.

Chapter 4, in full, is currently being prepared for submission for publication of Energy & Environmental Science. Sun Young Noh, Chulmin Choi, Yuanyuan Chen, Sungho Jin, and Deli Wang. The dissertation author was the primary researcher and first author of this paper.

Chapter 5, in full, is currently being prepared for submission for publication of Energy & Environmental Science. Sun Young Noh, Namseok Park, Li Chen, Zhaowei Liu, and Deli Wang. The dissertation author was the primary researcher and first author of this paper.

VITA

2005	Bachelor of Science in Textile Engineering, Konkuk University, Korea
2007	Master of Science in Textile Engineering, Konkuk University, Korea
2014	Doctor of Philosophy in Materials Science and Engineering, University of California, San Diego

LIST OF PUBLICATIONS

1. **Sun Young Noh**, Namseok Park, Li Chen, Zhaowei Liu, and Deli Wang, "Systematic Study of Metal Enabled Si Photocathodes for Efficient Photoelectrochemical Cells", *Energy Environ. Sci.*, 2014, in preparation

2. **Sun Young Noh**, Chulmin Choi, Yuanyuan Chen, Sungho Jin, and Deli Wang, "Metal-Si and Metal-Insulator-Si photoanodes for efficient photoelectro-chemical cells", *Energy Environ. Sci.*, 2014, in preparation

3. **Sun Young Noh**, Ke Sun, Shaohua Shen, Sung J. Kim, Xiaoqing Pan, Sungho Jin, and Deli Wang, "Photoelectrochemical Water Splitting Performance of Post Growth treated TiO_2 Nanowires", *J. Phys. Chem. C*, 2014, in preparation

4. Ke Sun, Shaohua Shen, Justin Cheung, Xiaolu Pang, Namseok Park, Jigang Zhou, Yongfeng Hu, Zhelin Sun, **Sun Young Noh**, Riley T. Conor, Paul Yu, Sungho Jin, Deli Wang, "Si Photoanode Protected by Metal Modified ITO with Ultrathin NiOx for Solar Water Oxidation", ***Phys. Chem. Chem. Phys***., 2014, Accepted

5. Yanyan Zhang, Jirapon Khamwannah, **Sun Young Noh**, Haibin Yang, Sungho Jin, "Improved Dye Sensitized Solar Cell Performance in Larger Cell Size by Using TiO_2 Nanotubes", ***Nanotechnology,*** 24, 045401 (2013).

6. Hyunsu Kim, Chulmin Choi, Jirapon Khamwannah, **Sun young Noh**, Yanyan Zhang, Tae-Yeon Seong and Sungho Jin, "Plasmonic Au nanoparticles on 8nm TiO_2 nanotubes for enhanced photocatalytic water splitting", ***J. Renewable Sustainable Energy***, 5, 053104 (2013)

7. **Sun Young Noh**, Ke Sun, Chulmin Choi, Mutong Niu, Ke Xu, Muchuan Yang, Sungho Jin, and Deli Wang, "Branched TiO2/Si Nanostructures for Enhanced Photoelectrochemical Water Splitting", ***Nano Energy***, 2, 351 (2013)

8. Jirapon Khamwannah, **Sun Young Noh**, Christine Frandsen, Yanyan Zhang, Hyunsu Kim, Seong Deok Kong, and Sungho Jin, "Nanocomposites of TiO_2 and double-walled carbon nanotubes for improved dye-sensitized solar cells", ***J. Renewable Sustainable Energy,*** 4, 023116 (2012)

9. Jirapon Khamwannaha, Yanyan Zhang, **Sun Young Noh**, Hyunsu Kim, Christine Frandsen, Seong Deok Kong, Sungho Jin, "Enhancement of dye-sensitized solar cell efficiency by composite TiO_2 nanoparticle/8nmTiO_2 nanotube paper-like photoelectrode", ***Nano Energy***, 1, 411 (2012)

10. Ke Sun, Namseok Park, Zhelin Sun, Jigang Zhou, Jian Wang, Xiaolu Pang, Shaohua Shen, **Sun Young Noh**, Yi Jing, Sungho Jin, Paul Yu, and Deli Wang, "Nickel oxide functionalized silicon for efficient photo-oxidation of water", ***Energy Environ. Sci.***, 5, 7872 (2012)

ABSTRACT OF THE DISSERTATION

Photoelectrodes Using Low Cost and Earth Abundant Materials for Practical Photoelectrochemical (PEC) Water Splitting

by

Sun Young Noh

Doctor of Philosophy in Materials Science and Engineering

University of California, San Diego, 2014

Professor Deli Wang, Chair

Professor Sungho Jin, Co-Chair

It is believed that the solar energy is the ultimate clean energy source to meet global human energy consumption demand. However, the harvesting of solar energy in a clean and sustainable fashion and the storage and transport of the electricity could be challenges precluding practical scaling up of solar energy applications. Photoelectrochemical (PEC) water splitting using semiconducting materials is the most

attractive approach of the solar energy applications because it efficiently converts solar energy, with high efficacy, to storable and transportable hydrogen fuel through an environmentally benign process (reaction with water and with hydrocarbon and oxygen as by-products). However, the good chemical and electrochemical stability and high overall energy conversion efficiency, in addition to low cost, are current challenges for the use of large scale PEC for practical and sustainable solar fuel production.

The focus of this thesis is to develop economically competitive and efficient PEC water splitting cells by selecting low cost and earth abundant semiconductors and developing cheap and facile scalable processing for photoelectrode fabrication. Two systems, three dimensional branched nanowire heterostructures and metal coating enabled planar Si structures, are studied in details.

This dissertation is structured in the following: after a briefly introduction of the principle of photoelectrochemical (PEC) water splitting cells in chapter 1, TiO2 nanowires and TiO_2/Si branched nanostructures are discussed in chapters 2 and 3. As a low cost material, TiO_2 nanowire structure is prepared by a hydrothermal method and further modified by different post growth treatments to improve light absorption and kinetic properties and investigated their effects on PEC water splitting performances. The results show that types and sequences of post growth treatments should be carefully considered to improve the properties and performances of TiO_2 NWs. Also, hierarchically heterogeneous integrated TiO_2/Si nanostructures such as core/shell and multibranched nanowire structures are fabricated by a combination of nanoimprint lithography, reactive ion etch, and hydrothermal reactions. The structures have increased surface area for enhanced light absorption and more reaction sites and short diffusion

length of minority carriers for higher reaction rate. Their PEC performances and the associated charge transfer at heterojunction interface are studied showing that photo current of TiO_2/Si heterojunction structure is limited by the recombination at the TiO_2/Si junctions or the properties of TiO_2.

In chapter 4, metal-Si (MS) and metal-insulator-Si (MIS) structures, which have been studied in photovoltaic cells, are employed to developed cost-effective and efficient Si-based photoelectrodes. Earth abundant Ni film is selected as an oxygen evolution electrocatlayst for PEC photoanode, which can provide a junction voltage and protect Si surface, and applied to MS and MIS structures to compare their PEC performances and investigate the effects of insulating layer. Furthermore, MS and MIS structures are used to fabricate PEC photocathode with bimetal layer and the study is discussed in chapter 5. Bimetal layer can decouple catalytic reaction part from photovoltaic part. We design different patterned bimetal layers to improve the amount of light absorption of Si substrate and investigate the effects of MS or MIS contact, differently prepared insulator and bimetal thickness ratio on PEC water splitting performances.

Finally, a summary on the major accomplishments and perspectives on future improvements are presented in Chapter 6.

CHAPTER 1: Introduction

1.1 Principles of Photoelectrochemical (PEC) Water Splitting Cells

Currently most of the electricity is produced from fossil fuels. However, the fossil fuels not only have the cost issues due limited reserve but also contribute the largest amount of greenhouse gas and air pollution. Therefore, numerous organizations have been conducting advanced researches in the field of renewable energy. Among renewable energy resources, solar energy is by far the largest exploitable natural resource because the solar energy irradiating the surface of the Earth (1.3×10^5 TW) exceeds the current global human energy consumption (1.6×10^1 TW in 2010) [1]. However, to use the sun sustainably as the primary energy source, energy storage and transportation can be challenging isuues. One of the most attractive approaches is the photoelectrochemical (PEC) water splitting process, which efficiently converts solar energy to storable and transportable hydrogen fuel, due to its potential high efficiency, up to >30 % in principle, low cost, and environmental friendliness. [2] In addition, hydrogen can be readily converted into electricity with fuel cells and electrolyzers. Since the first practical demonstration of PEC water splitting using a TiO_2-based photocatalyst in the early 1970s [3], photocatalytic (PC) and PEC water splitting on semiconducting materials has been studied extensively [4-8]. In this section, a brief introduction to PEC water splitting cells will be given, including the PEC cell apparatus, PEC performance measurements setup, working mechanism, and photoelectrode requirements for efficient cell performances.

1.1.1 PEC water splitting cells and performance measurement setup

A basic PEC water splitting cell consists of a working electrode (p type semiconductor as photocathode, or n type semiconductor as photoanode), a counter electrode, a water-based electrolyte, and a reference electrode as shown in Figure 1.1. The PEC cell should have an optically transparent window (a quartz window) which allows the working electrode to be illuminated because normal glass shows a transmission cut-off below ~350 nm. Usually, electrical contact to the working electrode (sample) is made with a thin copper wire that is glued to the sample with silver paste. The backside and edges of the sample were protected using epoxy and the copper wire was sealed in plastic tubes to prevent electrical shorts to the electrolyte such that only the sample front side was in contact with the electrolyte. For the counter electrode, a common materials choice is Pt because of good chemical stability and a very small over-potential for hydrogen evolution (~0.1 V) to avoid performance limitations [9]. The surface area of the counter electrode should be preferably at least two times larger than the working electrode area, and both electrodes should face each other symmetrically to avoid inhomogeneous current densities at the working electrode. However, the latter requirement is less strict due to the modest voltage drop across the electrolyte solution with high electrolyte concentrations (typically >0.5 M). For the water-based electrolyte, supporting ions must be added so that the desired current flow can be attained because pure water is weakly conducting. The concentration of supporting ions should be sufficiently high to avoid large Ohmic voltage losses across the electrolyte. These Ohmic losses have to be compensated by increasing the applied bias potential, which adversely affects the overall efficiency of the photoelectrode. Also, the electrolyte should be

constantly purged with an inert gas such as argon or nitrogen and stirred with a magnetic stir bar to remove the evolved hydrogen and oxygen from the electrolyte solution then prevent the back-reaction of dissolved hydrogen and oxygen to water. In order to study the properties of the working electrode, a reference electrode is definitely necessary so that any change in the applied potential reflects a change in the working electrode alone because the overpotential at the counter electrode/electrolyte interface varies with the amount of current flowing through the cell. Applied potentials are nowadays usually reported against the RHE scale for water splitting studies because zero volt on the RHE scale reflects the H^+/H_2 redox potential in the actual solution, irrespective of the pH and a potential measured with respect to different reference electrodes can be easily converted to the RHE scale. Ag/AgCl chloride electrodes are most commonly used as reference electrodes but it is not stable under a basic condition (high pH). Therefore we should choose a suitable reference electrode depending on measurement conditions. Note that all reference electrodes are delicate then it should be well-maintained.

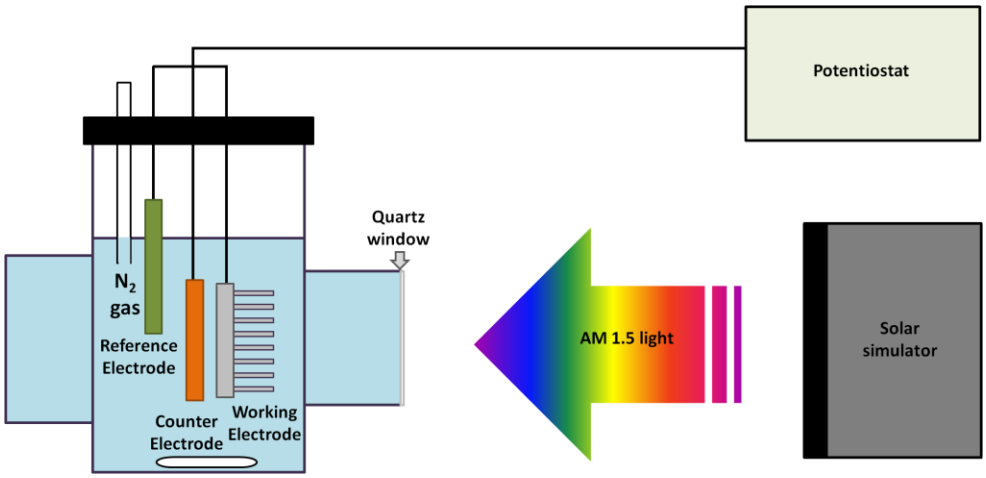

Figure 1.1 Schematic of a basic PEC water splitting cell.

The properties and PEC performance of the working electrodes are mainly investigated by two techniques such as current density vs potential (J-V) measurements and incident photon to charge carrier efficiency (IPCE) measurements. To provide a light source with the same intensity and spectral distribution, a solar simulator is employed and its intensity of 100mW/cm^2 corresponding to 1 sun at AM 1.5G should be verified at the sample position by a calibrated photodiode to compare device performances. Figure 1.2 shows solar irradiance and photon flux density spectrums of AM 1.5G.

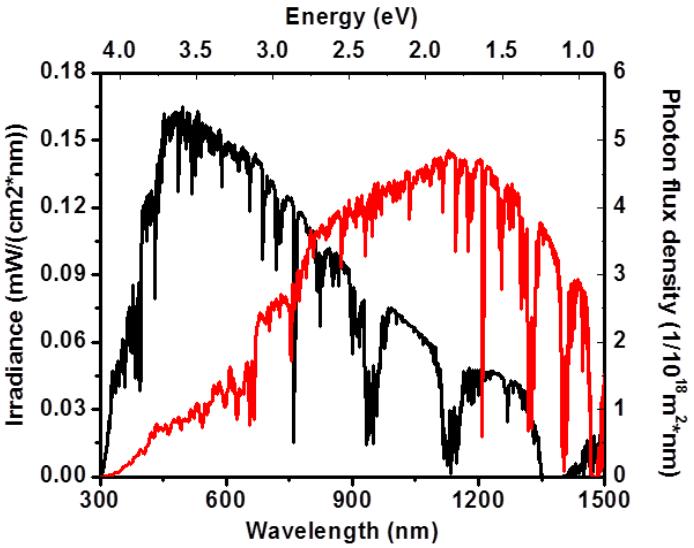

Figure 1.2 Solar irradiance and photon flux density spectrums.

J-V measurements are the most important technique to determine the performance characteristics of photoanodes or photocathodes for water splitting. J-V curves of the working electrode can be measured by a potentiostat which controls the potential of the photoelectrode and measures the current with three leads which are connected to the working, counter, and reference electrodes, respectively. From the J-V curve, anodic or cathodic current values can be distinguished through the sign of the photocurrent while a flatband potential or photocurrent onset potential can be obtained from a potential value which enables the separation of photogenerated electrons and holes leading to developing a photocurrent. However, a difference between flatband potential and onset potential is regularly several tenths of a volt due to recombination in the space charge layer, electron/hole trapping at surface defects, or electron/hole accumulation at the surface due to poor charge transfer kinetics [9]. Therefore, we generally use photocurrent onset potential for the potential value from the J-V curve. Also, the J-V curve can be recorded

under a chopped light, switching the light on and off with a shutter. This technique can help to accurately determine the photocurrent onset potential because it easily shows very small difference between dark current and photocurrent. Also, it can help to check if there is recombination of the photogenerated charge carriers via photocurrent transients under a chopped light. When the light is switched on and off, the photocurrent immediately rises/drops to its peak value and decays/increases to a steady-state value as part of the photogenerated charge carriers recombine due to accumulation or trapping of electrons or holes at surface states. Moreover, from the J-V curve, the solar-to-hydrogen conversion efficiency can be calculated as a function of applied potential with an assumption that 100% of the photocurrent is used to actually split water. However, many samples require an external bias (or overpotential) in order to drive water electrolysis due to unsuitable band edge positions or low overpotentials/slow catalysis of some samples. Therefore, applied bias photon-to-current efficiency (ABPE) can be employed for such samples and it is defined as [1, 8, 9].

$$ABCE = J_{mp}(V_{redox} - V_{app})/P_{in}$$

where J_{mp}, V_{redox}, V_{app}, P_{in} are the measured photocurrent density (mA/cm^2), the theoretical water-electrolysis voltage (1.23 V), the applied voltage (V), and the intensity of the incident light (100 mW/cm^2), respectively. Note that in the case of ABPE, the faradaic efficiency which corresponds to the ratio of the current contributing to water splitting into hydrogen and oxygen to the observed current is not considered explicitly.

The IPCE measurement is another important technique to investigate the spectral response of a photoelectrode, in which the photocurrent is recorded as a function of the wavelength at a constant applied potential. The intensity of the incident light as a

function of wavelength usually should be recorded using a calibrated photodiode and due to very much lower value of the intensity, the measured currents are relatively small and the dark current cannot be negligible. Therefore, the photocurrent for IPCE measurement always has to be reported as the difference between the current values under illumination and dark. IPCE value is defined by the number of electrons generated by light in the external circuit divided by the number of incident photons [2, 10]:

$$IPCE(\%)=1240\ J_{photo(\lambda)} / \lambda\ P_{in}$$

where λ, $J_{photo(\lambda),}$ P_{in} are the wavelength of the incident light (nm), the photocurrent density ($\mu A/cm^2$), and the intensity of the incident light ($\mu W/cm^2$), respectively. The number 1240 is the unit conversion factor (eVnm) from the product of the Plank constant and the speed of light. From the IPCE spectrum, an estimate of the total photocurrent under AM1.5 illumination can be obtained by integration over all the IPCE values for each wavelength through an important underlying assumption that there is a linear relationship between the monochromatic photocurrent and the light intensity. However, the presence of surface traps or slow surface reaction kinetics may cause large deviations between the predicted solar photocurrent and the measured photocurrent under AM1.5 conditions.

1.1.2 Working mechanism of PEC water splitting cells

An overview of the working principle is described on the basis of thermodynamics and kinetics of PEC water splitting process in this section. There are several options for the arrangement of photoelectrodes in PEC water splitting cells. However, this section will be limited to a basic cell configuration, two electrodes system,

consisting of a photoanode (n-type semiconductor) and a Pt counter electrode (Figure 1.3).

There are three important steps necessary for overall PEC water splitting process:

(1) First step: absorption of light near the surface of the n-type semiconductor creates electron–hole pairs and they are spatially separated from each other due to the presence of an electric field at the semiconductor and electrolyte junction which will be discussed in detail later.

(2) Second step: holes as minority carriers drift to the surface of the semiconductor then the semiconductor/electrolyte interface where they oxidize water to produce oxygen gas.

(3) Final step: electrons as majority carrier are conducted via an external wire toward a Pt counter electrode where they combine with H^+ ions in the electrolyte solution to generate hydrogen gas. Transport of H^+ from the photoanode to the counter electrode through the electrolyte completes the electrochemical circuit.

Following is the overall reaction [9, 10]:

$$2h\nu + H_2O \rightarrow H_2\,(g) + \tfrac{1}{2}\,O_2\,(g)\ (1.23\ eV,\ \Delta G^\circ = -nF\Delta E = +237\ kJ/mol)$$

where ΔG° is the Gibbs free energy change for the overall water splitting reaction, n is the number of electrons transferred in above reaction, F is the Faraday constant, and ΔE are the electric potential of the reaction at standard conditions (298 K, 1 mol/L, 1 bar), respectively. This value of +237 kJ/mol, which corresponds to $\Delta E° = 1.23$ V per electron transferred according to the Nernst equation, shows that the water-splitting reaction is thermodynamically uphill. However, there are losses during the electron-transfer processes at semiconductor/electrolyte junctions due to the concentration and kinetic

overpotentials required to drive the hydrogen evolution reaction and oxygen evolution reaction. Therefore, in order to generate the *V*oc required to split water, a semiconductor should have a band gap energy (E_g) with a 1.6 to 2.4 eV.

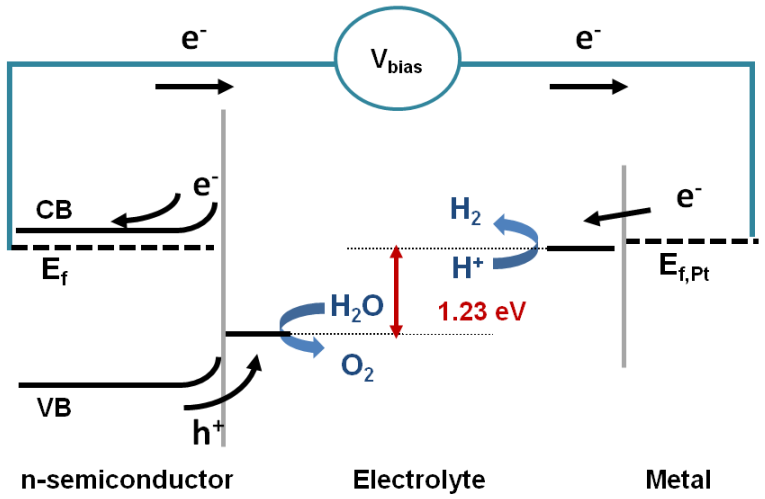

Figure 1.3 Energy diagrams of photocatalytic water splitting based on an n-type semiconductor photoanode and metal counter electrode (one-step excitation).

To design an efficient PEC water splitting cell, it is critical to understand the properties of semiconductor and semiconductor/electrolyte interface such as the band positions and the amount of band bending, which can be easily understood by energy diagram for a PEC cell. Figure 1.4 depicts the energy diagram of an n-type semiconductor/liquid contact[8]. When the semiconductor is immersed in an electrolyte solution at open circuit, the Fermi level of semiconductor is higher than the redox potential of the electrolyte and this difference between them is called the barrier height (Figure 1.4a). Consequently, electron transfer takes place between the semiconductor and the electrolyte solution so that the Fermi level of semiconductor is equilibrated with the

redox potential of electrolyte solution. The electron transfer leads to the positive charge associated with the space charge layer (also referred to as a depletion layer) causing an upward bending of the band edges as the majority charge carrier is removed from this region. The space charge layer results in an interfacial electric field whose electrostatic potential balances the initial difference in electrochemical potentials between the electrolyte solution and semiconductor (Figure 1.4b). The electric field plays an important role in charge separation of photogenerated charge carriers. Under illumination, non- equilibrium electron and hole pairs are created particularly in the space charge layer, the Fermi level increases with an internal photovoltage and the electron quasi-Fermi level and the hole quasi-Fermi level are formed (Figure 1.4c). The internal photovoltage which is referred to the open circuit voltage, V_{oc}, is given by the difference between the quasi-Fermi levels of electron and hole, that is, by the free energy difference between the majority carriers and the photoexcited minority carriers. The V_{oc} determines the photoelectrochemical reactions that can be driven by that system. It is well known that the redox potentials for water oxidation and reduction are pH dependent:

$$E^{\circ}(O_2/H_2O) = 1.23\ V - 0.059\ V \times pH\ (vs\ NHE)$$

Despite pH dependence of the redox couple, shifting the band edge of the semiconductor by a pH-dependent surface dipole (i.e., ~60 mV per pH unit) makes the relative interfacial energetics of a semiconductor/electrolyte junction pH independent.

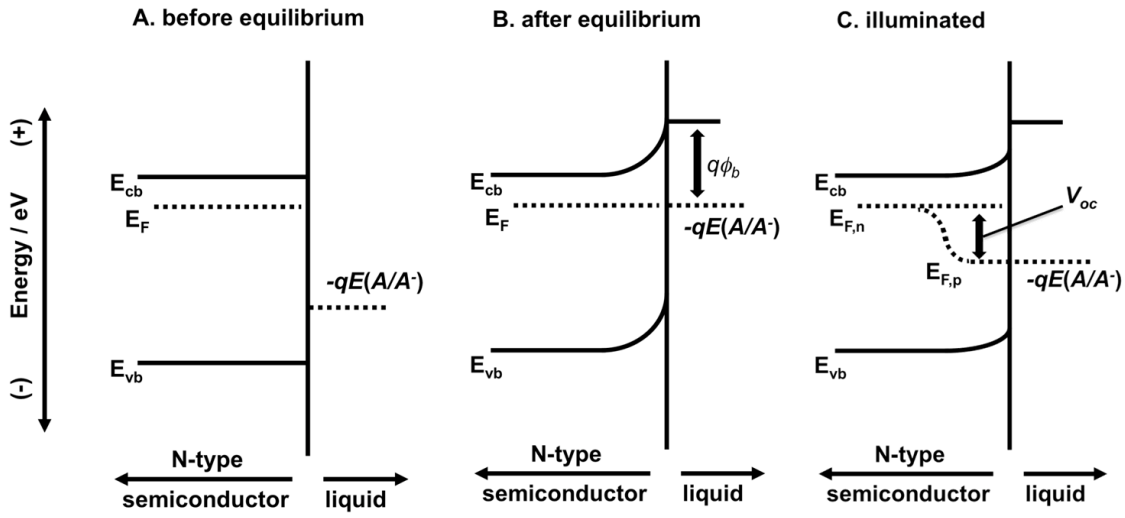

Figure 1.4 Energy diagram of an n-type semiconductor/liquid contact in three cases: (a) before equilibration between the two phases; (b) after equilibration, but in the dark; and (c) in quasi-static equilibrium under steady state illumination[8] (copy right American Chemical Society).

Even though a semiconductor meets the thermodynamic requirements with the appropriate band-edge positions to straddle the water oxidation and reduction levels, water splitting is not possible without any external bias unless recombination is sufficiently suppressed so that the V_{oc} exceeds 1.23 V. Therefore, to achieve efficient PEC performances of the semiconductor, we need also to understand the kinetics of the charge transfer from the semiconductor surface to the electrolyte solution, which is influenced by both on the number of charge carriers at the semiconductor surface and on the energetics of the semiconductor band edges. The useful current is produced by two main processes such as electron collection by the back contact and hole collection by the redox couple, which contribute positively to device efficiency. However, there are several recombination processes of photogenerated carriers at open circuit to generate unfavorable current; radiative or non-radiative recombination in the bulk of the

semiconductor, recombination in depletion-region of the semiconductor, surface recombination by surface defects or tunneling, recombination of majority carriers passing through the interfacial barrier. Under the dark, only few minority carrier holes are present, which allows their contribution to the rate to be neglected while the majority-carrier electron-transfer process is a source of detrimental recombination current. The applied potential to the semiconductor affects a change in the charge-transfer rate by changing the electron concentration at the semiconductor surface. Therefore, it should be minimized by introduction of a large electrostatic barrier at the semiconductor surface. Meanwhile, under illuminations, the charge transfer rate of minority carrier holes is very important to produce valuable current, which is related to the surface hole concentration described by the energy difference between the hole quasi-Fermi level and the valence band edge. The hole transfer is independent of the light intensity or the applied potential provided that the semiconductor remains in depletion. However, it is influenced by the energy difference between the valence band edge and the redox potential of electrolyte which is called a “built-in” overpotential for driving a given water oxidation/reduction reactions.

1.1.3 Photoelectrode materials requirements

The most critical aspect for the design of a PEC water splitting cell is to choose appropriate photoanode and/or photocathode materials. There are a number of the materials requirements for ideal PEC water splitting cell although some of them appear to be contradictory. This section will explain the semiconductor requirements for high

performance cells and will present numerous research efforts/strategies to meet those materials demands.

The band gap of semiconductor determines a wavelength region in which the material absorbs light; the smaller band gap a material has, the more light it absorbs. However, not only to drive the hydrogen evolution reaction and oxygen evolution reaction using electrons/holes generated under illumination but also to maintain the stability of the PEC cell, the conduction and valence band edge energies of the semiconductor should straddle the electrochemical potentials of electrolyte. Also, to split water without any external bias, materials need a band gap (1.6 ~ 2.4 eV) large enough to split water considering the thermodynamic losses [8]. Moreover, the charge transfer from the surface of the semiconductor to the solution must be selective for water splitting rather than corrosion then the materials should exhibit long-term stability in aqueous electrolytes. Furthermore, the semiconductors need efficient charge separation/transfer/transport to obtain high PEC performances while the fabrication cost should be low for practical use. To date, no cost-effective material satisfies all of the technical requirements listed above. Hence, various attempts have been made in order to develop materials with bulk and interfacial characteristics to meet these criteria.

Narrow band gap materials such as Si, CuO, Cu_2O, and CdS show superior light absorption properties but they are not appropriate to drive oxidation or reduction of water because they have unfavorable band edge positions or very poor photochemical stabilities which leads to a huge overpotential for water splitting or decomposing/oxidizing the material itself in the water-based electrolyte [11-16]. To solve these issues, such materials have been combined with other materials which can produce internal photovoltage for

zero bias or low overpotential or improve photochemical stability. Si was functionalized with ultrathin and highly transparent NiO_x layer prepared by sol-gel process and the Si/NiO_x presented a negative-shifted onset potential and higher PEC performances in comparison with those of ITO or TiO_2 coated Si photoanode because the NiO_x film served as both a protection layer and an oxygen evolution catalyst and further provided internal photovoltage by the formation of pn junction at the interface with Si (Figure 1.5) [12]. Similarly, Cu_2O was modified by 10nm thick NiO_x layer and in contrast with the fast photodegradation of the unmodified electrode, Cu_2O /NiO_x exhibited the enhanced photochemical stability and catalysis (Figure 1.6) [17]. Also, TiO_2 nanoparticles were used to improve the photo-efficiency and photostability of CdS and the composites revealed higher photocatalytic activity than only CdS photoelectrode because of an efficient charge separation by fast diffusion of photoelectrons generated from CdS nanowires toward surrounding TiO_2 nanoparticles (Figure 1.7) [14].

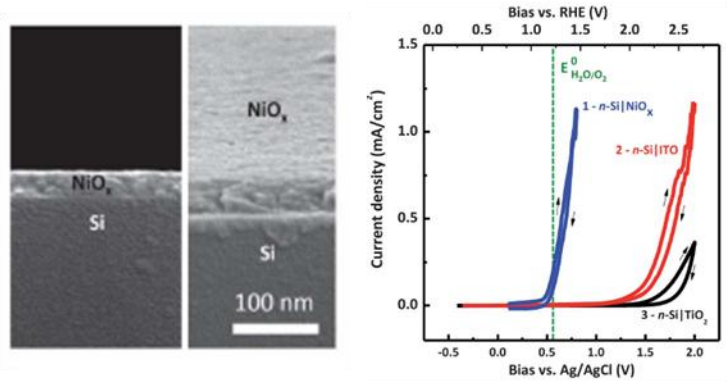

Figure 1.5 NiOx-functionalized Si photoanode[12] (copy right The Royal Society of Chemistry).

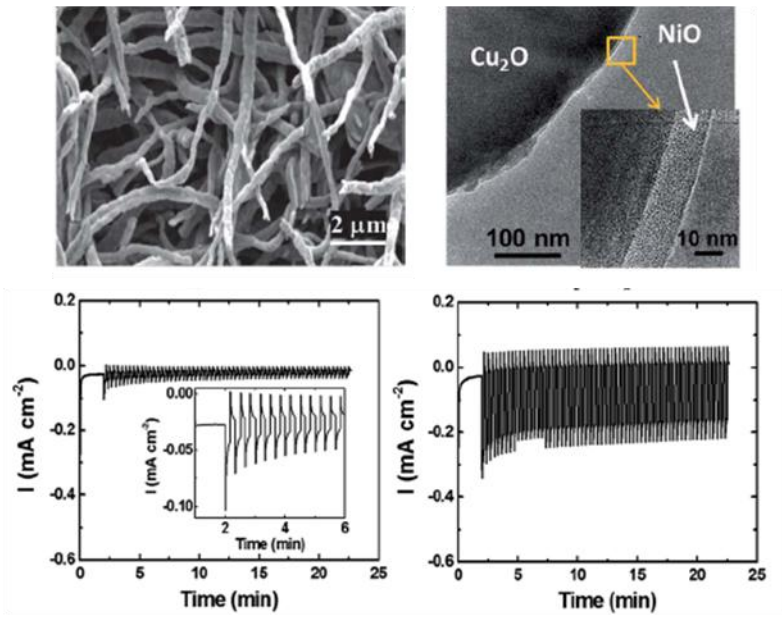

Figure 1.6 NiOx-modified Cu_2O photochathode[17] (copy right The Royal Society of Chemistry).

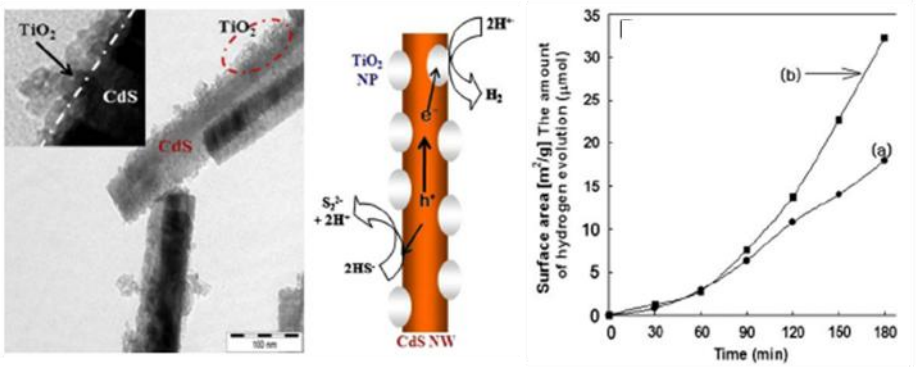

Figure 1.7 TiO_2-coated CdS photoanode[14] (copy right Elsevier).

Besides, structure engineering such as fabrications of textured, nano or branched structures can enhance PEC performances by not only the reduced reflectance which further improves light absorption but also the increased high surface-to-volume ratios (high surface area) or junction area which facilitates carrier separation and collection [18-20]. Although it has a narrow band gap and favorable band edge position, InP requires surface

texturing due to its low surface-recombination velocity [18]. Compared to the planar controls, the InP nanopillar arrays exhibited drastically improved solar driven hydrogen generation because surface nanotexturing resulted in higher current densities, more favorable onset potentials Furthermore, and further fast desorption of H_2 bubbles from the InP nanopillar surface through the lowered surface energy (Figure 1.8). Another example to indicate the effect of large junction areas is a paper about CdTe/TiO_2 electrodes constructed using highly ordered TiO_2 nanotube arrays [19]. The p-type CdTe nanoparticles with band gap of 1.5 eV were deposited on n-type TiO_2 nanotube arrays with band gap of 3.2 eV by two different methods; one is a typical electrochemical deposition method to deposit a thick CdTe nanoparticles layer on top of the TiO_2 nanotube pores and the other is their newly developed dipping and deposition technique to effectively deposit CdTe nanoparticles within the TiO_2 nanotubes enabling formation of a more intimate and conformal CdTe/TiO_2 junction (Figure 1.9). The second method significantly enhanced CdTe/TiO_2 junction areas which can facilitate the separation of electrons and holes at the junction, thus reducing electron-hole recombination in the CdTe. Therefore CdTe/TiO_2 with more intimate and conformal junctions showed the improved the photocurrent generation and photostability of the CdTe layer because of a longer path length for light in the CdTe layer as well as increased CdTe/TiO_2 and CdTe/electrolyte junction areas (Figure 1.9). In the same way, the branched TiO_2 nanorods exhibited the improved PEC water splitting efficiency compared to nanoparticles and nanorods because the several-fold increased surface area, which was created by branched structures, enhanced light absorption and improved charge separation and transport and also simultaneously offered a large contact area with the

electrolyte which facilitates the hole transfer at the TiO_2/electrolyte interface (Figure 1.10) [20].

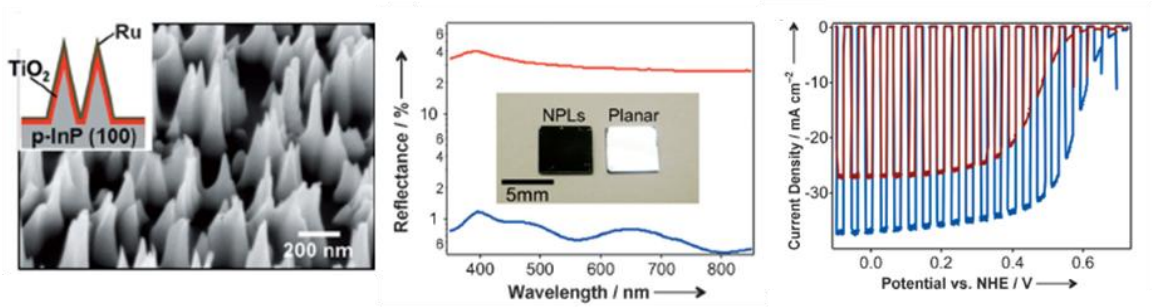

Figure 1.8 p-Type InP Nanopillar Photocathodes[18] (copy right Wiley)

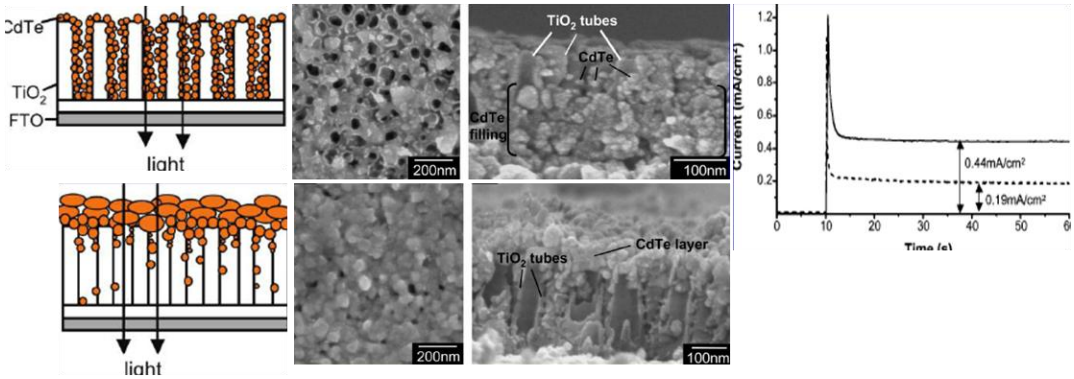

Figure 1.9 CdTe/TiO_2 electrodes with highly ordered TiO_2 nanotube arrays[19] (copy right American Chemical Society).

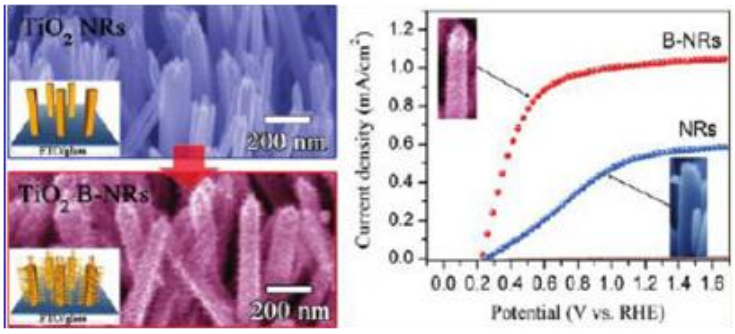

Figure 1.10 n-type branched TiO_2 nanorods electrodes[20] (copy right American Chemical Society).

The integration of electrocatalysts with light absorbing semiconductors is also a functional approach to develop high efficient PEC water splitting cells [21-23]. The introduction of RuO_2 cocatalysts onto the TaON surface resulted in observable O_2 evolution and remarked increase in photocurrent while only TaON electrode showed little photocatalytic activity, indicating that water oxidation on the loaded RuO_2 nanoparticles occurs more efficiently than on the TaON surface (Figure 1.11) [21]. Also, the PEC water oxidation performances of $BiVO_4$ electrode with different kinds of co-catalysts such as CoO_x, CoPi, IrO_x, MnO_x, RuO_x were investigated and among the co-catalyst tested, CoPi revealed the highest photocurrent density demonstrating the most efficient co-catalyst for O_2 evolution (Figure 1.12) [22]. Moreover, deposition of Ni, Ni–Mo, and Pt catalysts onto Si microwire arrays enhanced the apparent catalytic activities and both Ni and Ni–Mo alloy showed sufficient catalytic activity on the microwire arrays to make it a promising nonnoble alternative to Pt (Figure 1.13) [23]. Like these examples, an electrocatalyst deposited on the semiconductor surface influences not only the rate of electron transfer to and from the solution but also the equilibrium and non-equilibrium interface energetic, which is able to suppresses electron-hole recombination or to advance charge separation and photoelectrode performance [24]. Some electrocatalysts such as Pt or dense crystalline IrO_2, are metallic and thus the interface between semiconductor and electrocatalyst is expected to behave according to the well-developed theory of semiconductor/metal Schottky contacts [25]. The efficient electrocatalysts should catalyze desired reactions with relatively low overvoltages, to have high catalytic rates and have stability for long-term application. Noble metals and metal oxides like Pt, Pd, RuO_x, IrO_x, etc. meet most of the

requirements but they are very expensive, thus numerous efforts have been performed to develop cost-effective electrocatalysts.

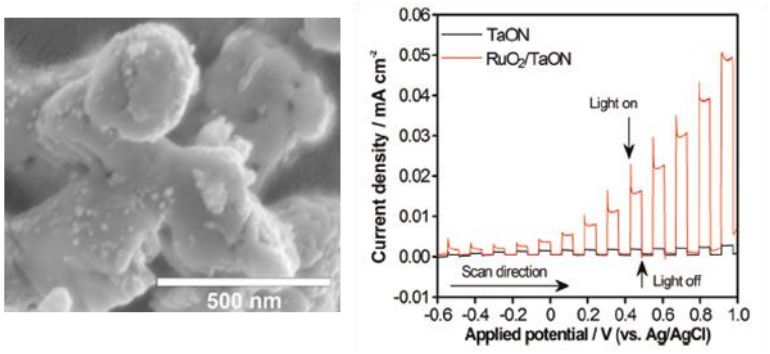

Figure 1.11 TaON photoelectrode with RuO_2 cocatalyst [21] (copy right American Chemical Society).

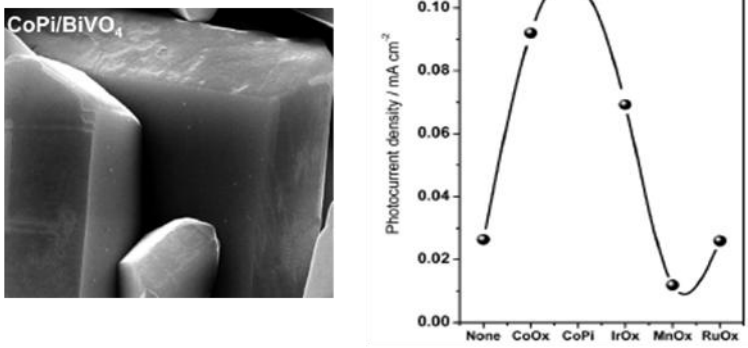

Figure 1.12 $BiVO_4$ photoelectrode with Co-Pi electrocatalyst[22] (copy right American Chemical Society).

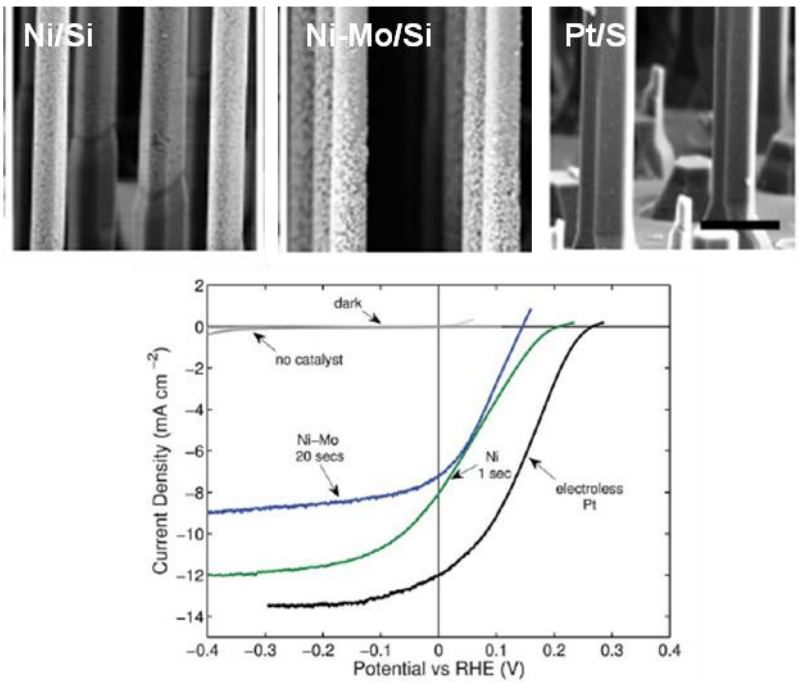

Figure 1.13 Si electrodes with Pt, Ni, and Ni–Mo electrocatalysts for hydrogen evolution [23] (copy right The Royal Society of Chemistry).

Above and beyond these strategies, there are the integration of a photovoltaic (PV) cell with catalysts or in series with the PEC photoelectrode materials to provide additional voltage (Figure 1.14a) [26-29], the addition of plasmonic metal nanoparticles on semiconductors to enhance optoelectronic properties of semiconductors by plasmon resonance energy transfer, hot electron production, and scattering and anti-reflection effects (Figure 1.14b) [30-32], metal/cation/anion doping in semiconductors to improve light absorption properties or electric conductivities (Figure 1.14c) [33-35], and so on.

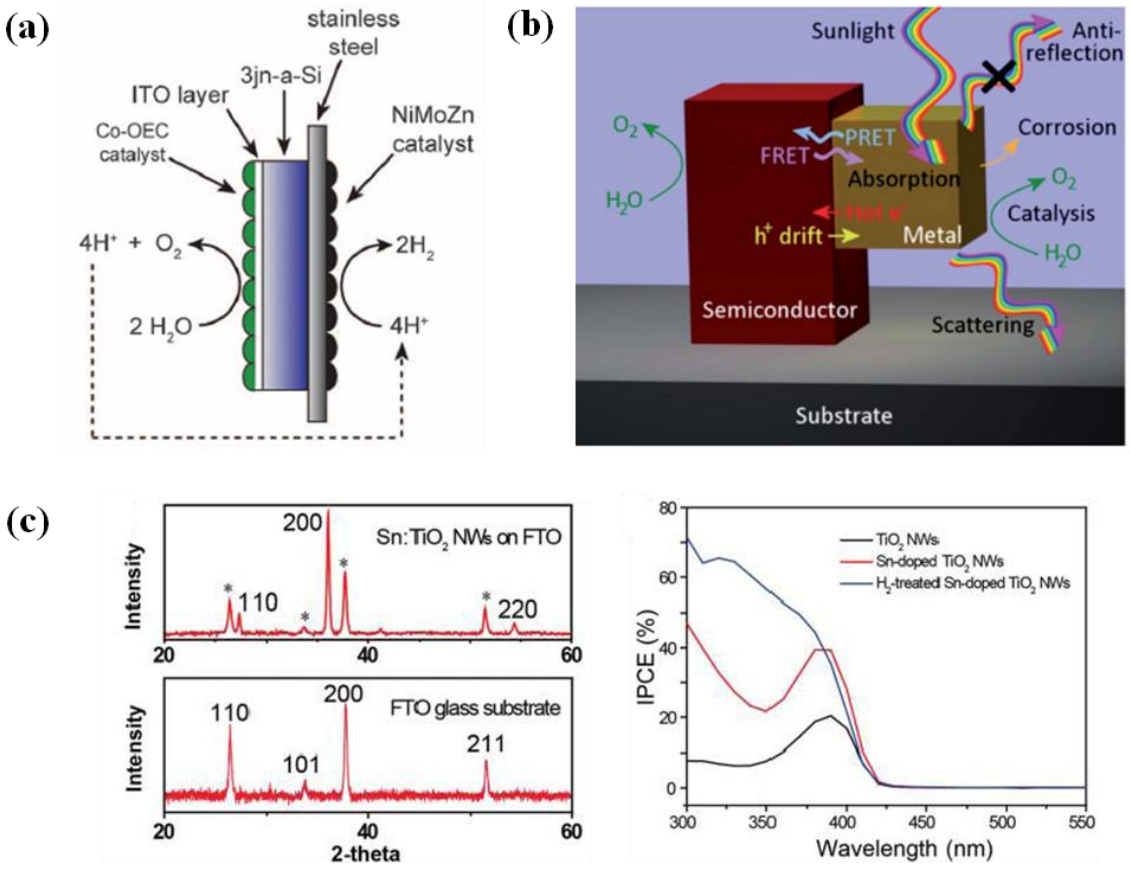

Figure 1.14 Other strategies: (a) the integration of a PV cell with catalysts[27] (copy right AAA Science), (b) the addition of plasmonic nanoparticles on photoelectrode (copy right The Royal Society of Chemistry)[30], (c) metal/cation/anion doping in semiconductors[33] (copy right American Chemical Society).

1.2 Thesis objectives

Solar energy conversion into storable and transportable chemical energy via PEC water splitting cell to generate hydrogen is an attractive scientific and technological goal to address the increasing worldwide demand for energy and to reduce the impact of energy production on climate change. As mentioned above, the key criteria for suitable water-splitting photoelectrode materials include good light absorption (visible range), proper band edge positions, superior chemical stability, low overpotentials for reduction/oxidation of water, efficient charge separation/transfer/transport in semiconductor, and low cost.

In order to fabricate economically competitive and highly efficient PEC water splitting cells, it is essential to choose appropriate photoelectrode materials by considering band gap energy, photo or chemical stability and electrical properties. Also, it is necessary to engineer and optimize the electrode structures by taking into account materials/electrolyte junction effects, dimensions, and optical properties such as scattering or reflectance. Finally, it is important to develop well-designed and cost effective fabrication methods.

1.3 Overview of the dissertation

Chapter 1 provides a brief introduction to principles of photoelectrochemical (PEC) water splitting cells and our research objectives.

Chapter 2 describes the preparation and characterizations of as-grown and post growth treated TiO_2 nanowires and explains the effects of different post growth treatments on PEC water splitting performances.

Chapter 3 illustrates the fabrication of TiO_2/Si core-shell nanowires and 3D branched TiO_2/Si nanowires and compares their PEC water splitting performances.

Chapter 4 describes the design of metal-silicon (MS) or metal-insulator-silicon (MIS) structures as PEC water splitting photoanodes and investigates the effects of metal thickness and differently prepared insulator on PEC water splitting performances.

Chapter 5 depicts the patterning of metal layer in metal-silicon (MS) or metal-insulator-silicon (MIS) structures as PEC water splitting photocathodes and investigates the effects of differently prepared insulator, bimetal thickness and ratio on PEC water splitting performances.

Chapter 6 summarized the dissertation and describes potential future directions.

1.4 References

1. Hisatomi, T., Kubota, J. & Domen, K. Recent advances in semiconductors for photocatalytic and photoelectrochemical water splitting. *Chemical Society Reviews* (2014).

2. Bak, T., Nowotny, J., Rekas, M. & Sorrell, C.C. Photo-electrochemical hydrogen generation from water using solar energy. Materials-related aspects. *International Journal of Hydrogen Energy* **27**, 991-1022 (2002).

3. Fujishima, A. & Honda, K. Electrochemical Photolysis of Water at a Semiconductor Electrode. *Nature* **238**, 37-38 (1972).

4. Wrighton, M.S. Photoelectrochemical conversion of optical energy to electricity and fuels. *Accounts of Chemical Research* **12**, 303-310 (1979).

5. Heller, A. & Miller, B. Some recent progress in semiconductor-liquid junction solar cells. *Electrochimica Acta* **25**, 29-41 (1980).

6. Weber, M.F. & Dignam, M.J. Efficiency of Splitting Water with Semiconducting Photoelectrodes. *Journal of The Electrochemical Society* **131**, 1258-1265 (1984).

7. Bard, A.J. & Fox, M.A. Artificial Photosynthesis: Solar Splitting of Water to Hydrogen and Oxygen. *Accounts of Chemical Research* **28**, 141-145 (1995).

8. Walter, M.G. Warren, E.L., McKone, J.R., Boettcher, S.W., Mi, Q. Santori, E.A., and Lewis, N.S., Solar Water Splitting Cells. *Chemical Reviews* **110**, 6446-6473 (2010).

9. Grätzel, M., Krol, R. v. d., & SpringerLink (Online) Photoelectrochemical hydrogen production. (New York, Springer; 2012).

10. Chouhan, N., Chen, C., Chang, W.-S., Cheng, K.-W. & Liu, R.-S. in Electrochemical Technologies for Energy Storage and Conversion 541-599 (Wiley-VCH Verlag GmbH & Co. KGaA, 2011).

11. Kargar, A., Jing, Y., Kim, S.J., Riley, C.T., Pan, X., and Wang, D., ZnO/CuO Heterojunction Branched Nanowires for Photoelectrochemical Hydrogen Generation. *ACS Nano* (2013).

12. Sun, K., Park, N., Sun, Z., Zhou, J., Wang, J., Pang, X., Shen, S., Noh, S. Y., Jing, Y., Jin, S., Yu, P.K.L., and Wang, D., Nickel oxide functionalized silicon for efficient photo-oxidation of water. *Energy & Environmental Science* **5**, 7872-7877 (2012).

13. Siripala, W., Ivanovskaya, A., Jaramillo, T.F., Baeck, S.-H. & McFarland, E.W. A Cu2O/TiO2 heterojunction thin film cathode for photoelectrocatalysis. *Solar Energy Materials and Solar Cells* **77**, 229-237 (2003).

14. Jang, J.S., Kim, H.G., Joshi, U.A., Jang, J.W. & Lee, J.S. Fabrication of CdS nanowires decorated with TiO2 nanoparticles for photocatalytic hydrogen production under visible light irradiation. *International Journal of Hydrogen Energy* **33**, 5975-5980 (2008).

15. Sun, K., Jing, Y., Li, C., Zhang, X., Aguinaldo, R., Kargar, a., Madsen, K., Banu, K., Zhou, Y., Bando, Y., Liua, Z., and Wang, D., 3D branched nanowire heterojunction photoelectrodes for high-efficiency solar water splitting and H2 generation. *Nanoscale* **4**, 1515-1521 (2012).

16. Cao, C., Hu, C., Shen, W., Wang, S., Tian, Y., and Wang, X., Synthesis and characterization of TiO2/CdS core-shell nanorod arrays and their photoelectrochemical property. *J Alloys Compd* **523**, 7-7 (2012).

17. Lin, C.-Y., Lai, Y.-H., Mersch, D. & Reisner, E. Cu2O|NiOx nanocomposite as an inexpensive photocathode in photoelectrochemical water splitting. *Chemical Science* **3**, 3482-3487 (2012).

18. Lee, M.H., Takei, K., Zhang, J., Kapadia, R., Zheng, M., Chen, Y., Nah, J., Matthews, T.S., Chueh, Y., Ager, J.W., and Javey, A., p-Type InP Nanopillar Photocathodes for Efficient Solar-Driven Hydrogen Production. *Angewandte Chemie International Edition*, n/a-n/a (2012).

19. Seabold, J.A., Shankar, K., Wilke, R.H.T., Paulose, M., Varghese, O.K., Grimes, C.A., and Choi, K., Photoelectrochemical Properties of Heterojunction CdTe/TiO2 Electrodes Constructed Using Highly Ordered TiO2 Nanotube Arrays. *Chemistry of Materials* **20**, 5266-5273 (2008).

20. Cho, I.S., Chen, Z., Forman, A.J., Kim, D.R., Rao, P.M., Jaramillo, T.F., and Zheng, X., Branched TiO2 Nanorods for Photoelectrochemical Hydrogen Production. *Nano Letters* **11**, 4978-4984 (2011).

21. Maeda, K., Abe, R. & Domen, K. Role and Function of Ruthenium Species as Promoters with TaON-Based Photocatalysts for Oxygen Evolution in Two-Step Water Splitting under Visible Light. *The Journal of Physical Chemistry C* **115**, 3057-3064 (2011).

22. Wang, D., Li, R., Zhu, J., Shi, J., Han, J., Zong, X., and Li, C., Photocatalytic Water Oxidation on BiVO4 with the Electrocatalyst as an Oxidation Cocatalyst: Essential Relations between Electrocatalyst and Photocatalyst. *The Journal of Physical Chemistry C* **116**, 5082-5089 (2012).

23. McKone, J.R., Warren, E.L., Bierman, M.J., Boettcher, S.W., Brunschwig, B.S., Lewis, N.S., and Gray, H.B., Evaluation of Pt, Ni, and Ni-Mo electrocatalysts for hydrogen evolution on crystalline Si electrodes. *Energy & Environmental Science* **4**, 3573-3583 (2011).

24. Tran, P.D., Wong, L.H., Barber, J. & Loo, J.S.C. Recent advances in hybrid photocatalysts for solar fuel production. *Energy & Environmental Science* **5**, 5902-5918 (2012).

25. Lin, F. & Boettcher, S.W. Adaptive semiconductor/electrocatalyst junctions in water-splitting photoanodes. *Nat Mater* **13**, 81-86 (2014).

26. Sun, K., Shen, S., Cheung, J.S., Pang, X., Park, N., Zhou, J., Hu, Y., Sun, Z., Noh, S.Y., Riley, C.T., Yu, P.K.L., Jin, S., and Wang, D., Si photoanode protected by a metal modified ITO layer with ultrathin NiOx for solar water oxidation. *Physical Chemistry Chemical Physics* **16**, 4612-4625 (2014).

27. Reece, S.Y., Hamel, J.A., Sung, K., Jarvi, T.D., Esswein, A.J., Pijpers, J.J.H., and Nocera, D.G., Wireless Solar Water Splitting Using Silicon-Based Semiconductors and Earth-Abundant Catalysts. *Science* **334**, 645-648 (2011).

28. Miller, E.L., Marsen, B., Paluselli, D. & Rocheleau, R. Optimization of Hybrid Photoelectrodes for Solar Water-Splitting. *Electrochemical and Solid-State Letters* **8**, A247-A249 (2005).

29. Brillet, J., Cornuz, M., Le Formal, F., Yum, J. Graetzel, M., and Sivula, K., Examining architectures of photoanode-photovoltaic tandem cells for solar water splitting. *Journal of Materials Research* **25**, 17-24 (2010).

30. Warren, S.C. & Thimsen, E. Plasmonic solar water splitting. *Energy & Environmental Science* **5**, 5133-5146 (2012).

31. Thimsen, E., Le Formal, F., Grätzel, M. & Warren, S.C. Influence of Plasmonic Au Nanoparticles on the Photoactivity of Fe2O3 Electrodes for Water Splitting. *Nano Letters* **11**, 35-43 (2010).

32. Ingram, D.B. & Linic, S. Water Splitting on Composite Plasmonic-Metal/Semiconductor Photoelectrodes: Evidence for Selective Plasmon-Induced Formation of Charge Carriers near the Semiconductor Surface. *Journal of the American Chemical Society* **133**, 5202-5205 (2011).

33. Xu, M., Da, P., Wu, H., Zhao, D. & Zheng, G. Controlled Sn-Doping in TiO2 Nanowire Photoanodes with Enhanced Photoelectrochemical Conversion. *Nano Letters* **12**, 1503-1508 (2012).

34. Bajnóczi, É.G., Balázs, N., Mogyorósi, K., Srankó, D.F., Pap, Z., Ambrus, Z., Canton, S.E., Norén, K., Kuzmann, E., Vértes, A., Homonnay, Z., Oszkó, A., Pálinkó, I., and Sipos, P., The influence of the local structure of Fe(III) on the photocatalytic activity of doped TiO2 photocatalysts—An EXAFS, XPS and Mössbauer spectroscopic study. *Applied Catalysis B: Environmental* **103**, 232-239 (2011).

35. Yang, X., Wolcott, A., Wang, G., Sobo, A., Fitzmorris, R.C., Qian, F., Zhang, J.Z., and Li, Y., Nitrogen-Doped ZnO Nanowire Arrays for Photoelectrochemical Water Splitting. *Nano Letters* **9**, 2331-2336 (2009).

CHAPTER 2: Photoelectrochemical Water Splitting Performance of Post growth treated TiO_2 Nanowires

2.1 Introduction

Photoelectrochemical (PEC) water splitting via various semiconducting materials and structures has been extensively studied because it is one of the most attractive approaches to efficiently produce hydrogen fuel as a transportable alternative energy[1-8]. In particular, titanium dioxide (TiO_2) has been comprehensively explored as a photoanode material due to its superior chemical stability as well as photochemical and photocatalytic properties[9-14]. Also, their one-dimensional (1D) nanostructures such as nanowires (NWs) or nanotubes (NTs) can be easily fabricated by relatively low cost process such as hydrothermal growth or anodization method[13, 15-17]. Such 1D nanostructures offer a unique combination of the large surface areas/reaction sites, increased optical path lengths, direct electronic carrier transport pathways, and short lateral diffusion length for efficient light harvesting, high quantum efficiency and enhanced PEC water splitting reactions[18, 19]. However, TiO_2 has a wide band gap, leading to a limited light absorption in the visible region of solar spectrum, low electron mobility and short minority carrier diffusion length[10, 12]. To overcome these disadvantages of TiO_2 and improve its PEC water splitting performance, various investigations have been performed on ion doping, dye/quantum dot sensitization, metal co-catalyst, heterojunction structures[20-24].

Recently, black TiO_2 nanomaterials have received attention for PEC water splitting because of the improved light utilization with maintained stability and band alignment. Black TiO_2 can be obtained by an uncomplicated method, for example annealing under hydrogen atmosphere[25-27], in vacuum, and doping with metal anion with and without other cations. It has been reported that black anatase TiO_2 nanocrystals, which were prepared by hydrogenation in a 20.0-bar pure H_2 atmosphere at about 200°C for 5 days, had a reduced band gap due to the introduced defects states in the partially filled d-band, which results in notable photocatalytic decomposition activity in the visible region and thus PEC water splitting efficiency. They explained that highly disordered surfaces and crystalline cores were produced during the hydrogenation process, then caused an increased density of states which effectively shifted the valence band edge leading to a lower band gap[25]. Meanwhile, the hydrogen treated rutile TiO_2 NWs, which were prepared by annealing at 350 °C for 30 min under a pure hydrogen atmosphere, also significantly enhanced PEC water splitting performance (quantum efficiency from <1% to 98% at wavelength 300~370nm; conversion efficiency increased from 0.24 to 1.63% after H_2 treatment). However, they explained mainly due to the increased donor density of TiO_2 NWs by creating a high density of oxygen vacancies without introducing noticeable change in its energy band gap[26]. Besides, they further investigated the underlying mechanisms on highly efficient PEC water splitting performances of those oxygen-deficient rutile TiO_2 NWs via transient absorption mechanistic study in collaboration with other group.[27]. Therefore, they verified that the improved electrical properties of oxygen-deficient TiO_2 NWs resulted in much efficient spatial separation of electron−hole pairs at moderate applied bias and almost completely suppressed the

recombination losses leading to an improved PEC water splitting performance[27]. Although both research groups used pure hydrogen gas to synthesis black TiO_2 nanomaterials, they utilized different H_2 pressure and temperature and then they obtained different hydrogenation effects like the valence band shift from highly disordered surfaces or Fermi level shift from oxygen vacancies. Therefore, it should be noted that hydrogenation process conditions are very important.

On the other hand, it is very important to passivate surface states in nanostructures for high charge collection efficiency[28, 29]. Atomic layer deposition (ALD) is a coating technique for passivating surface states and it allows highly conformal coating on nanostructures[30]. Very recently, a quantitative study was conducted on the dependence of PEC water splitting performance on the length of rutile TiO_2 NWs and they demonstrated that the photocatalytic activity of rutile TiO_2 NWs can be noticeably improved by ALD coating of additional rutile TiO_2 layer on the surface of TiO_2 NWs due to the passivation of surface states and an increase in surface area[31].

Both hydrogenation and ALD coating are straightforward post growth-treatment methods to improve PEC water splitting performance of TiO_2 NWs. However, they differently influence on the electrical properties of TiO_2 NWs. So far, it has not been investigated synergistic effects of hydrogenation and ALD coating as co-treatments of TiO_2 NWs. Here, we employ H_2/N_2 mixing gas (forming gas treatment) for hydrogenation or ALD coating or both to improve PEC performance of TiO_2 NWs via such simple post growth-treatments. To understand the effects of the post growth-treatments on surface morphologies/crystal structures, we have employed scanning electron microscope (SEM), high resolution transmission electron microscope (HRTEM),

X-ray photoelectron spectroscopy (XPS) and X-ray diffraction (XRD). Also, we have measured their dark- and photo-current density-voltage properties and incident photon to current conversion efficiencies to explore their PEC water splitting properties.

2.2 Experimental

2.2.1 Fabrication TiO_2 NWs and post growth treated TiO_2 NWs

TiO_2 NWs were prepared by a hydrothermal method[24]. For a growth solution, 1 ml of titanium n-butoxide (Alfa Aesar) was added drop-wise to a 1:1 mixture of DI water and concentrated hydrochloric acid (EMD chemicals) and stirred to obtain a clear transparent solution. A cleaned fluorine-doped tin oxide (FTO) glass was placed in the growth solution in a stainless steel autoclave with a Teflon liner (Parr instrument), and then sealed and maintained at 150 ˚C for 3hrs. After the hydrothermal reaction, the sample was removed from the solution, rinsed with ethanol, and dried with nitrogen gas, and followed by annealing at 450 ˚C for 2hrs in air. TiO_2 NWs grown on the FTO glass were obtained. For further modification of as-grown TiO_2 NWs, we employed different approaches such as forming gas (FG) treatment or atomic layer deposition (ALD). For FG TiO_2 NWs, as-grown TiO_2 NWs were treated in 10% H_2/90% N_2 mixed gas atmosphere at different temperatures (400, 450, 500, and 550 ˚C) for 2 hrs. For ALD TiO_2 NWs, we coated as-grown TiO_2 NWs with additional protecting TiO_2 layer by ALD method. Also, we used both processes with different sequences to obtain synergistic effects. For FG-ALD TiO_2 NWs, FG TiO_2 NWs were followed by ALD method and for ALD-FG TiO_2 NWs, ALD TiO_2 NWs were further treated by FG atmosphere.

2.2.2 Materials characterization and PEC performance measurements

To investigate the morphology of the TiO_2 NWs and differently post growth-treated TiO_2 NWs, a high-resolution SEM (FEI XL30-SFEG) was employed. The atomic scale structural analyses were performed using high-resolution transmission electron microscopy (HRTEM, JEOL JEM3100F) operated at 300 kV. For the TEM measurements, the TiO_2 NWs were scraped off from the FTO substrate onto a holey-carbon TEM grid. Also, the TiO_2 NWs with and without post growth-treatment were further characterized by both XPS (AXIS ULTRA equipped with Al Kα source line at 1486.6 eV) and XRD (Rigaku Multiflex X-ray diffractometer with Cu-Kα radiation (λ = 1.54 Å)).

PEC performance measurements were carried out in a 0.25 M Na_2SO_4 electrolyte (pH = 7.2) buffered with phosphate buffered saline (PBS). A three-electrode configuration was employed, where the unmodified and modified TiO_2 NW samples were used as photoanodes, a platinum coil as the counter electrode, and Ag/AgCl (with 1 M KCl) as the reference electrode[24, 32]. The photoanodes were illuminated by a solar simulator (Newport) equipped with a 150 W Xe lamp and an AM 1.5 filter (100 mW/cm^2) for light condition measurement. Both dark- and photo-current density-voltage (J–V) measurements were performed using a potentiostat (Digi-ivy Inc., DY2300) and all data were recorded using software DY2300. Photocurrent spectrum responses of the TiO_2 NWs and different post growth-treated TiO_2 NWs under a constant bias (1.23 V vs. RHE) were collected using a potentiostat (Digi-ivy Inc., DY2300) in conjugation with a monochromator (Horiba Jobin Yvon, iHR 550). Prior to the measurements, the intensity of the monochromated light was calibrated using a Si photodetector (Newport). To obtain

a steady-state photocurrent as well as dark current, a sufficiently low frequency of light chopping was used to allow the system to stabilize. The average steady-state current values were then used to calculate the incident photon to current conversion efficiencies (IPCEs)[24, 32].

2.3 Results and discussion

2.3.1 Morphologies and structures of TiO_2 NWs and post growth-treated TiO_2 NWs

Figure 2.1 indicates SEM images of typical TiO_2 NWs and differently post growth-treated TiO_2 NWs. Regardless of whether post growth-treatments were conducted or what kinds of them were employed, all NWs samples show high density and good vertical orientation with tetragonal top facets. Without any further modification, each TiO_2 NW with ~80nm of diameter had a bundle shape of secondary much thinner NWs (few nm) leading to a rough surface (Figure 2.1a'). These as-grown TiO_2 NWs samples on FTO glasses appeared semi-transparent after growth. Interestingly, additional TiO_2 ALD layer caused much smoother surface of TiO_2 NW by completely covering the secondary thinner NWs in each TiO_2 NW (Figure 2.1b'). Also, ALD TiO_2 NWs sample looked not semi-transparent but white color because additional TiO_2 layer made each TiO_2 NW thicker and then more reflection of TiO_2 NW surface occurred. However, FG treatment did not change the morphology of as-grown TiO_2 NWs but the color of FG treated samples was changed from grey to black as FG temperature increased from 400 ˚C to 550 ˚C. These color changes are similar to the results reported in previous literature even though they employed pure hydrogen gas with short time for hydrogenation. They explained the color changes are ascribed to the formation of impurity/defect states in the

band gap of TiO_2 NWs during hydrogen treatment[26]. This will be discussed more in XPS study. As shown in Figure 2.1f, the color of ALD - 450 ˚C FG TiO_2 NWs exhibit dark grey because additional TiO_2 ALD layer before FG treatment presumably acted as a blocking layer which prevents the secondary thinner NWs in each TiO_2 NW from reacting with forming gas in the next step, FG treatment. However, Figure 2.1g shows bright grey color of 450 ˚C FG - ALD TiO_2 NWs because oxygen vacancies formed by FG treatment might be reduced by additional TiO_2 ALD layer in the last step. This is not clear at this point, which is currently under investigation.

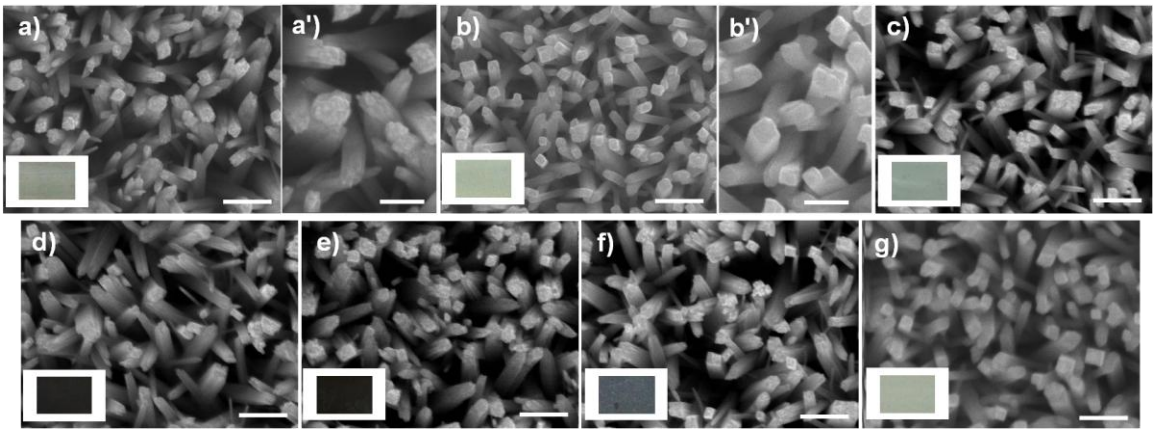

Figure 2.1 SEM images and optical images of typical TiO_2 NWs (a, a'), ALD TiO_2 NWs (b, b'), FG TiO_2 NWs treated at different temperatures of 400 ˚C (c), 450 ˚C (d), and 500 ˚C (e), ALD - 450 ˚C FG TiO_2 NWs (f), and 450 ˚C FG - ALD TiO_2 NWs (g). Scale bar is 500 nm except for 200 nm in (a') and (b').

Figure 2.2 shows TEM images, HRTEM images, and corresponding diffraction patterns of typical TiO_2 NWs and different post growth-treated TiO_2 NWs. The unmodified TiO_2 NWs have an edge with rough and jagged surface by secondary thinner NWs as we expected from SEM images while ALD-treated samples show a smooth surface. However, all TiO_2 NWs samples with and without post growth-treatments have

clearly visible lattice planes with spacing of 3.2±0.1 Å and 2.8±0.1 Å corresponding to the interplanar distance of the (110) and (001) planes of rutile TiO_2, respectively[24, 31]. Also, with zone axis [110], the diffraction patterns of them axis indicates that the TiO_2 NWs grew along the [002] direction.

XPS and XRD spectra of the unmodified and modified TiO_2 NWs were shown in Figure 2.3. Figure 2.3a–2.3c shows the high resolution XPS spectra of Ti 2p region (452–468 eV), O 1s region (527–535 eV), and valence band region (0–6 eV). For unmodified TiO_2 NWs, two sharp symmetric Ti 2p peaks appeared with binding energies centered at 458.5 eV and 464.2 eV which correspond to typical Ti $2p_{3/2}$ and Ti$2p_{1/2}$ peaks of Ti^{4+} in TiO_2, respectively[33, 34]. Also, a sharp peak in O 1s region (O 1s peak A) was observed at 529.8 eV attributed to the lattice oxygen ions O^{2-}, which are associated with Ti^{4+} in TiO_2. A broad peak (O 1s peak B) also exhibited at higher binding energy (531.8 eV) which can be ascribed to the hydroxyl groups or chemisorbed oxygen on the surface[26, 35] or which can be attributed to adventitious carbon contamination on the TiO_2 surface during sample preparation and subsequent XPS measurement[36, 37]. Note that TiO_2 has hydrophilic surface which can easily absorb water molecules in the air leading to the hydroxyl groups (O 1s peak B) on the surface. Regardless of difference in post growth-treatments, all of modified TiO_2 NWs indicate the peaks at identical positions in both Ti 2p. However, very small horizontal shift toward lower binding energy and peak narrowing of both Ti 2p peaks in 450 ˚C FG TiO_2 NWs were observed (Figure 2.3a). These can be explained by the reduced oxidation state of Ti ion from hydrogenation. In other words, hydrogenation can cause the increase oxygen vacancies and donor density in TiO_2 NWs because electronegativity of hydrogen is smaller than oxygen[38, 39]. However,

the peak shift was very small probably due to small amount of hydrogen gas used in our FG treatment compared to pure hydrogen gas or long time annealing in previous reports. Thus maybe the defects caused by the oxygen vacancy do not have significant density states that can be identified by the XPS. On the other hand, O 1s peak A was located at the same position in all samples irrespective of post growth-treatments. However, interestingly, O 1s peak B was differently shifted depending on post growth-treatment type and sequences (Figure 2.3b and 2.4). For example, compared to peaks of as-grown TiO_2 NWs, both ALD TiO_2 NWs and 450 ˚C FG-ALD TiO_2 NWs had the O 1s peak B at 531.0 eV which was not much separated from O 1s peak A. This implies that ALD layer can remove/reduce hydroxyl groups, chemisorbed oxygen, or organic contaminations on the TiO_2 surface. Meanwhile, both 450 ˚C FG TiO_2 NWs and ALD-450 ˚C FG TiO_2 NWs showed the O 1s peak B at 531.4 eV which was also closer to O 1s peak A but distinguishable from O 1s peak A, unlike that of ALD treated samples, suggesting TiO_2 surface hydration[35]. Moreover, both ALD and FG treatments did barely influence valence band maximum position (Figure 2.3c). Although it has been reported that the black color of hydrogenated TiO_2 nanoparticles resulted from surface disorder confirmed by a considerable shift of valence band position[25, 40], no shift of the valence band edge of hydrogen treated TiO_2 NWs has been also reported,[26] which is in good agreement with our results. From the XPS study, the dark color from hydrogenation is probably attributed to the formation of oxygen vacancies and surface hydroxyl groups on TiO_2. However, the energy states of surface hydroxyl groups below the valence band should not lead to visible light absorption due to their energetic stability[26]. Therefore, the oxygen vacancies below TiO_2 conduction band created by hydrogenation can cause the visible light

absorption of TiO_2 NWs and thereby the dark color of the samples[26, 27]. Furthermore, in Figure 2.3d, the unmodified TiO_2 NWs show an excellent agreement with the characteristic XRD patterns for the standard rutile structured TiO_2 (ICSD No. 064987, P42/mnm, a = b = 4.5845 Å and c=2.9537 Å). ALD TiO_2 NWs had obviously higher rutile TiO_2 peaks than those in as-grown and other post growth-treated TiO_2 NWs, confirming increased crystallinity. Also, there are new peaks (X, marked in Figure 2.3d) which can be peaks of anatase phase TiO_2 or FTO peaks. However, TEM study confirmed that all of samples are rutile TiO_2, which can confirm that the marked X peaks are from the FTO substrate. The other modified TiO_2 NWs also show almost same XRD peaks confirming that any post growth-treatments did not significantly change TiO_2 crystal structure. Therefore we concluded that FG treatment changed the color of TiO_2 NWs to dark (grey up to black) due to the formation of oxygen vacancies and surface hydroxyl groups on TiO_2 without any significantly changes of morphologies and crystal structures while ALD protected the surface of TiO_2 NWs by additional of TiO_2 layer, which can prevent/hinder the formation of oxygen vacancies and surface hydroxyl groups leading to whitening TiO_2 NWs with or without pre/post growth FG treatment.

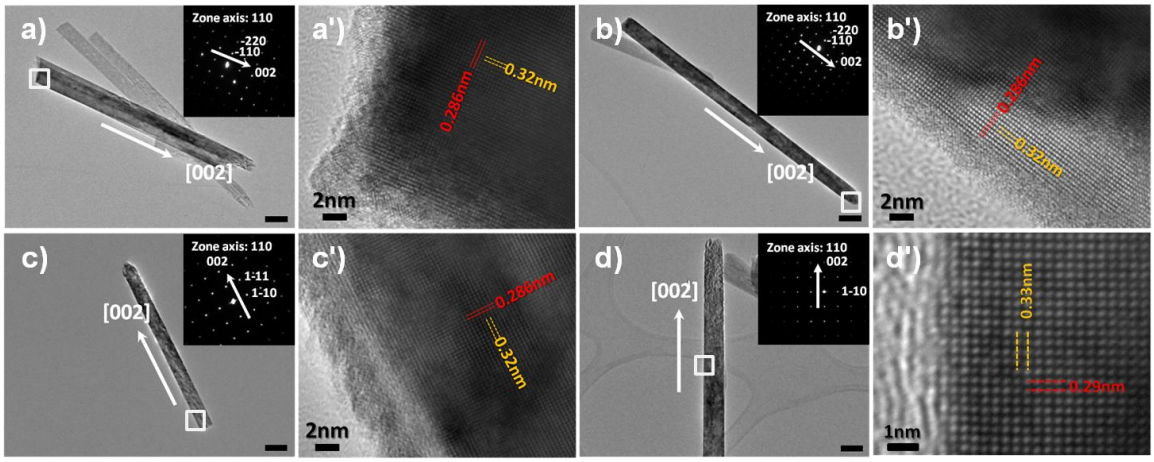

Figure 2.2 TEM images, diffraction patterns and HRTEM images of typical TiO_2 NWs (a, a'), ALD TiO_2 NWs (b, b'), ALD-450 ˚C FG TiO_2 NWs (c, c') and 450 ˚C FG-ALD TiO_2 NWs (d, d'). Scale bar is 100nm.

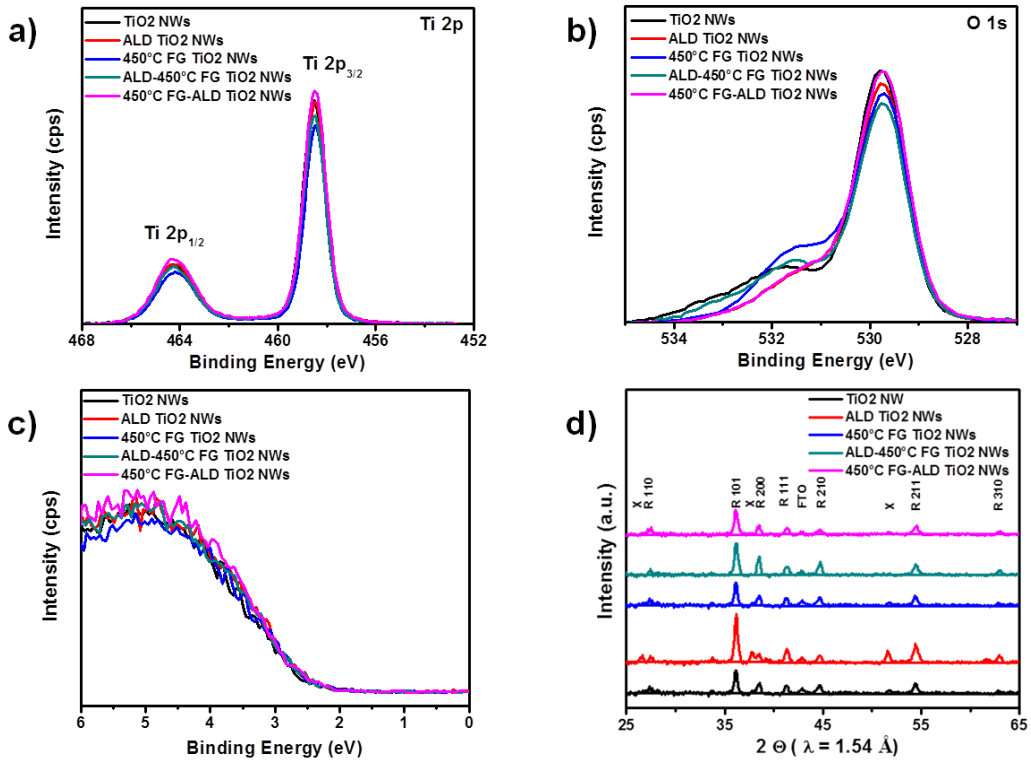

Figure 2.3 Ti 2p XPS peaks (a), O 1s XPS peaks (b), valence band XPS peaks (c) and XRD patterns (d) of typical TiO_2 NWs, ALD TiO_2 NWs, ALD-450 ˚C FG TiO_2 NWs and 450 ˚C FG-ALD TiO_2 NWs.

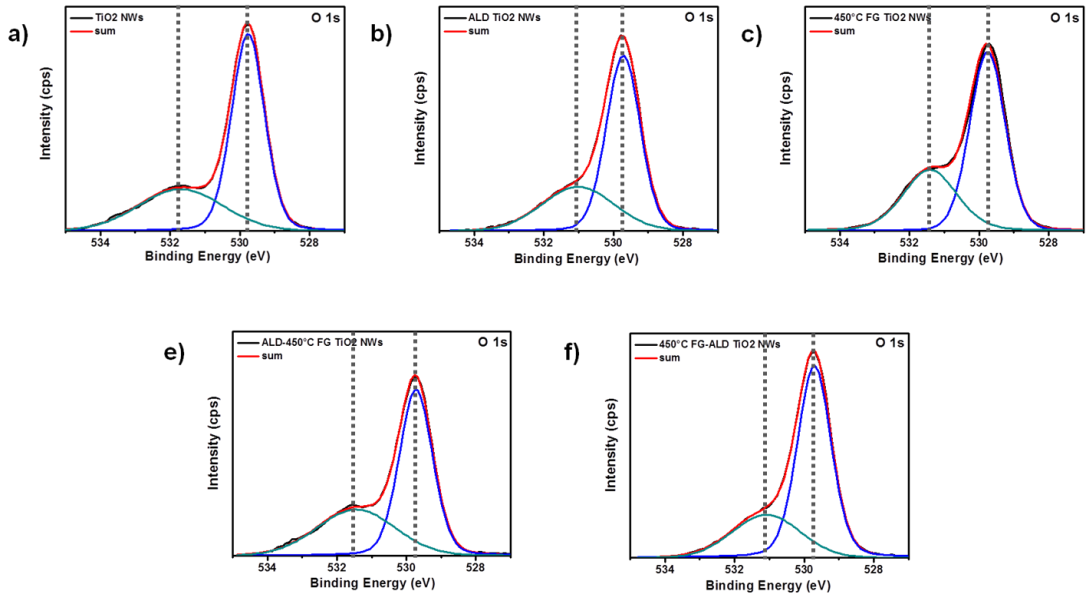

Figure 2.4 XPS O1s peaks of typical TiO_2 NWs, ALD TiO_2 NWs, ALD-450 ˚C FG TiO_2 NWs and 450 ˚C FG-ALD TiO_2 NWs.

2.3.2 PEC performances of different temperature FG treated TiO_2 NWs

We then investigated the effect of various FG treatment temperatures (from 400 ˚C to 550 ˚C) on PEC water splitting performance to optimize FG treatment conditions. The photocurrent-voltage (JV) and efficiency curves of the samples are shown in Figure 2.5. In this study, the PEC performance parameters are defined as flows. J_{sc} is a current density value of each sample at 1.23 V vs RHE (the Nernst potential for water oxidation, $E°_{H2O/O2}$) and V_{oc} is a voltage difference between $E°_{H2O/O2}$ and photo onset potential (V_{os}).

The TiO_2 NWs exhibited 0.17 % of efficiency with 0.37 mA/cm^2 of J_{sc} and 1.08 V of V_{oc}. When TiO_2 NWs were treated under FG atmosphere, J_{sc} significantly increased leading to higher efficiency although V_{oc} remained almost same and FF decreased in comparison with the performance parameters of as-grown TiO_2 NWs. V_{oc} is mainly determined by the over-potential of the oxidation reaction and the flat band potential[31],

which were not influenced by FG treatment. Especially, at a low potential window (V_{os} to 0.6 V vs RHE) in Figure 2.5a, 400 ˚C and 450 ˚C FG TiO_2 NWs show a dramatically increased current density, which means that the charge separation and transportation in those samples are more efficient, compared to the as-grown TiO_2 NWs and 500 ˚C FG TiO_2 NWs. We observed FG treatment over 450 ˚C notably increased the resistance of FTO substrate leading to remarkably reduced FF. Thus 550 ˚C FG TiO_2 NWs sample indicated very low photo-current density which was almost same as its dark current density (not shown here). That is, photo-induced charges from 550 ˚C FG TiO_2 NWs cannot be collected via FTO substrate which became an insulating substrate. Note that the maximum power of FG TiO_2 NWs was obtained at a higher bias than that of as-grown TiO_2 NWs and the bias increased according to FG treatment temperature up to 500 ˚C. This confirms that as the sheet resistance of FTO substrate increased with FG temperature, higher bias was required for efficient charge collection via FTO layer to Cu wire. The best FG TiO_2 NWs, which prepared at 450 ˚C under forming gas, show 2.6 times higher efficiency (0.45 %) mainly due to much higher J_{sc} (1.15 mA/cm^2). These results prove that FG treatment is a straightforward and effective method to improve the PEC performance of TiO_2 NWs. We will discuss FG treatment effects on the PEC performance more with the data of dark current density and IPCE below.

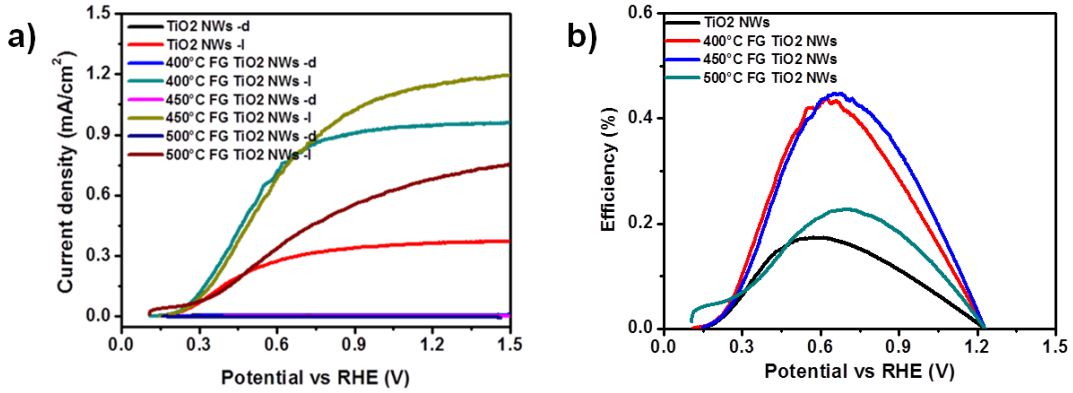

Figure 2.5 JV curves (a) and efficiency (b) of typical TiO_2 NWs and FG TiO_2 NWs treated at different temperatures.

2.3.3 PEC performances and Photocurrent spectrum responses of TiO_2 NWs and post growth-treated TiO_2 NWs

The PEC performances of different post growth-treated samples were compared to explore their each or synergetic effects. Figure 2.6 shows J-V curves, efficiency and IPCE data of as-grown TiO_2 NWs, ALD TiO_2 NWs, 450 ˚C FG TiO_2 NWs, ALD-450 ˚C FG TiO_2 NWs and 450 ˚C FG-ALD TiO_2 NWs. Although ALD treatment increased J_{sc} by about 1.6 times, ALD TiO_2 NWs exhibited similar efficiency (0.18%) due to very low FF. There are two possible reasons for low FF. One is due to the defect/impurities in TiO_2 NWs which cause the fast recombination losses between photo induced electrons and holes[41]. However, from XPS data (Figure 2.3), ALD treated samples did not show broadening both Ti 2p peaks, confirming there were no defects/impurities and XRD shows better crystallinity. Also, in general, the defects/impurities in materials cause higher dark current density[42]. However, in Figure 2.7, unlike TiO_2 NWs, ALD treated samples showed very low dark current which further decreased as the applied bias

increased confirming no defects in TiO_2 NWs of ALD treated samples. Note that the dark current value for all samples is few $\mu A/cm^2$ showing good quality of NWs. Another possible reason for low FF is the smaller surface area/roughness from the smoother surface of ALD TiO_2 NWs. We observed that TiO_2 NWs have rough surface and higher surface area, consisting of secondary ultrathin NWs in each TiO_2 bundle (Figure 2.1a'). However, ALD TiO_2 NWs have no secondary NWs exposed to electrolyte (Figure 2.1b') and they need high bias as a driving force for charge separation in bulk. Therefore, ALD TiO_2 NWs had higher Tafel slope (167 mV/decade) than TiO_2 NW (134 mV/decade) in Figure 2.8. Also, in comparison with TiO_2 NWs, smaller photocurrent density was obtained at lower bias and the maximum power also exhibited at higher bias. Nevertheless, as the bias increased, photocurrent density dramatically increased and in Figure 2.6c, IPCE value of ALD TiO_2 NWs was also much enhanced in the UV region, compared to that of TiO_2 NWs. It has been reported that despite efficient light absorption at the shorter wavelengths due to a larger absorption coefficient of TiO_2, the IPCE value of TiO_2 generally decreases at the shorter wavelengths like our IPCE data of as-grown TiO_2 NWs because a fraction of the photo-induced majority carriers in the depletion region can diffuse to the electrolyte interface against the electric field leading to the recombination with holes[31]. These electron diffusion losses are significant when the majority carrier's mobility is low and there is a high density of surface/interface states which creates a large recombination velocity. Note that the improvement of IPCE value in ALD TiO_2 NWs occurred particularly at the short wavelength as well as the dark current density was very low and further decreased as the applied bias increased. ALD TiO_2 NWs have no the exposed ultrathin secondary NWs of TiO_2 NWs which can be

charge trapping sites at their interfaces. This implies that ALD layer acted as a protecting layer to passivate defect sites of TiO_2 NWs surface leading to increased charge collection efficiency.

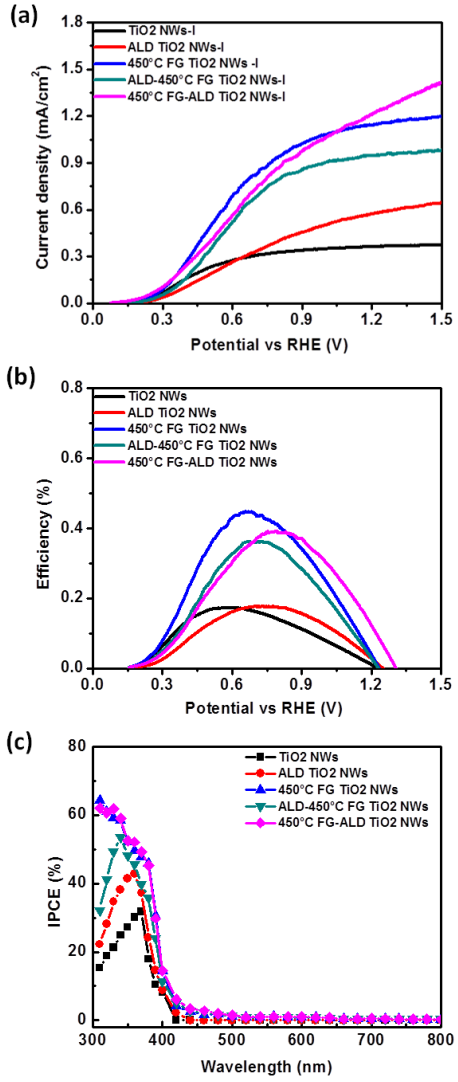

Figure 2.6 JV curves (a), efficiency (b) and IPCE data (c) of typical TiO_2 NWs, ALD TiO_2 NWs, 450 ˚C FG TiO_2 NWs, ALD-450 ˚C FG TiO_2 NWs, and 450 ˚C FG-ALD TiO_2 NWs.

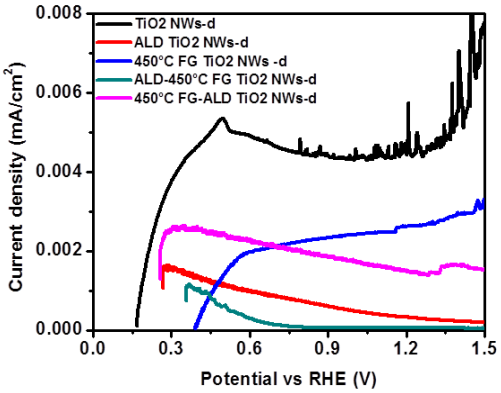

Figure 2.7 Dark current density of typical TiO_2 NWs, ALD TiO_2 NWs, ALD-450 ˚C FG TiO_2 NWs and 450 ˚C FG-ALD TiO_2 NWs.

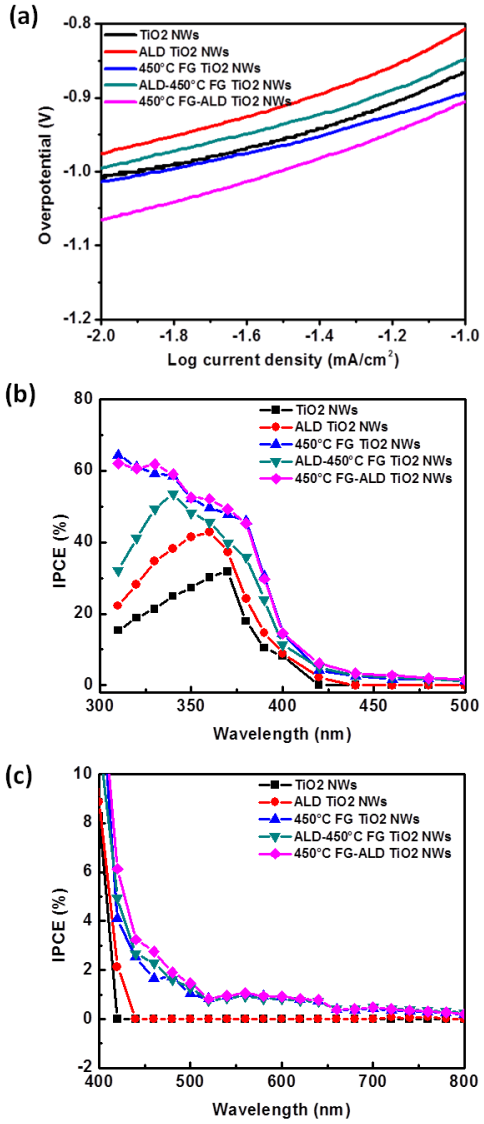

Figure 2.8 Tafel plots (a) and the scale-up IPCE data (b, c) of typical TiO_2 NWs and different post growth treated TiO_2 NWs. (b) and (c) indicate the scale-up IPCE data in the wavelength range of 300~500 nm and 400~800 nm, respectively.

As mentioned earlier, 450 ˚C FG TiO_2 NWs had low FF due to increased resistance of FTO substrate by FG treatment. Also, the dark current density of FG TiO_2 NWs further increased along with more positively applied bias (Figure 2.7) but the value was lower than that of TiO_2 NWs. However, despite low FF, 450 ˚C FG TiO_2 NWs

exhibited 0.45 % of efficiency mainly due to much higher J_{sc} which is about three times higher than that of TiO_2 NWs and two times higher than that of ALD TiO_2 NWs as shown in Figure 2.6. Also, Tafel slope of 450 ˚C FG TiO_2 NWs (124 mV/decade) was lower than that of TiO_2 NW in Figure 2.8 showing higher electrical conductivity for efficient charge separation and transportation. Moreover, they indicated much improved IPCE value in the whole UV region (~60 % of the maximum value at 300nm) which mainly contributed to much higher J_{sc}, and exhibited few % even in visible light range where TiO_2 NWs and ALD TiO_2 NWs did not show any IPCE value (Figure 2.6c and 2.8). The enhancement of IPCE value in the entire UV region, especially at shorter wavelength, confirmed that FG treatment increased the mobility of photo-induced majority carrier by suppression of recombination loss thereby improved short wavelength absorption, which was also verified by the IPCE data of both ALD-FG TiO_2 NWs and FG-ALD TiO_2 NWs. It was reported that both TiO_2 NWs and hydrogen treated TiO_2 NWs have similar nature of the trap states but under a positive applied bias, hydrogen treated TiO_2 NWs dramatically decreases the width of the space charge layer due to higher donor density, which leads to large band bending and effective spatial charge separation thereby high initial charge carrier yields [27]. With dark color of the sample and XPS data, IPCE values of FG TiO_2 NWs in visible light range support that FG treatments created a high density of oxygen vacancies below the conduction band edge to make TiO_2 NWs visible light responsive[26].

Interestingly, both processes-treated samples with different sequence, ALD - 450 ˚C FG TiO_2 NWs and 450 ˚C FG - ALD TiO_2 NWs, indicated different PEC water oxidation performance (Figure 2.6). They similarly exhibited very low dark current

which further decreased with the increased applied bias like ALD TiO_2 NWs (Figure 2.7). However, although they indicated much better PEC water oxidation performance than as-grown TiO_2 NWs and ALD TiO_2 NWs, both samples showed lower efficiency than 450 ˚C FG TiO_2 NWs. Mainly due to smaller J_{sc}, ALD - 450 ˚C FG TiO_2 NWs had smaller efficiency as we expected. This is because ALD - 450 ˚C FG TiO_2 NWs have no thinner NWs to expose to forming gas leading to insufficient FG treatment effects. Nonetheless, compared to ALD TiO_2 NWs, ALD - 450 ˚C FG TiO_2 NWs exhibited not only superior efficiency due to increased J_{sc} and FF but also improved IPCE value at shorter wavelength with visible light response. These results imply that FG treatment enhanced the electrical conductivity even if its effect was insufficient in ALD - 450 ˚C FG TiO_2 NWs. On the other hand, 450 ˚C FG - ALD TiO_2 NWs had improved J_{sc} than that of 450 ˚C FG TiO_2 NWs but they had poorer efficiency due to much low FF possibly because ALD layer blocked black thinner NWs in each TiO_2 bundle to expose to electrolyte for water oxidation reactions. Like ALD TiO_2 NWs, they also need high bias as a driving force for charge separation in bulk. Therefore, in comparison with 450 ˚C FG TiO_2 NWs, 450 ˚C FG - ALD TiO_2 NWs had higher Tafel slope (160 mV/decade) in Figure S3 and smaller photocurrent density at lower bias. Also, the maximum power exhibited at higher bias. However, FG-ALD TiO_2 NWs show a minute amount of increase in IPCE value compared to FG TiO_2 NWs. As mentioned above, this also suggests that FG treatment can enhance the short wavelength absorption typically due to reduced recombination, which is also proved by the ALD then FG treatment sample. In our study, FG treatment effect was more efficient than ALD coating effect. FG treatment and ALD coating can improve IPCE value at the shorter wavelength by different means. ALD layer acts as a

protecting layer to passivate defect sites of TiO_2 NWs surface leading to increased charge collection efficiency by completely covering ultrathin secondary NWs of TiO_2 NWs which can be charge trapping sites at their interfaces. On the other hand, FG treatment increases donor density by generating oxygen vacancies below the conduction band edge leading to large band bending and effective spatial charge separation thereby high initial charge carrier yields in the whole UV region. Also, FG treatment makes TiO_2 NWs visible light responsive.

2.4 Conclusion

To improve PEC water splitting performances of hydrothermally grown rutile TiO_2 NWs, we have further modified TiO_2 NWs with ALD coating or FG treatment or both post growth treatment processes and investigated their effects. FG treatment increases donor density in TiO_2 NWs by the formation of oxygen vacancies, which gives rise to more efficient charge separation and transportation leading to much higher IPCE value and J_{sc}. On the other hand, the additional ALD layer indicates two opposite effects on PEC performances of TiO_2 NWs. One is playing a protecting layer that passivates defect sites of TiO_2 NWs surface leading to increased charge collection efficiency. The other is acting a blocking layer that prevents secondary thinner NWs in each TiO_2 bundle from reacting with water-based electrolyte during PEC performance test or reacting with FG gas in second FG treatment. Therefore, TiO_2 NWs and FG TiO_2 NWs with ALD layer exhibited similar or smaller efficiency due to very low FF despite improved J_{sc} and IPCE value. Therefore both types and sequences of post growth treatments should be carefully considered to improve the properties and performances of TiO_2 NWs.

2.5 Note

This chapter, in full, is currently being prepared for submission for publication of the Journal of Physical Chemistry C. Sun Young Noh, Ke Sun, Shaohua Shen, Sung J. Kim, Xiaoqing Pan, Sungho Jin, and Deli Wang. The dissertation author was the primary researcher and the first author of this paper.

2.6 References

1. Walter, M.G., Warren, E.L., McKone, J.R., Boettcher, S.W., Mi, Q. Santori, E.A., and Lewis, N.S., Solar Water Splitting Cells. *Chemical Reviews* **110**, 6446-6473 (2010).

2. Leempoel, P., Castro-Acuna, M., Fan, F.-R.F. & Bard, A.J. Semiconductor electrodes. 43. The effect of light intensity and iodine doping on the stabilization of n-silicon by phthalocyanine films. *The Journal of Physical Chemistry* **86**, 1396-1400 (1982).

3. Hanna, M.C. & Nozik, A.J. Solar conversion efficiency of photovoltaic and photoelectrolysis cells with carrier multiplication absorbers. *Journal of Applied Physics* **100**, 074510-074518 (2006).

4. Bak, T., Nowotny, J., Rekas, M. & Sorrell, C.C. Photo-electrochemical hydrogen generation from water using solar energy. Materials-related aspects. *International Journal of Hydrogen Energy* **27**, 991-1022 (2002).

5. Bard, A.J. & Fox, M.A. Artificial Photosynthesis: Solar Splitting of Water to Hydrogen and Oxygen. *Accounts of Chemical Research* **28**, 141-145 (1995).

6. Fujishima, A. & Honda, K. Electrochemical Photolysis of Water at a Semiconductor Electrode. *Nature* **238**, 37-38 (1972).

7. Wrighton, M.S. Photoelectrochemical conversion of optical energy to electricity and fuels. *Accounts of Chemical Research* **12**, 303-310 (1979).

8. Amouyal, E. Photochemical production of hydrogen and oxygen from water: A review and state of the art. *Solar Energy Materials and Solar Cells* **38**, 249-276 (1995).

9. Takabayashi, S., Nakamura, R. & Nakato, Y. A nano-modified Si/TiO2 composite electrode for efficient solar water splitting. *Journal of Photochemistry and Photobiology A: Chemistry* **166**, 107-113 (2004).

10. Neumann, B., Bogdanoff, P., Tributsch, H., Sakthivel, S. & Kisch, H. Electrochemical Mass Spectroscopic and Surface Photovoltage Studies of Catalytic Water Photooxidation by Undoped and Carbon-Doped Titania. *The Journal of Physical Chemistry B* **109**, 16579-16586 (2005).

11. Imanishi, A., Okamura, T., Ohashi, N., Nakamura, R. & Nakato, Y. Mechanism of Water Photooxidation Reaction at Atomically Flat TiO2 (Rutile) (110) and (100) Surfaces: Dependence on Solution pH. *Journal of the American Chemical Society* **129**, 11569-11578 (2007).

12. Mohapatra, S.K., Misra, M., Mahajan, V.K. & Raja, K.S. Design of a Highly Efficient Photoelectrolytic Cell for Hydrogen Generation by Water Splitting: Application of TiO2-xCx Nanotubes as a Photoanode and Pt/TiO2 Nanotubes as a Cathode. *The Journal of Physical Chemistry C* **111**, 8677-8685 (2007).

13. Shankar, K., Basham, J.I., Allam, N.K., Varghese, O.K., Mor, G.K., Feng, X., Paulose, M., Seabold, J.A. Choi, K., and Grimes, C.A., Recent Advances in the Use of TiO2 Nanotube and Nanowire Arrays for Oxidative Photoelectrochemistry. *The Journal of Physical Chemistry C* **113**, 6327-6359 (2009).

14. Nakata, K. & Fujishima, A. TiO2 photocatalysis: Design and applications. *Journal of Photochemistry and Photobiology C: Photochemistry Reviews* **13**, 169-189 (2012).

15. Wang, H.E., Chen, Z., Leung, Y.H., Luan, C., Liu, C., Tang, Y., Yan, C., Zhang, W., Zapien, J.A., Bello, I., and Lee, S. Hydrothermal synthesis of ordered single-crystalline rutile TiO2 nanorod arrays on different substrates. *Applied Physics Letters* **96**, 263104-263103 (2010).

16. Cho, I.S., Chen, Z., Forman, A.J., Kim, D.R., Rao, P.M., Jaramillo, T.F., and Zheng, X., Branched TiO2 Nanorods for Photoelectrochemical Hydrogen Production. *Nano Letters* **11**, 4978-4984 (2011).

17. Sedach, P.A., Gordon, T.J., Sayed, S.Y., Furstenhaupt, T., Sui, R., Baumgartner, T., and Berlinguette, C.P., Solution growth of anatase TiO2 nanowires from transparent conducting glass substrates. *Journal of Materials Chemistry* **20**, 5063-5069 (2010).

18. Zhou, H., Qu, Y., Zeid, T. & Duan, X. Towards highly efficient photocatalysts using semiconductor nanoarchitectures. *Energy Environ. Sci.* **5**, 6732-6743 (2012).

19. Hochbaum, A.I. & Yang, P. Semiconductor Nanowires for Energy Conversion. *Chemical Reviews* **110**, 527-546 (2009).

20. Chen, X. & Burda, C. The Electronic Origin of the Visible-Light Absorption Properties of C-, N- and S-Doped TiO2 Nanomaterials. *Journal of the American Chemical Society* **130**, 5018-5019 (2008).

21. Gomes Silva, C.u., Juárez, R., Marino, T., Molinari, R. & García, H. Influence of Excitation Wavelength (UV or Visible Light) on the Photocatalytic Activity of Titania Containing Gold Nanoparticles for the Generation of Hydrogen or Oxygen from Water. *Journal of the American Chemical Society* **133**, 595-602 (2010).

22. Hensel, J., Wang, G., Li, Y. & Zhang, J.Z. Synergistic Effect of CdSe Quantum Dot Sensitization and Nitrogen Doping of TiO2 Nanostructures for Photoelectrochemical Solar Hydrogen Generation. *Nano Letters* **10**, 478-483 (2010).

23. Hoang, S., Berglund, S.P., Hahn, N.T., Bard, A.J. & Mullins, C.B. Enhancing Visible Light Photo-oxidation of Water with TiO2 Nanowire Arrays via Cotreatment with H2 and NH3: Synergistic Effects between Ti3+ and N. *Journal of the American Chemical Society* **134**, 3659-3662 (2012).

24. Noh, S.Y., Sun, K., Choi, C., Niu, M., Yang, M., Xu, K., Jin, S., and Wang, D., Branched TiO2/Si nanostructures for enhanced photoelectrochemical water splitting. *Nano Energy* **2**, 351-360 (2013).

25. Chen, X., Liu, L., Yu, P.Y. & Mao, S.S. Increasing Solar Absorption for Photocatalysis with Black Hydrogenated Titanium Dioxide Nanocrystals. *Science* **331**, 746-750 (2011).

26. Wang, G., Wang, H., Ling, Y., Tang, Y., Yang, X., Fitzmorris, R. C., Wang, C., and Zhang, J.Z., Hydrogen-Treated TiO2 Nanowire Arrays for Photoelectrochemical Water Splitting. *Nano Letters* **11**, 3026-3033 (2011).

27. Pesci, F.M., Wang, G., Klug, D.R., Li, Y. & Cowan, A.J. Efficient Suppression of Electron–Hole Recombination in Oxygen-Deficient Hydrogen-Treated TiO2 Nanowires for Photoelectrochemical Water Splitting. *The Journal of Physical Chemistry C* (2013).

28. Law, M., Greene, L.E., Radenovic, A., Kuykendall, T., Liphardt, J., and Yang, P., ZnO−Al2O3 and ZnO−TiO2 Core−Shell Nanowire Dye-Sensitized Solar Cells. *The Journal of Physical Chemistry B* **110**, 22652-22663 (2006).

29. Le Formal, F., Tetreault, N., Cornuz, M., Moehl, T., Gratzel, M. and Sivula, K., Passivating surface states on water splitting hematite photoanodes with alumina overlayers. *Chemical Science* **2**, 737-743 (2011).

30. Kargar, A., Sun, K., Jing, Y., Choi, C., Jeong, H., Jung, G.Y., Jin, S., and Wang, D., 3D Branched Nanowire Photoelectrochemical Electrodes for Efficient Solar Water Splitting. *ACS Nano* **7**, 9407-9415 (2013).

31. Hwang, Y.J., Hahn, C., Liu, B. & Yang, P. Photoelectrochemical Properties of TiO2 Nanowire Arrays: A Study of the Dependence on Length and Atomic Layer Deposition Coating. *ACS Nano* **6**, 5060-5069 (2012).

32. Sun, K., Park, N., Sun, Z., Zhou, J., Wang, J., Pang, X., Shen, S., Noh, S. Y., Jing, Y., Jin, S., Yu, P.K.L., and Wang, D., Nickel oxide functionalized silicon for efficient photo-oxidation of water. *Energy & Environmental Science* (2012).

33. Xu, M., Da, P., Wu, H., Zhao, D. & Zheng, G. Controlled Sn-Doping in TiO2 Nanowire Photoanodes with Enhanced Photoelectrochemical Conversion. *Nano Letters* **12**, 1503-1508 (2012).

34. Zhang, Q., Li, Y., Ackerman, E.A., Gajdardziska-Josifovska, M. & Li, H. Visible light responsive iodine-doped TiO2 for photocatalytic reduction of CO2 to fuels. *Applied Catalysis A: General* **400**, 195-202 (2011).

35. Das, S., Kim, D.-Y., Choi, H.-S. & Hahn, Y.-B. Studying trivalent/bivalent metal ion doped TiO2 as p-TiO2 in bipolar heterojunction devices. *Materials Chemistry and Physics* **129**, 887-891 (2011).

36. Abazovic, N., Mirenghi, L., Jankovic, I., Bibic, N., Sojic, D., Abramovic, B., and Comor, M., Synthesis and Characterization of Rutile TiO2Nanopowders Doped with Iron Ions. *Nanoscale Research Letters* **4**, 518 - 525 (2009).

37. Purvis, K.L., Lu, G., Schwartz, J. & Bernasek, S.L. Surface Characterization and Modification of Indium Tin Oxide in Ultrahigh Vacuum. *Journal of the American Chemical Society* **122**, 1808-1809 (2000).

38. Nassoko, D., Li, Y.F., Wang, H., Li, J.L., Li, Y.Z., and Yu, Y., Nitrogen-doped TiO2 nanoparticles by using EDTA as nitrogen source and soft template: Simple preparation, mesoporous structure, and photocatalytic activity under visible light. *Journal of Alloys and Compounds* **540**, 228-235 (2012).

39. Sathish, M., Viswanathan, B. & Viswanath, R.P. Characterization and photocatalytic activity of N-doped TiO2 prepared by thermal decomposition of Ti–melamine complex. *Applied Catalysis B: Environmental* **74**, 307-312 (2007).

40. Chen, X., Liu, L., Liu, Z., Marcus, M.A., Wang, W.C., Oyler, N.A. Grass, M.E., Mao, B., Glans, P.A., Yu, P.Y., Guo, J., and Mao, S.S., Properties of Disorder-Engineered Black Titanium Dioxide Nanoparticles through Hydrogenation. *Sci. Rep.* **3** (2013).

41. Shi, J. & Wang, X. Hierarchical TiO2-Si nanowire architecture with photoelectrochemical activity under visible light illumination. *Energy & Environmental Science* **5**, 7918-7922 (2012).

42. Liu, S.Y., Sheu, J.K., Lee, M.L., Lin, Y.C., Tu, S.J., Huang, F.W., and Lai, W.C., Immersed finger-type indium tin oxide ohmic contacts on p-GaN photoelectrodes for photoelectrochemical hydrogen generation. *Optics Express* **20**, A190-A196 (2012).

CHAPTER 3: Branched TiO_2/Si Nanostructures for Enhanced Photoelectrochemical Water Splitting

3.1 Introduction

Since the first practical demonstration of photoelectrochemical (PEC) water splitting using a TiO_2-based photocatalyst [1], research efforts have been focused on various semiconducting materials and structures for efficient light harvesting, high quantum efficiency, enhanced PEC water splitting performance, as well as practical durability and low cost manufacturing [2-10]. In particular, photoelectrodes based on dimension-controllable and highly ordered metal oxide nanostructure array [6, 8, 11-13] have attracted much attention for PEC applications. Such nanostructures offer a unique combination of the large surface areas/reaction sites, increased optical path lengths and thus low reflection, direct electronic carrier transport pathways, and short lateral diffusion length due to their one-dimensional (1D) nanostructures.

Additional advantages such as superior chemical stability, ease of fabrication, and relative low cost inherited from oxide materials have also been noted. However, most metal oxides such as TiO_2, ZnO, and WO_3 have wide bandgaps, leading to a limited light absorption in the visible region of solar spectrum, unfavorable band positions with respect to the water oxidation and reduction levels, low electron mobility, and rapid electron-hole pair recombination [5]. To resolve these issues of metal oxide photoelectrodes, various investigations have been performed on metal/cation/anion doping, dye/quantum dot sensitization, metal ion-implantation, and heterojuction [14-17].

Among the aforementioned techniques, the heterojunction electrode approach utilizes two different semiconductors that form a hetero-junction allowing enhanced light absorption and charge collection efficiency, which can also take advantage of electrochemically robust materials to improve photoelectrochemical corrosion stability[18-23].

Si is the most important and broadly used semiconductor in electronic and optoelectronic devices, which is also abundant and generally of low cost. Si is a desirable photoelectrode material for PEC applications because it has a narrow band gap, absorbs light efficiently, and has easily controllable electrical conductivity [3, 24, 25]. However, Si has poor chemical stability because it is rapidly oxidized in aqueous solution under solar illumination or under anodic bias [26]. On the other hand, TiO_2 has been extensively studied as photoanode material due to its superior chemical stability as well as photochemical and photocatalytic properties [7, 27, 28]. However, it absorbs sunlight only in the UV region and collects less than 5% of the total energy available in the solar spectrum [5, 12] and thus offers a limited PEC performance. Therefore, a heterogeneous integration of Si and TiO_2 could combine their advantageous properties for PEC with good chemical stability and efficient light absorption.

Compared to a planar structure, a vertically oriented nanowire (NW) array exhibits a significant advantage of enhanced light absorption and energy conversion efficiency due to the following reasons [3, 29-32]. First, vertically oriented NW array provides a reduced reflection and thus enhanced sunlight absorption due to their light trapping properties. Second, the aligned NWs can orthogonalize the light absorption and the carrier collection processes due to the reduced competition between photon absorption and carrier collection, and short diffusion length of minority carriers. Third,

the NWs also provide a larger internal surface area and reaction sites to improve the charge transfer and PEC reaction kinetics. In this regard, the core/shell NW (cs-NW) and three-dimensional (3D) branched NW (b-NW) heterostructures are very attractive photoelectrodes. Such structures offer combined advantages of heterojunction and 1D nanostructures [10, 33, 34]. The 3D b-NW heterostructures could offer greatly increased surface area and more enhanced light absorption in NW branches compared to the cs-NW heterostructures.

In this article, we report a successful fabrication of three-dimensional (3D) TiO_2/Si based branched NW arrays by a combination of nanoimprint lithography (NIL), reactive ion etching (RIE), and hydrothermal reactions. The b-NW structures were characterized using scanning electron microscopy (SEM), high-resolution transmission electron microscopy (HR-TEM), and X-ray diffraction (XRD). The TiO_2/Si b-NW arrays, in comparison with TiO_2/Si cs-NW arrays, with various Si NW lengths were studied as photoanodes for PEC water splitting. A working mechanism based on charge transfer and recombination at the n-n TiO_2/Si heterojunction is proposed.

3.2 Experiments

3.2.1 Preparation of vertical Si nanowire (NW) arrays

N-type (100) polished silicon wafers (University Wafer, phosphorus doped, 0.3~0.5 Ω-cm resistivity) were cleaned by 10% nitric acid, acetone, isopropanol alcohol (IPA), deionized (DI) water, and blow-dried by nitrogen gas. Vertical Si NW arrays were fabricated by combining nanoimprint lithography (NIL) and reactive ion etching (RIE) processes[35-37]. Specifically, a polymethylmethacrylate (PMMA, Micro Resist

Technology, mr-I35k PMMA 300) layer was spin-coated and baked. The NIL was carried out at 175 ℃ using an ANT-2 nano-imprinter machine using a mould consisting of islands having 500 nm diameter and 500 nm spacing. After imprinting, the residual imprint polymer was removed by RIE (Oxford instrument, Plasmalab 80 RIE system). An array of Ni dots, later to be used as RIE etch masks, were defined by a deposition of 40-nm Ni thin film on the nanoimprinted PMMA/Si substrate by an E-beam evaporator (Temescal, BJD 1800 E-beam Evaporator) and subsequently lift-off processed using acetone. Si NW arrays with different lengths were fabricated by RIE (Oxford instrument, Plasmalab 100 RIE/ICP system) using different etching time. In order to achieve vertical un-isotropic etching, sulfur hexafluoride (SF_6) was used as etchant while octafluorocyclobutane (C_4F_8) was added to passivate the sidewalls and suppress lateral etching of the silicon NWs. The nickel etch mask was chemically removed after RIE using a Ni etchant solution. Prior to the TiO_2 coating, the surface of Si NW arrays was cleaned - the Si NW array were annealed in oxygen at 600 ℃ for 1 h, etched in HF solution, and cleaned using the standard RCA procedure.

3.2.2 Fabrication of core/shell and branched TiO_2/Si NWs arrays

To fabricate a TiO_2 thin film-coated Si NW (core/shell TiO_2/Si NW, cs-NW) array, a thin layer of TiO_2 was deposited on the vertical Si NWs using RF magnetron sputtering (Denton Discovery, 18 Sputter System) at 400 W under 15 mTorr in an argon environment, and annealed at 400 ℃ for 30 min in nitrogen atmosphere. The TiO_2 thin film coating on Si NW surface serves as shells and also as a seeding layer for the growth of 3D branched TiO_2/Si NWs.

Branched TiO_2/Si NW (or TiO_2/Si b-NW) arrays were prepared by a hydrothermal reaction [38]. For hydrothermal processing solution, 1 ml of titanium n-butoxide (Alfa Aesar), the titanium precursor, was added drop-wise to a 1:1 mixture of DI water and concentrated hydrochloric acid (EMD chemicals) and stirred to obtain a clear transparent solution. The core/shell TiO_2/Si NW arrays were placed in the growth solution in a stainless steel autoclave with Teflon liner (Parr instrument), and then sealed and maintained at 155 ℃ for the growth of TiO_2 branches for various time periods. After the hydrothermal reaction, the samples were removed from the solution, rinsed with ethanol, and dried with nitrogen gas, and followed by annealing at 400 ℃ for 30min in nitrogen atmosphere. Figure 3.1 shows a schematic diagram outlining the fabrication process of vertical Si NW arrays, core/shell and branched TiO_2/Si NW arrays.

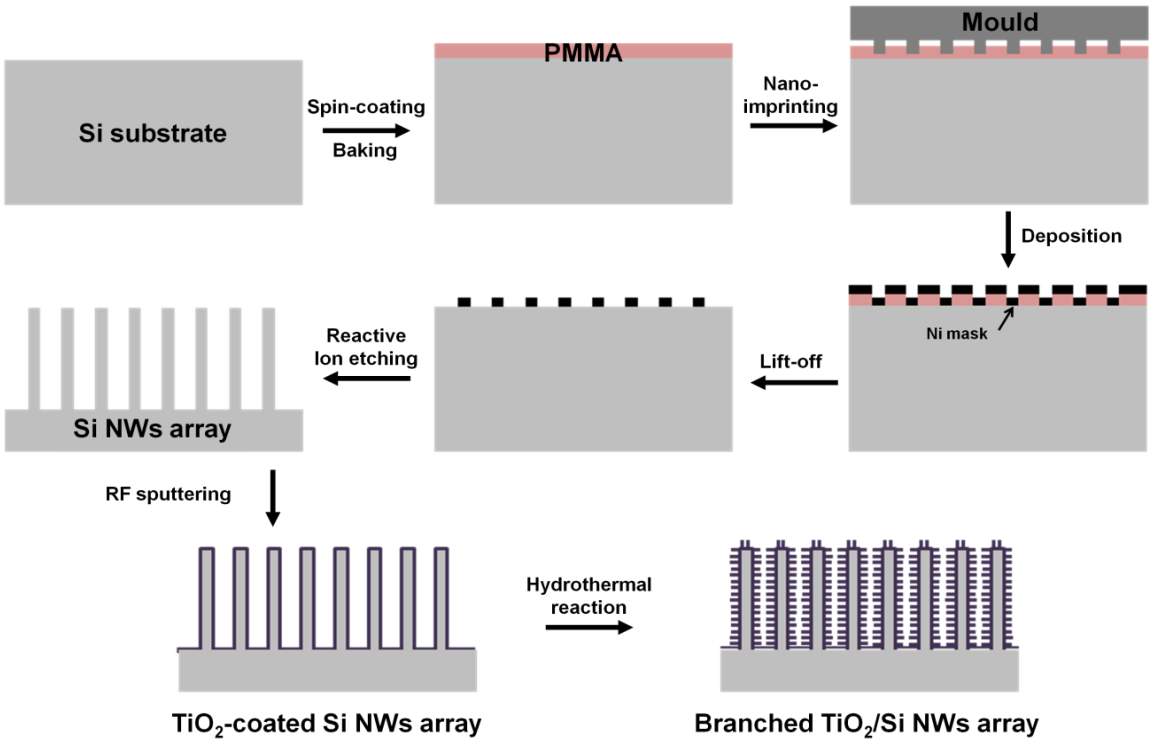

Figure 3.1 Schematic of the fabrication process of TiO_2 thin film-coated Si NWs array and 3D branched TiO_2/Si NWs array.

3.2.3 Materials characterization and PEC performance measurements

A high-resolution scanning electron microscope (SEM, FEI XL30-SFEG) was employed to examine the NW morphology. The crystalline structures of TiO_2 NWs hydrothermally grown on Si substrate were further characterized by X-ray diffraction (XRD, Rigaku Multiflex X-ray diffractometer) with Cu-Kα radiation (λ = 1.54 Å) scanning at a rate of 0.05° s^{-1}. Transmission electron microscopy (TEM, FEI Tecnai G2 F20 S-Twin) was carried out with 200 kV accelerating voltage (SINANO, China). For the TEM measurements, the TiO_2/Si b-NWs were scraped off from the substrate and dispersed in IPA using sonication, and a drop of the resulting suspension was then applied on a nickel TEM grid.

The optical transmittance of hydrothermally grown TiO_2 NWs on sapphire substrate was measured by using a monochromator (Horiba Jobin Yvon, iHR 550) equipped with a 150 W Xenon lamp as an illumination source, from which the optical band gap was extrapolated. A lock-in amplifier (Stanford Research, SR530) was used to isolate the signal component specifically from the incident illumination. A pre-amp (Ithaco 1211 current preamplifier) with various gains depending on the current levels was also used. The transmitted light spectrum of the monochromatic illumination was calibrated using a Si p-i-n photodiode (Newport, 818-UV).

PEC performance measurements were carried out in a 0.25 M Na_2SO_4 electrolyte (pH = 7.2) buffered with phosphate buffered saline (PBS) in a three-electrode configuration [39], where the TiO_2/Si cs-NW or b-NW array based photoanode serves as the working electrode, a platinum mesh as the counter electrode, and Ag/AgCl (with 1 M KCl) as the reference electrode. All three electrodes were in a glass apparatus with a quartz window, through which the photoanodes were illuminated by a solar simulator (Newport) equipped with a 150 W Xe lamp and an AM 1.5 filter (100 mW/cm^2). During the measurement, the electrolyte solution is saturated with nitrogen gas to remove the dissolved oxygen and carbon dioxide. Steady-state current density-voltage (J–V) measurements were performed using a potentiostat (Digi-ivy Inc., DY2300) with a sweep rate of 10 mV/s and all data were recorded using software DY2300.

Photocurrent spectrum responses of the TiO_2/Si b-NW array under a constant bias (2.0 V vs. RHE) were collected using a potentiostat (Digi-ivy Inc., DY2300) in conjugation with a monochromator (Horiba Jobin Yvon, iHR 550) equipped with a 150 W xenon lamp for the short wavelength range of 300-500 nm, while a 100 W halogen

lamp was utilized for the longer wavelength range of 500-1100 nm. Prior to the measurements, the intensity of the monochromated light was calibrated using a Si photodetector (Newport) in the wavelength range utilized. To obtain a steady-state photocurrent as well as dark current, a sufficiently low frequency of light chopping was used to allow the system to stabilize. The average steady-state current values were then used to calculate the incident photon to current conversion efficiencies (IPCEs).

3.3 Results and Discussion

3.3.1 Morphologies of vertical Si NW arrays and TiO_2/Si cs-NW arrays

Figure 3.2 shows the cross-sectional SEM images of vertical Si NW arrays of different lengths as well as the corresponding TiO_2/Si cs-NWs. The morphology of the Si NW array depends on both the nanoimprint mold dimension and the RIE conditions such as the type and flow rate of the gases employed and RIE etching time [35]. In this study, we only varied the RIE etching time to effectively control the length of the Si NWs. As shown in Figures 1a-1c, cylindrical Si NWs with length of ~1.2 μm, ~2.5 μm, and ~5 μm were obtained by 5 min, 10 min, and 20 min etching, respectively. Figures 1d-1f show the higher magnification SEM images. After 5 min and 10 min RIE etching, the Si NWs showed a quite uniform cylindrical shape with a smooth sidewall surface (no scalloping) with typical dimensions of ~330 nm in diameter and ~670 nm in spacing (Figures 1d and 1e). On the other hand, Si NWs obtained by a longer time 20 min RIE under the same conditions exhibited a flower-vase shape nanowires with tapered sidewall geometry (~210 nm in diameter at the top and ~330 nm at the bottom) (Figures 1c and 1f). The tapered Si NWs resulted from the longer RIE time can actually enhance the light

absorption, due to the smoother transition of refractive index difference along the nanowire length between air and silicon, resulting in a broad anti-reflective window [29]. An investigation of the effect of such a tapered TiO_2-coated Si nanowire structure on light absorption behavior is beyond the scope of this particular study, and will be studied in a separate investigation.

It is critical to have a uniform TiO_2 coating with well-controlled thickness and quality for preparation of both TiO_2/Si cs-NW and TiO_2/Si b-NWs. First of all, a dense, uniform, and pin-hole free TiO_2 coating on the entire Si NW surfaces is necessary [40, 41] to prevent direct contact of Si to electrolyte, which can cause photo-oxidation of Si and formation of an insulating SiO_2 layer. The thickness of the TiO_2 seeding layer also plays an important role for the hydrothermal reaction because of the lattice mismatch between Si and TiO_2 [42, 43]. When the TiO_2 seeding layer is thin (<30 nm), no TiO_2 NWs were successfully grown. Formation of uniform coating with full coverage on a high-aspect-ratio pillar array feature is very challenging, such as the high-density vertical NW arrays produced in this study. TiO_2 shell layers were coated by RF sputtering in our experiments, which presents additional difficulties. To obtain a successful coating on vertical NWs, the RF power and the gas pressure are very important factors that influence the sputtering rate and the film coating quality [44]. In general, the kinetic energy of the ionized atoms increases as the RF power increases, and thus the ions undergo enhanced back sputtering on the deposited film while traveling through NW length, leading to an increased coating uniformity. However, at low gas flow rates, the incident atoms are preferentially deposited near the top of the NWs due to the diffusion limited process and somewhat line-of-sight limited deposition. Indeed, we have found that a high power of

400 W combined with a high gas flow rate of 15 mTorr produces a denser and more uniform TiO_2 coating, particularly on long Si NWs. As shown in Figures 1g-1i (for the three different nanowire lengthes/heights), a TiO_2 layer with a uniform thickness of 35~40 nm was deposited on the surface of Si NWs as well as on the bottom surface of the flat Si substrate (the space between the neighboring Si pillars). On the other hand, when a high RF power (400 W) is used but at a low gas flow rate (5 mTorr), substantially different diameters were observed on the top vs bottom part of the TiO_2/Si cs-NWs, which is caused by the difference in the thickness of TiO_2 shell coating (pictures not shown).

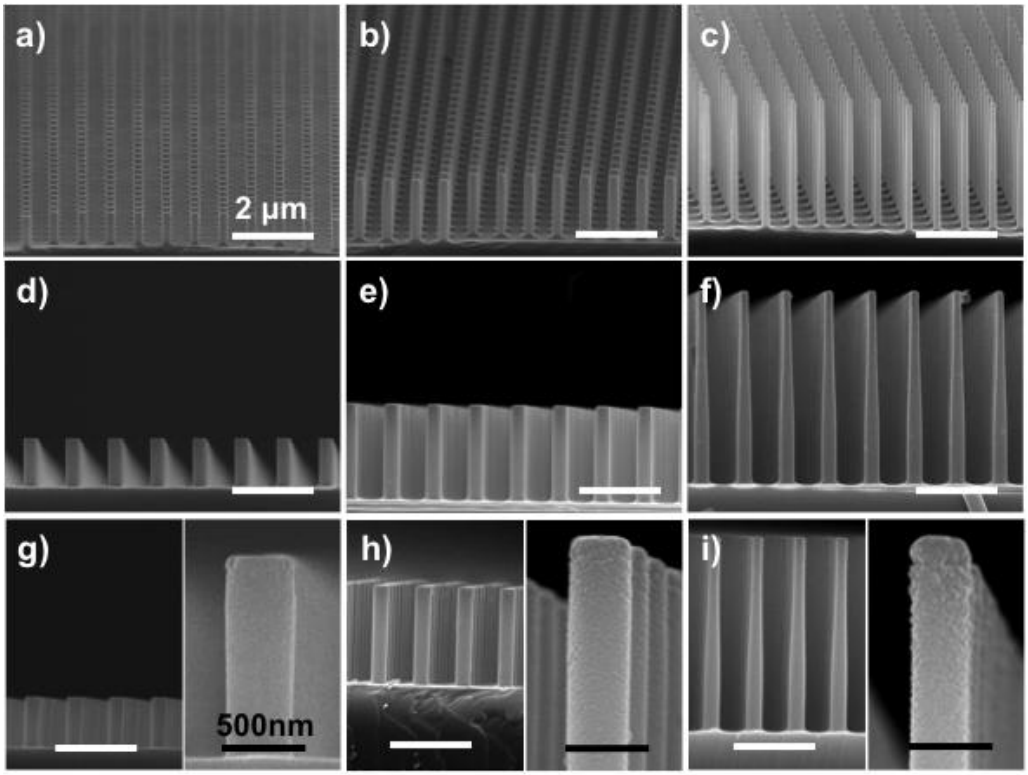

Figure 3.2 Cross-sectional SEM images of Si NW arrays and TiO_2/Si cs-NW arrays with NW lengths of ~1.2μm (a, d, g), ~2.5 μm (b, e, h), and ~5 μm (c, f, i), respectively. g) - i) on the right side of each figure show zoom-in higher magnification views. Scale bars are 200m for all the SEM images, and 500 nm for the zoom-in micrographs.

3.3.2 Morphologies and structures of the TiO_2/Si b-NW arrays

Using the vertical Si NWs with uniform TiO_2 seeding layers (Figure 3.2g-3.2i) as the basis, branched TiO_2 NWs were then grown by hydrothermal reaction. Figure 3.3 shows the top, tilted, and cross-sectional SEM images of the TiO_2/Si b-NWs arrays with different Si NW lengths and TiO_2 NW dimensions. The TiO_2 nanowire dimension was controlled by the reaction time, as well as the precursor concentration, volume, and temperature of reaction solution [42, 45]. To fabricate the high-density TiO_2 NWs on Si NWs of different lengths, the reaction time was varied with other growth parameters kept constant. Figures 3.3a-3.3c show the top view of the TiO_2/Si b-NW arrays where the TiO_2 branches were grown for 50 min, 60 min, and 70 min on Si NWs with length of ~1.2 μm, ~2.5 μm, and ~5 μm, respectively. Figures 3.3d-3.3f and 3.3g-3.3i show the tilted and cross-sectional views. The images at different locations and magnifications reveal that the entire surface of the Si NWs is covered very uniformly with TiO_2 NWs with their orientation nearly perpendicular to the Si NW surfaces as a radial growth. The insets in Figures 3.3g-3.3i indicate that the TiO_2 NWs grown on Si NWs are crystals having a tetragonal wire shape with square top facets. The average diameters of TiO_2 NW branches are in the range of 30~32 nm and almost independent to Si NW lengths (See Figure 4). It was reported that during a hydrothermal reaction the diameter of a newly formed nucleus grows quickly and remains constant for a period of time, while the length increases with time due to the preferential absorption of precursor molecules on the high energy polar surfaces and thus the preferential growth of the length [45-47]. Figure 4 shows statistics and the reaction time dependence of the diameters and lengths of TiO_2 NWs

grown on Si NWs. The TiO_2 branches have an average length of about 280 and 300 nm for 60 min (on ~2.5 □m Si NWs) and 70 min (on ~5 □m Si NWs) growth, respectively, while much longer (~350 nm) branches are obtained for 50 min growth (on ~1.2 μm Si NWs), which is also shown in Figures 3.3a and 3.3g. The longer branches on shorter Si NWs are probably due to the easy access of reactant species to the nucleation sites and the relatively high reactant concentration with respect to both Si NW surface and the number of nucleation sites compared to the longer Si NWs. The use of different branch growth time was to compensate for the limited access to the reactant species and limited diffusion for the case of longer nanowire array configuration, with the hope of growth of similar length of TiO_2 NW branches on Si NWs with different length. In the case of ~5 μm long Si NWs, no significant difference at the top and bottom of the TiO_2/Si b-NW array are observed because the tapered Si NW core geometry is more likely to allow easier access to the reactant solution along the length of the Si NWs (Figures 3.3f and 3.3i).

The structures of the TiO_2/Si b-NWs were further characterized by XRD and TEM. Figure 3.5 shows XRD data of a typical TiO_2 NWs on Si sample, showing an excellent agreement with the diffraction peaks for the standard rutile structured TiO_2 (ICSD No. 064987, $P4_2/mnm$, a = b = 4.5845 Å and c=2.9537 Å). Figure 3.6 shows a TEM image of the TiO_2/Si b-NWs and HRTEM image of a single TiO_2 NW branch. Lattice planes with spacing of 3.3 Å are distinctly visible, corresponding to the interplanar distance of the (110) planes of rutile TiO_2, which is consistent with XRD data. FFT diffraction pattern of a single TiO_2 NW branch with $[\bar{1}\,\bar{1}\,1]$ being the zone axis indicates that the TiO_2 NWs grew along the [112] direction.

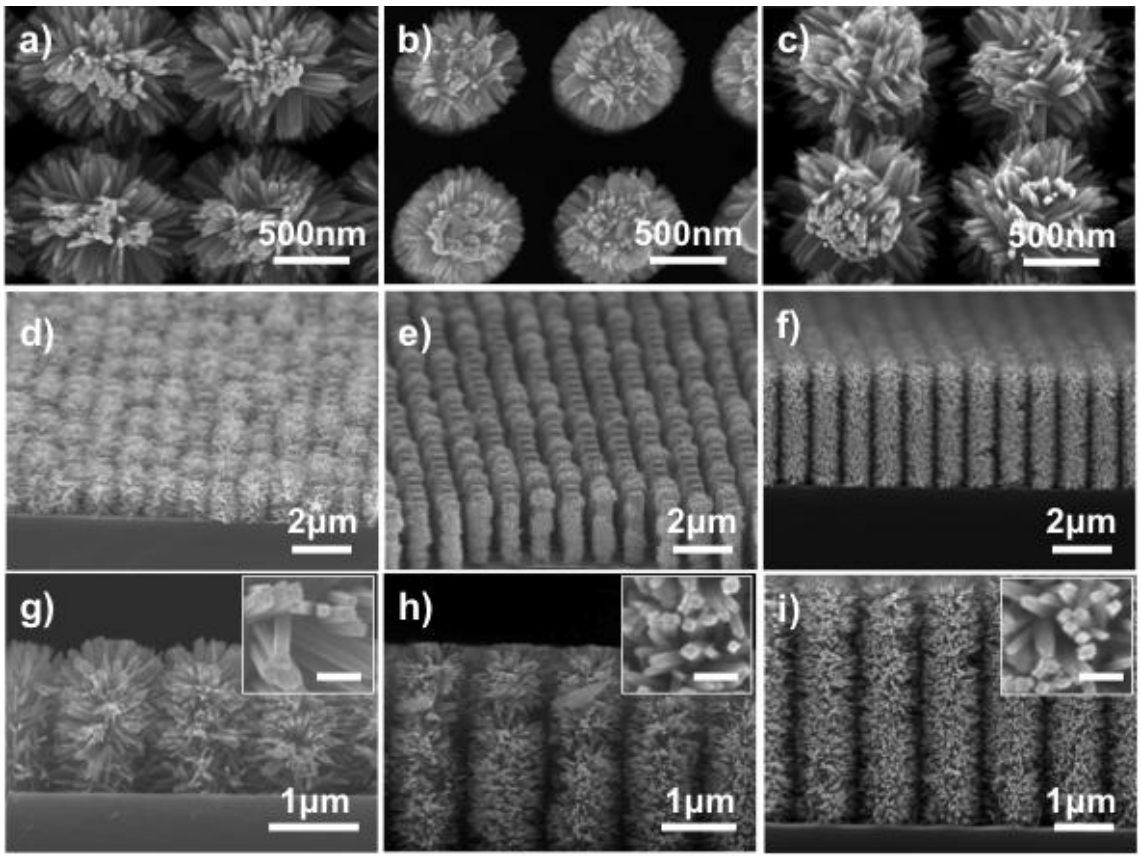

Figure 3.3 SEM images of TiO_2/Si b-NW arrays with Si NWs lengths of a)-c) ~1.2 μm (a, d, g), ~2.5 μm (b, e, h), and ~5 μm (c, f, i), respectively. Insets are higher magnification SEM images and scale bars are 100 nm.

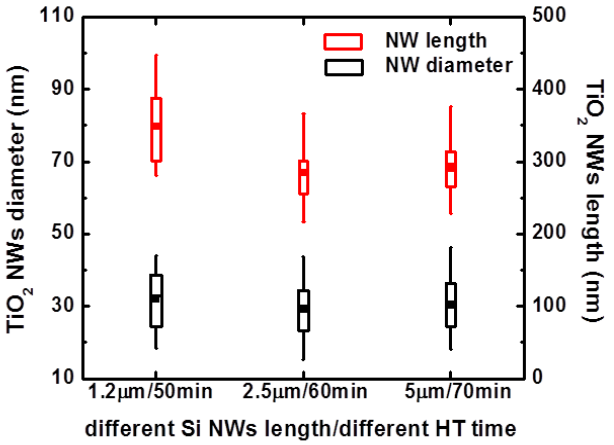

Figure 3.4 Statistics and the reaction time dependence of the diameters and lengths of TiO_2 NWs grown on Si NWs.

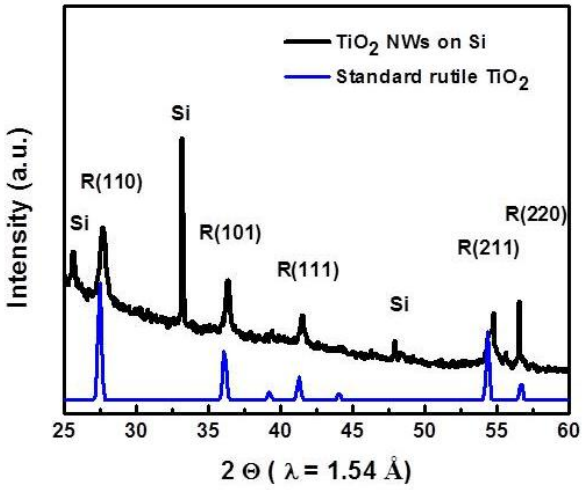

Figure 3.5 XRD pattern of hydrothermally grown TiO_2 NWs on Si substrates, which is compared to that of the standard rutile TiO_2.

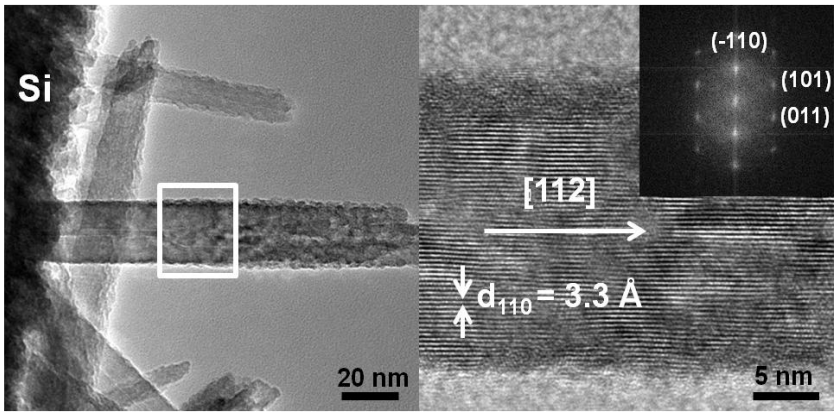

Figure 3.6 LRTEM image of the TiO_2/Si b-NWs and HRTEM image of a TiO_2 NW branch. Inset is FFT diffraction pattern from HRTEM image of a TiO_2 NW branch.

3.3.3 Optical properties of TiO_2 NW arrays grown on Si substrate

The optical properties of TiO_2 NWs were tested on the sample with NWs hydrothermally grown on optically transparent sapphire substrates. Figure 3.7 shows the optical transmittance spectra and Tauc plot of the sample. A noticeable loss of transmittance across the visible region, particularly <600 nm wavelength, was observed. This might come from the surface defect states of TiO_2 NWs indicating the presence of additional energy states within the band gap of TiO_2 [48]. However, the transmittance loss is primarily due to scattering and reflection events, which are two intrinsic optical properties of dense 1D NW arrays [29]. Recent work reported that the reflectance of TiO_2 NWs, hydrothermally grown on FTO substrate, is 20-30% in visible region (>420 nm) while it is almost zero in UV region [49]. From the Tauc plot, the optical bandgap of the TiO_2 NWs are estimated to be about 3.0 eV, which is consist with the reported value for rutile TiO_2 NWs [7, 49]. Figure 3.8 shows the band energy diagram and proposed charge transfer pathway at the TiO_2/Si heterojunction at zero bias under light illumination, with a

band bending considered at the TiO_2/electrolyte interface. The proposed band diagram applies to both the core/shell and branched NWs at the TiO_2/Si heterojunction, while the band diagram in the TiO_2 material away from the junction interface when the TiO_2 branches are long will have symmetric band bending from TiO_2 NW surface to TiO_2 NW center.

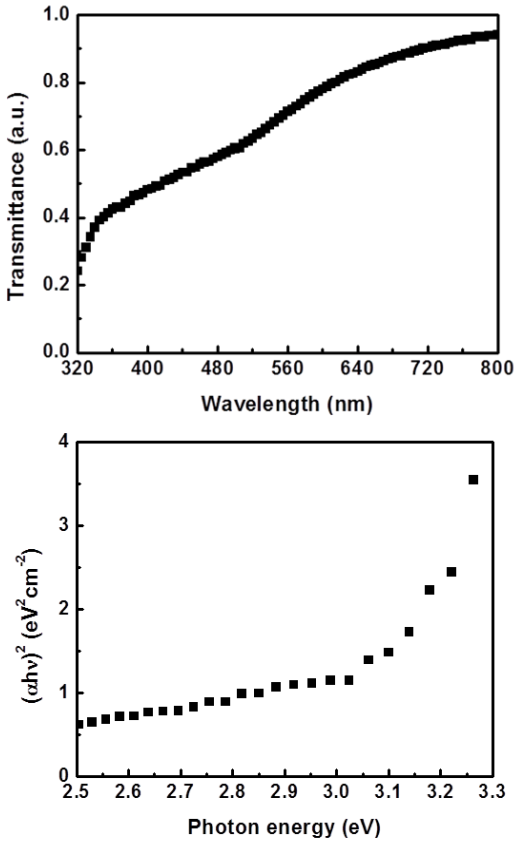

Figure 3.7 The optical transmittance and Tauc plot of TiO_2 NWs hydrothermally grown on sapphire substrate.

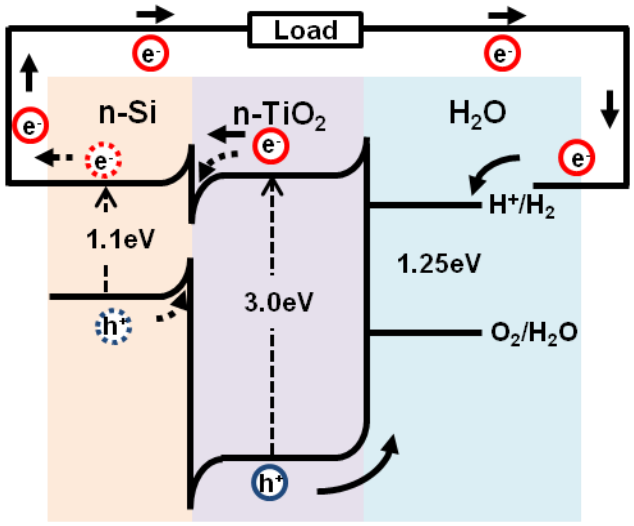

Figure 3.8 Schematics of energy band diagram and charge transfer at the TiO_2/Si heterojunction interface at zero bias under solar illumination.

3.3.4 PEC performances and working mechanism of TiO_2/Si cs-NW and b-NW arrays

Figure 3.9 shows the photocurrent density versus the bias potential characteristics of TiO_2/Si cs-NW and b-NW arrays of different Si NW lengths. The dark current densities of the TiO_2/Si b-NW arrays are higher than that of the corresponding core/shell NW arrays; however, all the samples show a small dark current density of less than 1.2 $\mu A/cm^2$ (not shown), indicating high surface quality of both TiO_2 thin layer and TiO_2 NWs on Si NWs. The photocurrent versus bias potential curves of all samples show two regions: increasing photocurrent density region at bias potentials ranging from the onset potential (TiO_2/Si cs-NW arrays: ~ 0.2 V; TiO_2/Si NWs b-arrays: ~ 0.3 V) to 1.26 V vs. RHE, and plateau at a more positive bias potential (>1.26 V vs. RHE), where the photocurrent is limited by the photogenerated holes in TiO_2. Similarly, the planar TiO_2/Si heterojunction photoelectrodes with same oxide thickness prepared using RF sputtering and tested under identical conditions also show the photocurrent density increasing and

plateau regions, except the plateau occurs at lower positive bias potential of >0.98 V vs. RHE (Figure 3.10). From the increasing photocurrent density region, the photoelectrocatalytic performance of TiO_2/Si cs-NW and b-NW arrays can be further investigated using a Tafel plot (Figure 3.11). The Tafel slope increased from 387 and 334 mV/decade to 846 and 703 mV/decade for cs-NW and b-NW samples, respectively as the length of Si NW backbone increased from ~1.2 μm to 5 μm. In other words, the longer Si NW sample required a higher overpotential to attain a given anodic current. In addition, the Tafel slope of b-NW arrays was smaller compared to the core-shell counterparts with an identical Si NW length, exhibiting a better photoelectrocatalytic performance. However, the Tafel slope remains large presumably due to the interface between n-Si and n-TiO_2, ohmic loss of TiO_2, as well as the mesoporous nature of the TiO_2 film.

The photocurrent characteristics can be understood using the band diagram in Figure 3.8. At zero bias and under light illumination, TiO_2 and Si absorb UV light and visible to near IR light and thus generate electron/hole pairs. On TiO_2 surface or at the TiO_2/electrolyte interface, band bending occurs due to the initial difference in electrochemical potentials, which drives the photogenerated holes in TiO_2 (NW of shell coating) to move toward electrolyte and thus oxidize water to oxygen, while the photogenerated electrons in TiO_2 tunnel through the energy barrier due to band offset and recombine with the holes from Si NW core at the junction interface (Figure 3.8). The electrons generated in Si NW travel from the NW top to bottom, to the Si substrates, and to the counter electrode. In other words, the photocurrent is limited by the recombination at the TiO_2/Si junction. As the biasing voltage increases, the energy barriers at the TiO_2/electrolyte interface as well as at TiO_2/Si interface are reduced and thus the current

increases. However, because the holes generated in the Si NWs are blocked by the large energy barrier due to valance band offset, the photocurrent is limited by the light absorption and photogenerated holes in TiO_2, and thus a photocurrent plateau is reached at higher bias. This is true for the TiO_2/Si photoelectrodes with planar, cs-NW, as well as the b-NW structures.

Figure 3.9a also reveals that the photocurrent density of TiO_2/Si cs-NW arrays decreased with increasing Si NW backbone length, while the onset potential was nearly constant. The TiO_2/Si cs-NW array with Si NWs of ~1.2 μm in length produced the photocurrent density of 0.27 mA/cm^2 at 2 Volts vs. RHE, which was twice and three times of that produced by the samples with ~2.5 μm long Si NWs and ~5 μm long Si NWs, respectively. The decrease in photocurrent vs Si NW length is probably due to the increased electron/hole recombination in TiO_2 by its short hole diffusion length, which reduce the number of electrons participating in the water oxidation reaction at the TiO_2/electrolyte interface. Previous studies showed that depending on the diameter, length, and quality of Si NWs, the carrier generation rate can be different along the vertical Si NW axis via waveguiding and light trapping effect, which influences the diffusion length of both majority and minority carriers leading to either effective or ineffective carrier collection [50, 51]. In addition, longer Si NWs increase the diffusion length of photogenerated carriers before they are collected leading to the increased electron/hole recombination [25, 32]. It can also be due to the fact that the lower part of Si NWs are often coated with somewhat less TiO_2 material, and thus less light absorption and low photogenerated carrier density occur when NWs gets longer. Moreover, for the longer NWs, the reaction rate can be reduced due to limited diffusion.

Figure 3.9b shows the photocurrent characteristics of the 3D TiO_2/Si b-NW array electrodes. In general, the b-NW array electrodes exhibited higher photocurrent densities compared to the core-shell counterparts with identical Si NW length, which is expected by the charge transfer mechanism (Figure 3.8) because the overall photocurrent should be limited by the lowest performing component, TiO_2. Therefore, the enhanced light absorption in TiO_2 NWs by band gap engineering and intentionally increased surface area led to the increased photocatalyzed water splitting efficiency of the b-NW array electrodes [33, 52, 53]. The TiO_2/Si b-NW arrays with ~2.5 μm long Si NW backbones indicated the highest photocurrent density of ~0.36 mA/cm^2 at 2 V vs. RHE, which is 2.8 times higher than that of TiO_2/Si cs-NW arrays without branch TiO_2 nanowires with identical lengths. While the TiO_2/Si b-NW arrays with ~1.2 μm long Si NW showed similar photocurrent compared to the TiO_2/Si cs-NWs array electrodes with the same Si NW length, the photocurrent density of ~5 μm long TiO_2/Si b-NW photoelectrodes increased noticeably by twofold compared to the core-shell counterpart. The fact that there is only a small photocurrent increase for the b-NW photoelectrode with ~2.5 μm long Si NW backbones compared to the electrodes with ~1.2 μm (more than doubled amount of light absorption) may be explained, albeit somewhat speculative. The similar argument for the cs-NW electrodes applies to the b-NWS due to the (i) non-uniform light absorption along the NW axis, (ii) the potential non-uniform growing of TiO_2 branches along the NW axis and reduced light absorption, and (iii) possibly reduced overall reaction rates due to diffusion limits. Note that the increased surface area could possibly have negative effect due to the surface recombination (see Figure 3.12) [25, 32], as the

interface states and surface states density are also recognized as the major loss of the photovoltage and photocurrent [54].

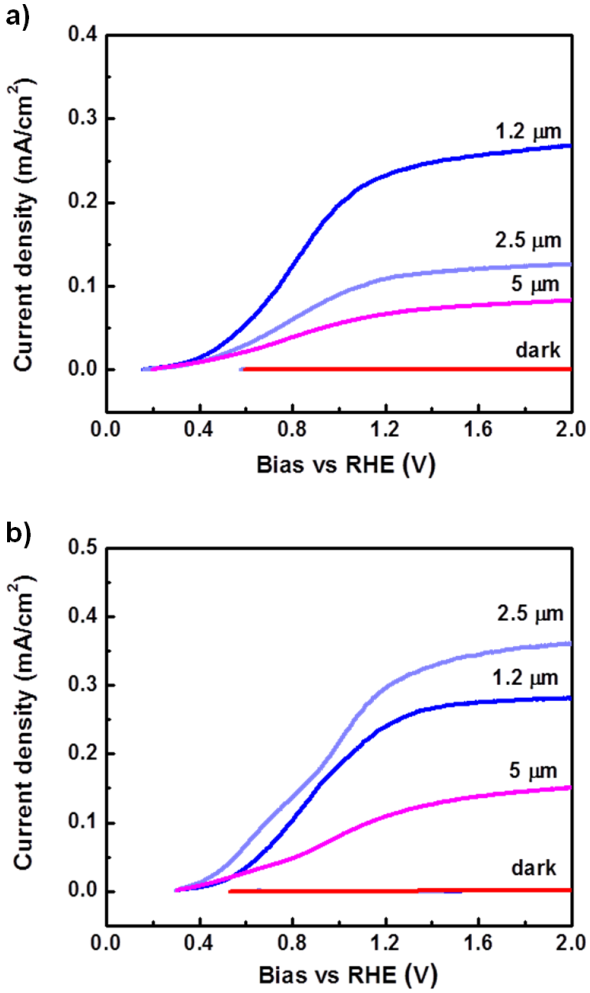

Figure 3.9 Comparison of PEC performance of (a) TiO_2/Si cs-NW and (b) b-NW array based photoelectrodes with different Si NW lengths.

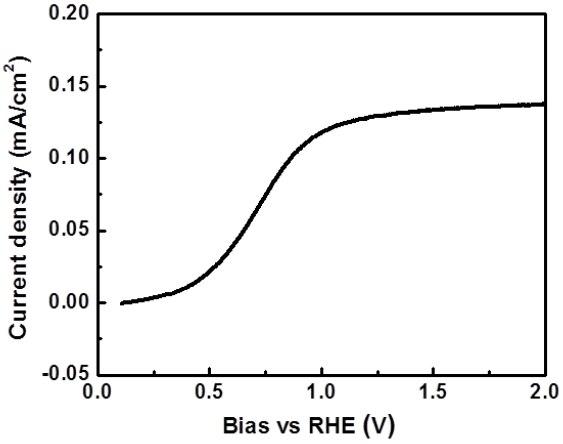

Figure 3.10 Photocurrent density of planar Si substrate with sputtered TiO_2 thin film.

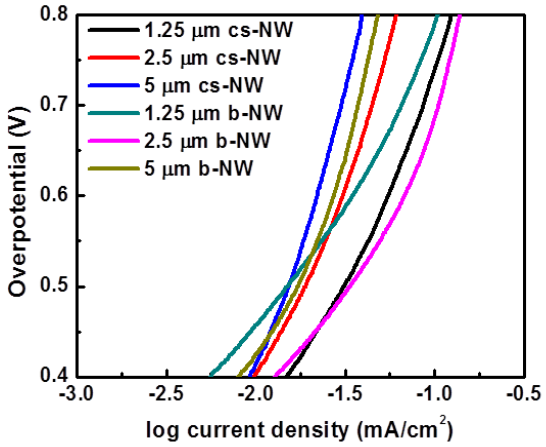

Figure 3.11 Comparison of Tafel plot of TiO_2/Si cs-NW and b-NW array based photoelectrodes with different Si NW lengths.

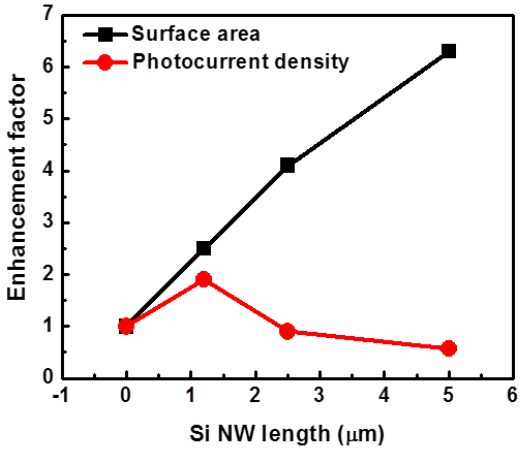

Figure 3.12 Effect of Si NW length on surface area and photocurrent density.

3.3.5 Photocurrent spectrum responses of the TiO_2/Si b-NW arrays

Figure 3.13 shows the IPCE data of the TiO_2/Si b-NWs array photoelectrode with ~2.5 μm Si NWs under 2 V bias. A large photoresponse with close to 50% IPCE in the UV region was observed, which indicates that one electron is generated by two UV photons absorbed by both Si and TiO_2 after recombination at interface, performing a redox reaction with water molecules. On the other hand, under visible light illumination, the IPCE value is less than 1% (see Figure 3.13 inset), meaning that the photogenerated carriers only in Si NWs do not contribute to photocurrent. This can be easily understood from the band diagram that the photogenerated holes in Si are blocked by the energy barrier and there is no carrier generation in wide band gap TiO_2. The small photocurrent can be from the high-energy holes from Si that tunneled through the barrier or from the photogenerated carriers in TiO_2 due to defect absorption. To prove this charge transfer mechanism at the TiO_2/Si heterojunction, the photochemical activity was further

investigated by applying a 550 nm long wavelength pass filter to the solar simulator in Figure 3.14. The 550 nm filter only allowed light with a wavelength ranging from 560 nm to 1100 nm to pass while the light with wavelength below 550 nm ± 5nm was cut off. The light in this experiment was only absorbed by the Si NWs present underneath. Figure 3.14 shows the photocurrent density versus the bias potential characteristics of TiO_2/Si b-NW array with ~2.5 μm long Si backbone (the best sample) under dark, full solar illumination, and filtered illumination. However, when the 550 nm filter was applied, the photocurrent density was significantly reduced to ~3 $\mu A/cm^2$ at 2 V vs. RHE, which is four times higher than that under dark but three orders of magnitudes lower than that under unfiltered illumination (see Figure 3.14 inset). Note that the light intensity of solar spectrum in the wavelength over 560 nm was very slightly changed by the 550 nm filter in Figure 3.15. Therefore, the appreciable photocurrent reduction with the 550 nm filter confirmed that TiO_2 and Si can be independently excited by photons in the solar spectrum having different energies and two-photon-one-electron process (photocurrent) develops only when TiO_2 and Si are excited in a synergistic manner. Therefore, the PEC performance of this TiO_2/Si b-NW structure can be improved by optimizing the dimensions and densities of both the Si and TiO_2 NWs or by doping TiO_2 with foreign elements to improve the TiO_2 properties.

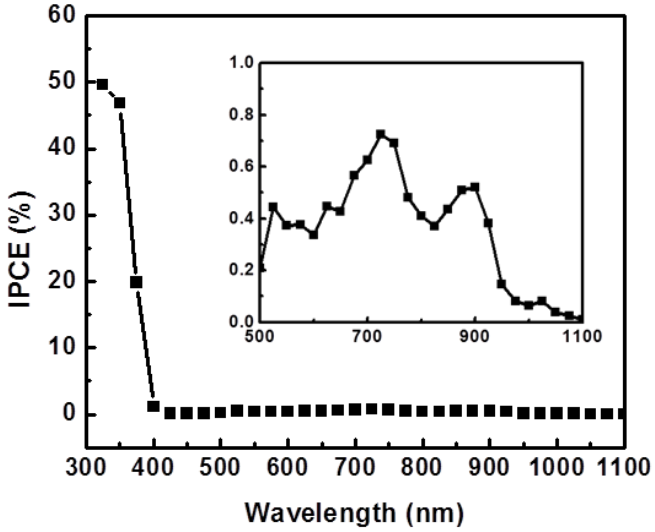

Figure 3.13 IPCE of TiO_2/Si b-NW array photoelectrode (with ~2.5 μm Si NW backbones) measured at an applied bias of 2 V. Inset indicates the zoom in IPCE data in the wavelength range of 500~1100 nm.

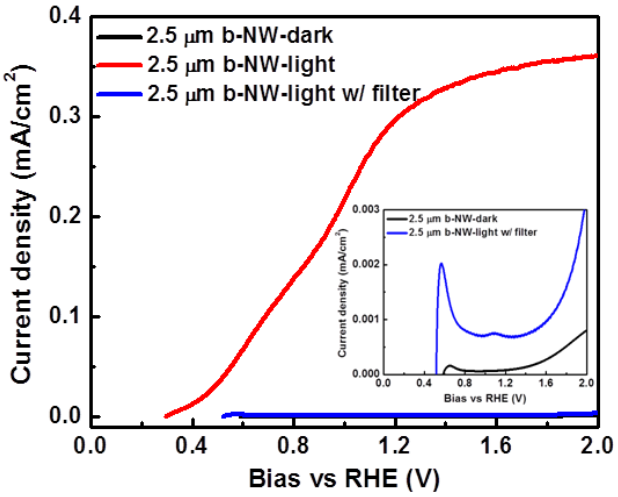

Figure 3.14 PEC performance of ~2.5 μm long TiO_2/Si b-NW array based photoelectrode under dark, full solar illumination, and filtered illumination with a 550 nm long wavelength pass filter. Inset indicates the zoom in PEC performance under dark and the filtered illumination.

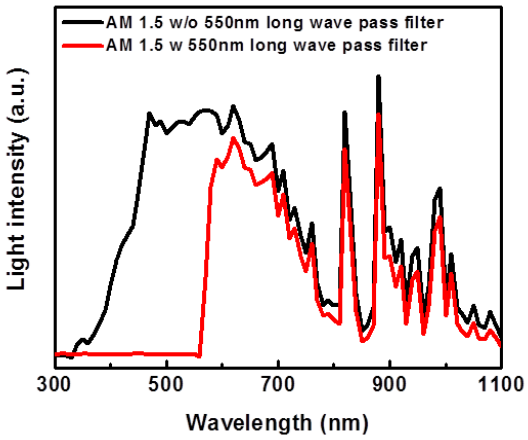

Figure 3.15 Comparison of light intensity of solar simulator (AM 1.5, 100 mW/cm^2) and when a 550 nm long wave pass filter was applied.

3.4 Conclusion

In summary, we reported a successful fabrication of novel, 3D branched TiO_2/Si NW arrays and their photoelectrochemical performance as a photoanode. The hierarchical structured photoelectrodes with various Si NW lengths were fabricated by a combination of nanoimprint lithography, reactive ion etch, and hydrothermal reactions. The TiO_2/Si b-NWs arrays noticeably improved the PEC performance compared to TiO_2 thin film-coated Si NW (cs-NW) arrays. IPCE value of about 50% is obtained under UV illumination indicating an operation of a two-photon-one-electron process model. The PEC performance of this b-NW photoelectrodes can be further improved by optimizing the dimensions and densities of both the Si and TiO_2 NWs. These studies of hierarchically integrated nanostructures and the associated understanding of charge transfer at heterojunction interface can lead to improved nanoscale devices for renewable energy applications.

3.5 Note

This chapter, in full, is a reprint of the material as it appears in Nano Energy, Volume 2, 2013. Sun Young Noh, Ke Sun, Chulmin Choi, Mutong Niu, Ke Xu, Muchuan Yang, Sungho Jin, and Deli Wang. The dissertation author was the primary investigator and author of this paper.

3.6 References

1. Fujishima, A. & Honda, K. Electrochemical Photolysis of Water at a Semiconductor Electrode. *Nature* **238**, 37-38 (1972).

2. Rocheleau, R.E. & Miller, E.L. Photoelectrochemical production of hydrogen: Engineering loss analysis. *International Journal of Hydrogen Energy* **22**, 771-782 (1997).

3. Peng, K., Xu, Y., Wu, Y., Yan, Y., Lee, S.T., and Zhu, J. Aligned Single-Crystalline Si Nanowire Arrays for Photovoltaic Applications. *Small* **1**, 1062-1067 (2005).

4. Amouyal, E. Photochemical production of hydrogen and oxygen from water: A review and state of the art. *Solar Energy Materials and Solar Cells* **38**, 249-276 (1995).

5. Bak, T., Nowotny, J., Rekas, M. & Sorrell, C.C. Photo-electrochemical hydrogen generation from water using solar energy. Materials-related aspects. *International Journal of Hydrogen Energy* **27**, 991-1022 (2002).

6. Yang, X., Wolcott, A., Wang, G., Sobo, A., Fitzmorris, R.C, Qian, F., Zhang, J.Z., and Li, Y., Nitrogen-Doped ZnO Nanowire Arrays for Photoelectrochemical Water Splitting. *Nano Letters* **9**, 2331-2336 (2009).

7. Chen, X. & Burda, C. The Electronic Origin of the Visible-Light Absorption Properties of C-, N- and S-Doped TiO2 Nanomaterials. *Journal of the American Chemical Society* **130**, 5018-5019 (2008).

8. Allam, N.K. & El-Sayed, M.A. Photoelectrochemical Water Oxidation Characteristics of Anodically Fabricated TiO2 Nanotube Arrays: Structural and Optical Properties. *The Journal of Physical Chemistry C* **114**, 12024-12029 (2010).

9. Cesar, I., Kay, A., Gonzalez Martinez, J.A. & Grätzel, M. Translucent Thin Film Fe2O3 Photoanodes for Efficient Water Splitting by Sunlight: Nanostructure-Directing Effect of Si-Doping. *Journal of the American Chemical Society* **128**, 4582-4583 (2006).

10. Su, J., Guo, L., Bao, N. & Grimes, C.A. Nanostructured WO3/BiVO4 Heterojunction Films for Efficient Photoelectrochemical Water Splitting. *Nano Letters* **11**, 1928-1933 (2011).

11. Mohapatra, S.K., John, S.E., Banerjee, S. & Misra, M. Water Photooxidation by Smooth and Ultrathin α-Fe2O3 Nanotube Arrays. *Chemistry of Materials* **21**, 3048-3055 (2009).

12. Hoang, S., Guo, S., Hahn, N.T., Bard, A.J. & Mullins, C.B. Visible Light Driven Photoelectrochemical Water Oxidation on Nitrogen-Modified TiO2 Nanowires. *Nano Letters* (2011).

13. Wang, G., Yang, X., Qian, F., Zhang, J.Z. & Li, Y. Double-Sided CdS and CdSe Quantum Dot Co-Sensitized ZnO Nanowire Arrays for Photoelectrochemical Hydrogen Generation. *Nano Letters* **10**, 1088-1092 (2010).

14. Jang, J.S., Kim, H.G. & Lee, J.S. Heterojunction semiconductors: A strategy to develop efficient photocatalytic materials for visible light water splitting. *Catalysis Today* **185**, 270-277 (2012).

15. Ni, M., Leung, M.K.H., Leung, D.Y.C. & Sumathy, K. A review and recent developments in photocatalytic water-splitting using for hydrogen production. *Renewable and Sustainable Energy Reviews* **11**, 401-425 (2007).

16. Yin, W.J., Tang, H., Wei, S.H., Al-Jassim, M.M., Turner, J., and Yan, Y., Band structure engineering of semiconductors for enhanced photoelectrochemical water splitting: The case of TiO_{2}. *Physical Review B* **82**, 045106 (2010).

17. Kronawitter, C.X., Vayssieres, L., Shen, S., Guo, L., Wheeler, D.A., Zhang,Z.J., Antounf, B.R., and Mao, S.S., A perspective on solar-driven water splitting with all-oxide hetero-nanostructures. *Energy & Environmental Science* **4**, 3889-3899 (2011).

18. Seabold, J.A., Shankar, K., Wilke, R.H.T., Paulose, M., Varghese, O.K., Grimes, C.A., and Choi, K.S., Photoelectrochemical Properties of Heterojunction CdTe/TiO2 Electrodes Constructed Using Highly Ordered TiO2 Nanotube Arrays. *Chemistry of Materials* **20**, 5266-5273 (2008).

19. Sivula, K., Formal, F.L. & Grätzel, M. WO3−Fe2O3 Photoanodes for Water Splitting: A Host Scaffold, Guest Absorber Approach. *Chemistry of Materials* **21**, 2862-2867 (2009).

20. Lin, Y., Zhou, S., Liu, X., Sheehan, S. & Wang, D. TiO2/TiSi2 Heterostructures for High-Efficiency Photoelectrochemical H2O Splitting. *Journal of the American Chemical Society* **131**, 2772-2773 (2009).

21. Hong, S.J., Lee, S., Jang, J.S. & Lee, J.S. Heterojunction BiVO4/WO3 electrodes for enhanced photoactivity of water oxidation. *Energy & Environmental Science* **4**, 1781-1787 (2011).

22. Zhu, W., Liu, A., Liu, H., Tong, D., Yang, J., and Peng J., Coaxial Heterogeneous Structure of TiO2 Nanotube Arrays with CdS as a Superthin Coating Synthesized via Modified Electrochemical Atomic Layer Deposition. *Journal of the American Chemical Society* **132**, 12619-12626 (2010).

23. Sun, K., Jing, Y., Li, C., Zhang, Z., Aguinaldo, R., Kargar, A., Madsen, K., Banu, K., Zhou, Y., Bando, Y., Liua Z., and Wang, D., 3D branched nanowire heterojunction photoelectrodes for high-efficiency solar water splitting and H2 generation. *Nanoscale* **4**, 1515-1521 (2012).

24. Peng, K., Wang, X. & Lee, S.-T. Silicon nanowire array photoelectrochemical solar cells. *Applied Physics Letters* **92**, 163103-163103 (2008).

25. Garnett, E. & Yang, P. Light Trapping in Silicon Nanowire Solar Cells. *Nano Letters* **10**, 1082-1087 (2010).

26. Leempoel, P., Castro-Acuna, M., Fan, F.-R.F. & Bard, A.J. Semiconductor electrodes. 43. The effect of light intensity and iodine doping on the stabilization of n-silicon by phthalocyanine films. *The Journal of Physical Chemistry* **86**, 1396-1400 (1982).

27. Imanishi, A., Okamura, T., Ohashi, N., Nakamura, R. & Nakato, Y. Mechanism of Water Photooxidation Reaction at Atomically Flat TiO2 (Rutile) (110) and (100) Surfaces: Dependence on Solution pH. *Journal of the American Chemical Society* **129**, 11569-11578 (2007).

28. Wang, G., Wang, H., Ling, Y., Tang, Y., Yang, Z., Fitzmorris, R.C., Wang, C., Zhang, J.Z., and Li, Y., Hydrogen-Treated TiO2 Nanowire Arrays for Photoelectrochemical Water Splitting. *Nano Letters* **11**, 3026-3033 (2011).

29. Hung, Y.-J., Lee, S.-L. & Coldren, L.A. Deep and tapered silicon photonic crystals for achieving anti-reflection and enhanced absorption. *Optics Express* **18**, 6841 (2010).

30. Fan, Z., Ruebusch, D.J., Rathore, A.A., Kapadia, R., Ergen, O., Leu, P.W., Javey, A., Challenges and prospects of nanopillar-based solar cells. *Nano Research* **2**, 829-843 (2009).

31. Lin, C. & Povinelli, M.L. Optical absorption enhancement in silicon nanowire arrays with a large lattice constant for photovoltaic applications. *Opt. Express* **17**, 19371-19381 (2009).

32. Garnett, E.C., Brongersma, M.L., Cui, Y. & McGehee, M.D. Nanowire Solar Cells. *Annual Review of Materials Research* **41**, 269-295 (2011).

33. Shi, J., Hara, Y., Sun, C., Anderson, M.A. & Wang, X. Three-Dimensional High-Density Hierarchical Nanowire Architecture for High-Performance Photoelectrochemical Electrodes. *Nano Letters*, 3413-3419 (2011).

34. Cheng, C. & Fan, H.J. Branched nanowires: Synthesis and energy applications. *Nano Today* **7**, 327-343 (2012).

35. Morton, K.J., Nieberg, G., Bai, S. & Chou, S.Y. Wafer-scale patterning of sub-40 nm diameter and high aspect ratio (>50:1) silicon pillar arrays by nanoimprint and etching. *Nanotechnology* **19**, 345301 (2008).

36. Fu, Y.Q. Colli, A., Fasoli, A., Luo, J. K., Flewitt, A. J., Ferrari, A. C., and Milne, W. I., Deep reactive ion etching as a tool for nanostructure fabrication. *Journal of Vacuum Science & Technology B Microelectronics and Nanometer Structures* **27**, 1520 (2009).

37. Wu, B., Kumar, A. & Pamarthy, S. High aspect ratio silicon etch: A review. *Journal of Applied Physics* **108**, 051101 (2010).

38. Kumar, A., Madaria, A.R. & Zhou, C. Growth of Aligned Single-Crystalline Rutile TiO2 Nanowires on Arbitrary Substrates and Their Application in Dye-Sensitized Solar Cells. *The Journal of Physical Chemistry C* **114**, 7787-7792 (2010).

39. Sun, K., Park, N., Sun, Z., Zhou, J., Wang, J., Pang, X., Shen, S., Noh, S.Y., Jing, Y., Jin, S., Yua, P.K.L., and Wang, D., Nickel oxide functionalized silicon for efficient photo-oxidation of water. *Energy & Environmental Science* (2012).

40. Lévy-Clément, C., Lagoubi, A., Neumann-Spallart, M., Rodot, M. & Tenne, R. Efficiency and Stability Enhancement of n-Si Photoelectrodes in Aqueous Solution. *Journal of The Electrochemical Society* **138**, L69-L71 (1991).

41. Kohl, P.A., Frank, S.N. & Bard, A.J. Semiconductor Electrodes. *Journal of The Electrochemical Society* **124**, 225-229 (1977).

42. Tang, D., Cheng, K., Weng, W., Song, C., Du, P., Shen, G., and Han, G., TiO2 nanorod films grown on Si wafers by a nanodot-assisted hydrothermal growth. *Thin Solid Films* **519**, 7644-7649 (2011).

43. Wang, H.E., Chen, Z., Leung, Y. H., Luan, C., Liu, C., Tang, Y., Yan, C., Zhang, W., Zapien, J.A., Bello, I. and Lee, S. T., Hydrothermal synthesis of ordered single-crystalline rutile TiO[sub 2] nanorod arrays on different substrates. *Applied Physics Letters* **96**, 263104-263103 (2010).

44. Ji, L., Kim, J. K., Ji, Q., Leung, K. N., Chen, Y., and Gough, R. A., Conformal metal thin-film coatings in high-aspect-ratio trenches using a self-sputtered rf-driven plasma source. *Journal of Vacuum Science & Technology B: Microelectronics and Nanometer Structures* **25**, 1227-1230 (2007).

45. Liu, B. & Aydil, E.S. Growth of Oriented Single-Crystalline Rutile TiO2 Nanorods on Transparent Conducting Substrates for Dye-Sensitized Solar Cells. *Journal of the American Chemical Society* **131**, 3985-3990 (2009).

46. Chen, F., Zhou, R., Yang, L., Shi, M., Wu, G., Wang, M., and Chen, H., One-Step Fabrication of CdS Nanorod Arrays via Solution Chemistry. *The Journal of Physical Chemistry C* **112**, 13457-13462 (2008).

47. Xu, S., Shen, Y., Ding, Y. & Wang, Z.L. Growth and Transfer of Monolithic Horizontal ZnO Nanowire Superstructures onto Flexible Substrates. *Advanced Functional Materials* **20**, 1493-1497 (2010).

48. Mahajan, V.K., Misra, M., Raja, K.S. & Mohapatra, S.K. Self-organized TiO 2 nanotubular arrays for photoelectrochemical hydrogen generation: effect of crystallization and defect structures. *Journal of Physics D: Applied Physics* **41**, 125307 (2008).

49. Cho, I.S., Chen, Z., Forman, A.J., Kim, D.R., Rao, P.M., Jaramillo, T.F., and Zheng, X., Branched TiO2 Nanorods for Photoelectrochemical Hydrogen Production. *Nano Letters* **11**, 4978-4984 (2011).

50. Wang, B. & Leu, P.W. Enhanced absorption in silicon nanocone arrays for photovoltaics. *Nanotechnology* **23**, 194003 (2012).

51. Wong, S.M., Yu, H.Y., Li, J.S., Zhang, G., Lo, P., and Kwong, D. L., Design High-Efficiency Si Nanopillar-Array-Textured Thin-Film Solar Cell. *Electron Device Letters, IEEE* **31**, 335-337 (2010).

52. Hwang, Y.J., Boukai, A. & Yang, P. High Density n-Si/n-TiO2 Core/Shell Nanowire Arrays with Enhanced Photoactivity. *Nano Letters* **9**, 410-415 (2008).

53. Mayer, M.T., Du, C. & Wang, D. Hematite/Si Nanowire Dual-Absorber System for Photoelectrochemical Water Splitting at Low Applied Potentials. *Journal of the American Chemical Society* **134**, 12406-12409 (2012).

54. Yuan, G., Aruda, K., Zhou, S., Levine, A., Xie, J., and Wang, D., Understanding the Origin of the Low Performance of Chemically Grown Silicon Nanowires for Solar Energy Conversion. *Angewandte Chemie International Edition* **50**, 2334-2338 (2011).

3.7. Appendix

Nano Energy Cover page image

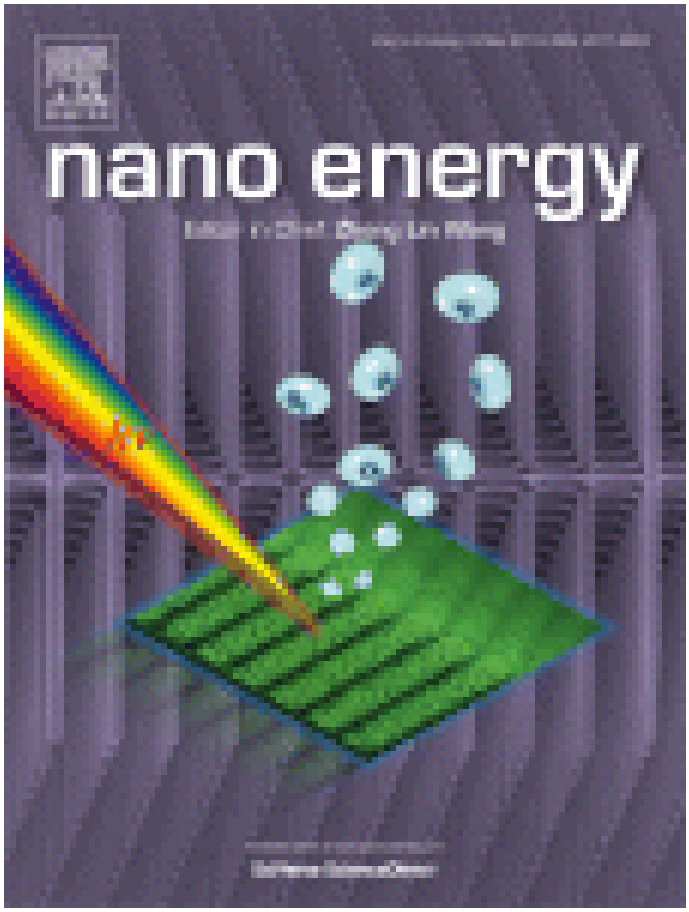

CHAPTER 4: Metal-enabled Efficient Photoelectrochemical Photoanodes for Solar Water Oxidation

4.1 Introduction

Since the usage of fossil fuels not only causes environmental problems such as climate change and but also has cost issues from their limited amount, numerous researches in the field of renewable energy have been vigorously performed to develop alternative energy resources[1]. Photoelectrochemical (PEC) water splitting process of semiconducting materials is one of the most attractive approaches, which efficiently converts solar energy with water to storable and transportable hydrogen fuel, because of its potential high efficiency, up to >30 % in principle, low cost, and environmental friendliness[2, 3].

Although it is an attractive photovoltaic material for efficient solar energy harvesting due to a narrow band gap (~1.1 eV), Si is not an appropriate photoelectrode material for PEC cells because it is easily oxidized/decomposed in the electrolyte due to its unfavourable band edge positions and poor photochemical stability and it also needs a huge overpotential for water splitting owing to its poor kinetics[4, 5]. To solve these issues and develop efficient Si based photoelectrodes, Si has been combined with other materials. Stable photocatalyst materials such as ZnO and TiO_2 were coated or grown on the Si surface mainly to improve light absorption as well as protect photochemical corrosion[6-9]. Also, electrocatalyst materials such as NiO_x, Pt, and Ir were integrated with Si to reduce overpotential because the electrocatlyst can increase charge separation and

reduce charge recombination by accelerating the water oxidation/reduction kinetics[5, 10, 11]. Besides, when a stable metal layer is employed as the electrocatalyst, we can further use junction effects not only to provide a potential for water electrolysis of the electocatalyst but also to protect Si surface. A metal-silicon (MS) structure offers Schottky junction at the interface which causes to increase band bending then further reduce charge recombination[12]. In addition, a metal-insulator-silicon (MIS) structure can be fabricated by adding a sufficiently thin insulating layer in which the minority charge carriers can flow by quantum mechanical tunneling whereas the majority carriers are blocked[13]. Thus, efficient charge separation and transfer occur in the MIS structure leading to less overpotential required for water splitting[14, 15]. In MIS structures, however, the insulating layer must be very thin (less than 2 nm) and uniform layer with high quality so that tunneling currents are large enough for applications[16, 17]. Note that in both MS and MIS structures, the thickness of a metal electrocatlyst layer should be a compromise between transparency and voltage drop caused by series resistance.

In this study, to develop cost-effective and efficient Si-based photoelectrodes, we chose Ni layer as a metal electrocatalyst due to its earth abundance and good catalyst properties. With Ni electrocatalyst, we fabricated both MS and MIS structures to investigate the effects of structure/interfacial junction type on PEC performance parameters. Also, two different insulating layers such as native silicon oxide layer or artificial silicon oxide layer were used for MIS structures and we compared their properties in PEC water splitting cells. Moreover, we examined the metal thickness effects of the Ni electrocatalyst for the absorbed light amount of Si as well as electrocatalytic reactions.

4.2 Experiments

4.2.1 Fabrication MS and MIS photoanodes

Phosphorus doped n-type silicon wafers (University Wafer, single side polished, 0.3~0.5 Ω-cm reesistivity) were cut into sample size (half inch × half inch) and were cleaned by 10% nitric acid solution, acetone, isopropanol alcohol, deionized water, and then blow-dried by nitrogen gas. Ni metal layers with different thickness x (x: 2, 5, 10, and 20 nm) were directly deposited on the cleaned Si samples by e-beam evaporation method (Temescal BJD 1800 Ebeam Evaporator). These were designated by MIS-native structures (or x nm/native SiO_2/Si), which have native oxide layer. On the other hand, for other sample structures, the native oxide layer was intentionally removed by immersing in buffered HF etchant (BOE) then rinsing with deionized water before Ni deposition. MS structures (or x nm/Si) were prepared by coating Ni layers on the oxide-removed Si samples by the same way as above, whereas MIS-HWO structures (or x nm/HWO SiO_2/Si) were fabricated by hot water oxidation (HWO) (80 °C for 1 min) of the oxide-removed Si samples following Ni deposition. The energy-dispersive X-ray spectroscopy (EDS) and its elemental mapping analyses confirmed that Ni layer was deposited uniformly on the Si surface (Figure 4.1). Also, the absorption properties of MS and MIS were simulated by the transfer matrix method (TMM). The refractive indices of nickel and silicon are taken from the experimental data reported in a book[18] and the refractive index of silicon dioxide is set to be 1.5. As shown in figure 4.2, the illumination is a normally incident plane wave. There are no differences of absorption values between MS and MIS photoanodes which have identical thickness of Ni layer. At 650 nm of

wavelength, the absorption values of photoanodes with no metal, 2nm, 5nm, 10nm and 20nm Ni are 0.65, 0.58, 0.48, 0.35, and 0.19, respectively.

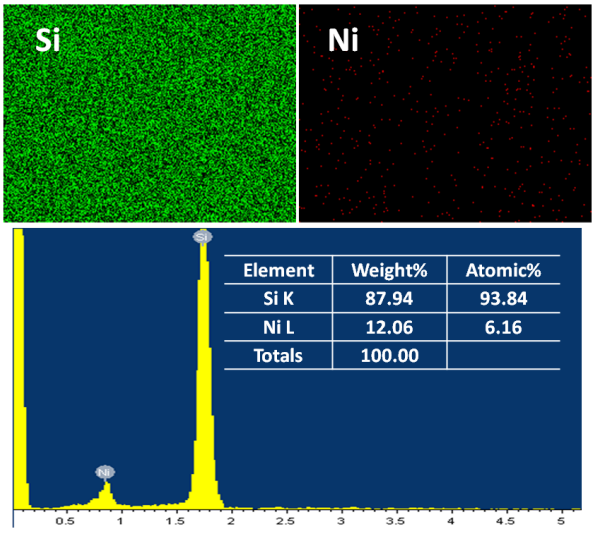

Figure 4.1 EDS mapping image and elements analysis of Ni layer deposited on n-Si substrate.

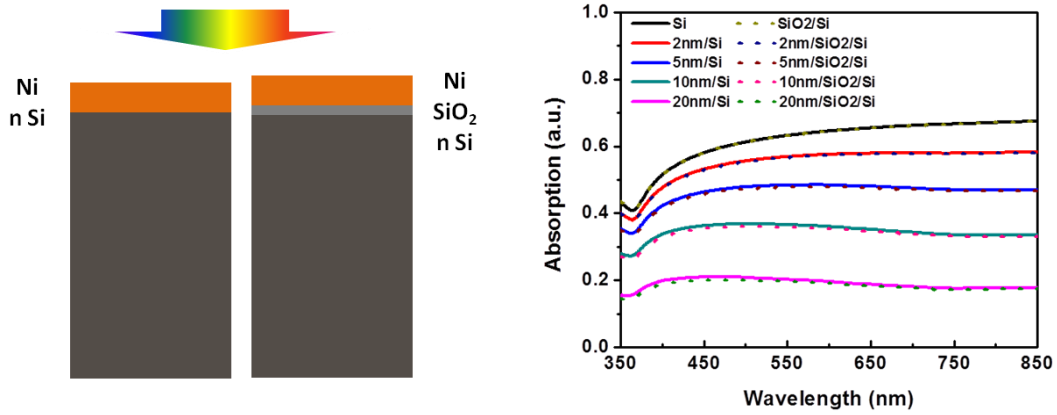

Figure 4.2 Schematic and simulated absorption of MS and MIS samples

4.2.2 PEC performance measurement of MS and MIS photoanodes

PEC performance measurements[5, 8] were carried out in a 1 M KOH electrolyte solution (pH = 14) in a three-electrode configuration, where the MS, MIS-HWO, or MIS-native structured photoanode serves as the working electrode, a platinum coil as the counter electrode, and Hg/HgO electrode (1 M NaOH) as the reference electrode. All three electrodes were in a glass apparatus with a quartz window, through which the photoanodes were illuminated by a solar simulator (Newport) equipped with a 150 W Xe lamp and an AM 1.5 filter (100 mW/cm^2). During the measurement, the electrolyte solution is saturated with nitrogen gas to remove the dissolved oxygen and hydrogen. Steady-state current density-voltage (J–V) measurements were performed using a potentiostat (Digi-ivy Inc., DY2300) with a sweep rate of 10 mV/s and all data were recorded using software DY2300.

4.3 Results and Discussion

4.3.1 PEC water splitting mechanism of MS and MIS structures with Ni reduction reactions

Regardless of the type of structures such as MS or MIS, the surface of Ni layer is electrochemically oxidized to Ni(II) oxide ($Ni(OH)_2$) in high pH solution and the Ni(II) oxide is further transformed to Ni (III) oxide (NiOOH) on the anodic sweep leading to oxygen evolution[19, 20]. These redox reaction peaks of Ni can be clearly seen in figure 4.3 and the peaks were shifted under illumination representing the photovoltage was generated in the structure. Since the reduction of $Ni(OH)_2$ or NiOOH back to metallic Ni cannot occur in the voltage range used here, Ni layer in all samples became a layer

consisting of Ni, NiO_x and $Ni(OH)_2$/NiOOH during JV measurements in electrolyte. The relatively large anodic current of redox reaction peaks of Ni is related to further oxide growth as well as the change in Ni oxidation state from Ni (II) to Ni (III)[20]. It is plausible that very thin Ni layer (<5nm) became to non-metallic NiO_x layer. However, the formation of NiO_x layer does not need to be detrimental to the overall OER process since NiO is known to be conductive and hence will not necessarily impair hole transport from the Si absorber[21].

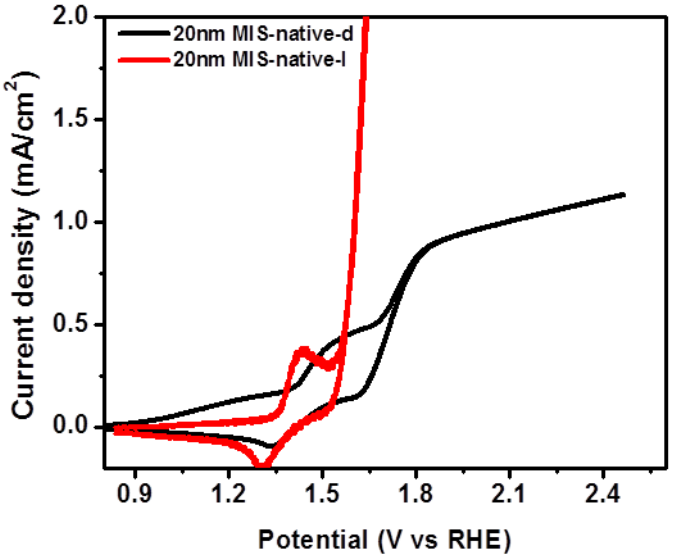

Figure 4.3 Current density of MIS-native with 20nm Ni layer under dark and illumination.

Figure 4.4 shows the band energy diagram of both MS and MIS structures. Under illumination, photogenerated electrons in Si are blocked by a high Schottky barrier at the junction between Si and Ni and flow to the back-contact. Meanwhile, photogenerated holes in Si drift across the junction by the built-in potential in MS or by both the built-in

potential and tunneling in MIS and participate directly in water oxidation reaction at potentials significantly lower than that under dark. Interstitial O and higher state Ni ions (III) exist in Ni layer and they act as acceptors leading to the p-type conductivity as well as oxygen evolution reaction catalytic centers[5].

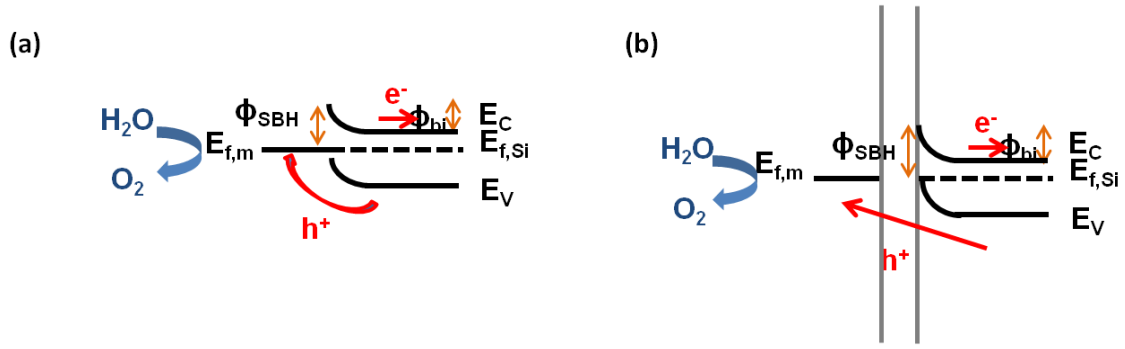

Figure 4.4 Energy band diagrams of both MS (a) and MIS structures (b).

4.3.2 PEC performances of MS and MIS structures

For both MS and MIS structures, the amount of light transmitted on the underlying Si absorber via Ni layer is a key factor to influence the PEC performances, especially current density. The simulation results for absorption properties of MS and MIS samples showed no differences between them (Figure 4.2). Figure 4.5 and 4.6 indicate J-V curves of the MS (a), MIS-HWO (b), and MIS-native (c) structures under dark and illumination, respectively. The important PEC performance parameters such as dark current density (J_{dark}), saturated photocurrent density (J_{sat}), photocurrent on-set potential (V_{os}), and Tafel slope were obtained from the J-V curves and figure 4.7 exhibits the parameters vs Ni thickness for each structure.

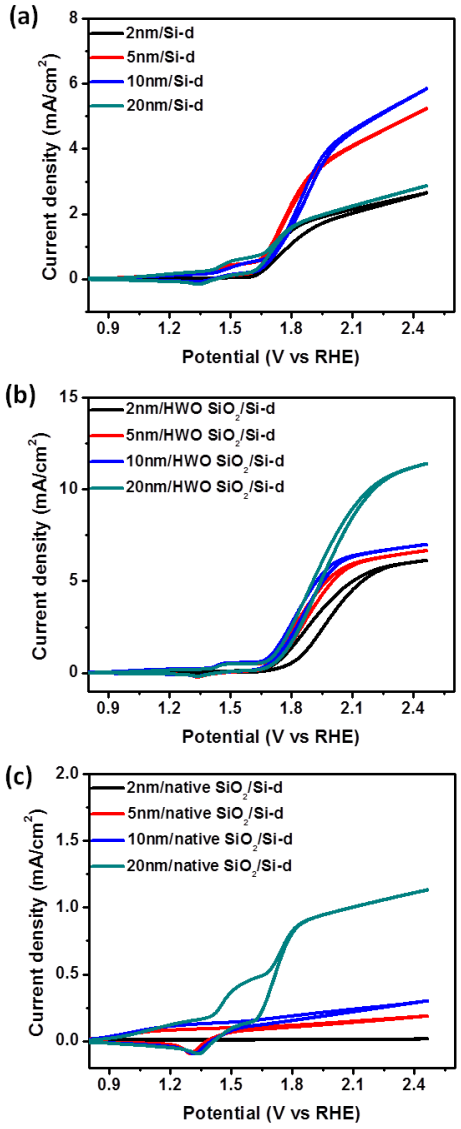

Figure 4.5 J_{dark}-V curves of MS (a), MIS-HWO (b) and MIS-native (c) structures.

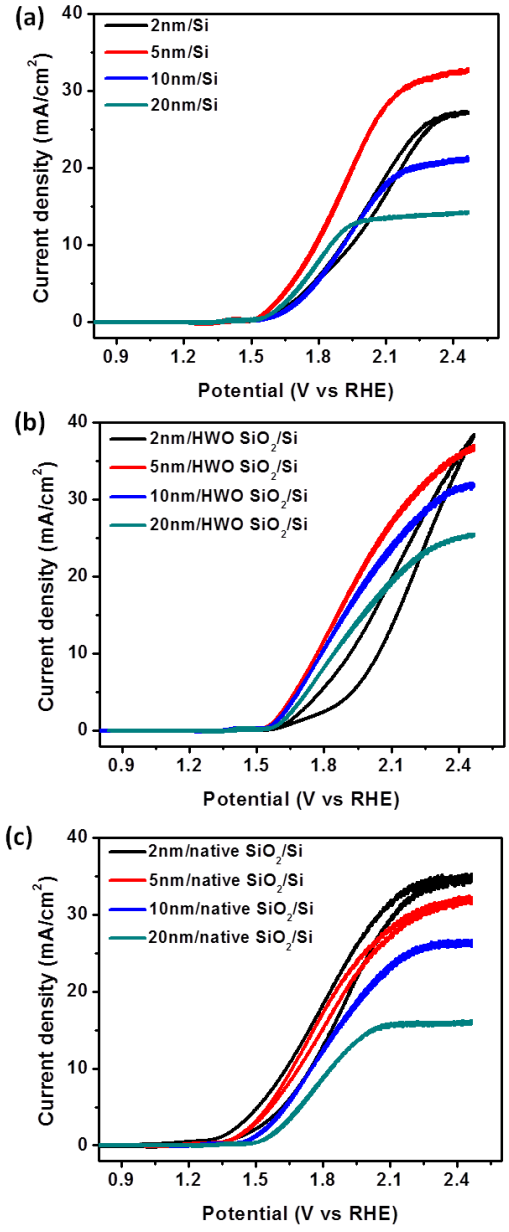

Figure 4.6 J_{photo}-V curves of MS (a), MIS-HWO (b) and MIS-native (c) structures.

4.3.2.1 Dark current density

As shown in figure 4.5 and 4.7 (a), the trends of J_{dark} as a function of Ni thickness are not significantly different among all three structures. In general, J_{dark} increased along with Ni thickness because of intrinsic electrocatalytic activity of Ni and further grown NiO_x layers for oxygen evolution reactions as mentioned above. Even though identical Ni layers were deposited, the values of J_{dark} were totally different depending on the type of structures (Figure 4.7 (a)). Compared to MS structures, MIS-native samples indicate much lower J_{dark} (< 1.2 mA/cm^2 at ~ 2.5 V vs. RHE). It has been reported that in photovoltaic cells, MIS structure has lower J_{dark} than MS structure without decreasing photocurrent density (J_{photo}) because the insulator lowers thermionic emission which influences not J_{photo} but J_{dark}[22]. But even with an insulating layer, MIS-HWO structures show the highest J_{dark} values. J_{dark} can be created by the intrinsic catalytic activity of Ni or produced holes from inherent surface/interface states of Si. Also, in this study, moderately doped n-Si wafers were used for both dark and photo conditions and identical Ni layers were employed in all structures. Therefore, in comparison with that of MIS-native structure, higher peaks for Ni redox reactions as well as higher J_{dark} values of MIS-HWO samples at identical Ni thickness might result from uneven surface or interface states produced during HWO process or too thin oxide layer formed by HWO process.

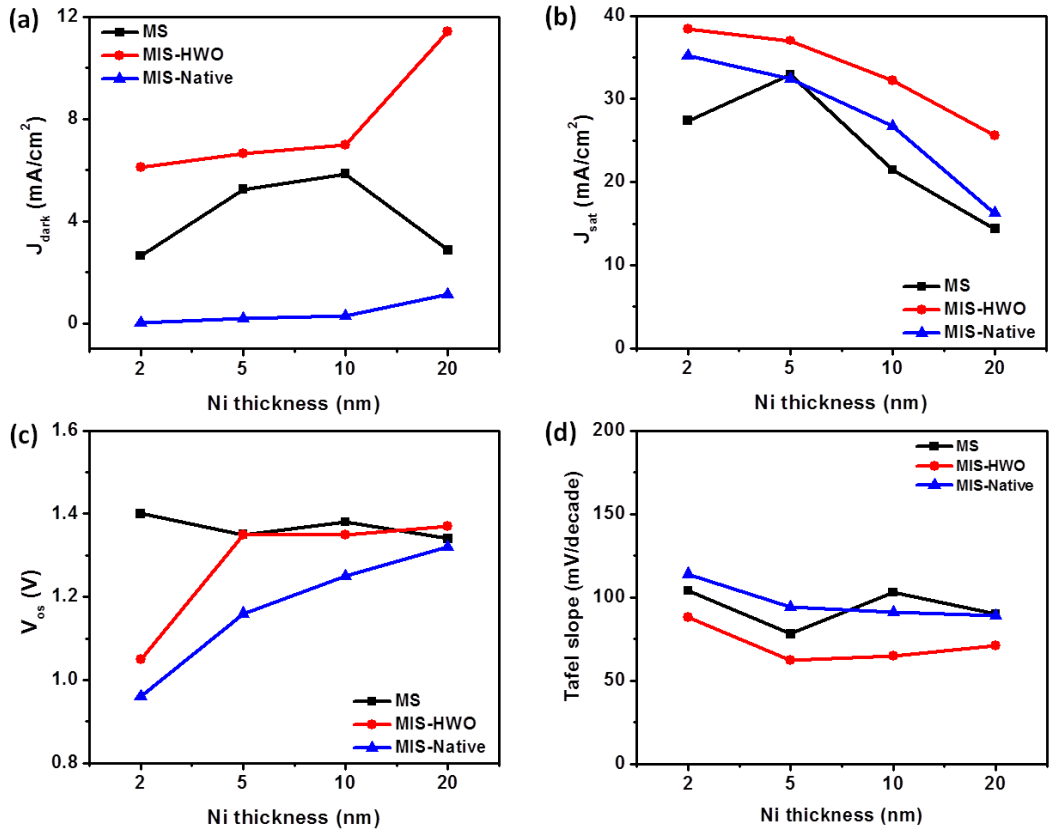

Figure 4.7 PEC performance parameters such as J_{dark} (a), J_{sat} (b), V_{os} (c), and Tafel slope (d) as a function of Ni thickness of MS, MIS-HWO and MIS-native structures.

4.3.2.2 Photocurrent density and photocurrent on-set potential

Figure 4.6 shows J-V curves of MS (a), MIS-HWO (b) and MIS-native (c) structures under illumination. Independently from the structure type, J_{sat} values of the samples decreased as the thickness of Ni layer increased owing to the reduced amount of light transmitted through metal layer onto Si absorber (Figure 4.7 (b)). It should be noted that all samples with 2nm Ni layer have a significant hysteresis between forward and reverse direction scans in J-V curves. In case of MS and MIS-native samples with 2nm layer, in spite of the considerable hysteresis, the J_{photo} values were not significantly

changed during stability test as shown in figure 4.10. Thus, the hysteresis can be explained by charging/discharging of surface/interface trap states, and electrocatalysts[1]. Considering that the samples with thick metal layer (≥ 5 nm) have no hysteresis and their 2nm samples show superior stability, it is possible that 2 nm metal layer is fully oxidized and the hysteresis is a character of ultrathin stable nickel oxide electrocatalyst. On the other hand, MIS-HWO sample with 2 nm Ni layer exhibited that J_{photo} value suddenly dropped in figure 4.10 (a) due to corrosion and surface damage which can be responsible for hysteresis[23]. The inferior stability of the 2 nm MIS-HWO sample might be because very thin Ni layer did not perfectly cover the surface of Si due to inhomogeneous interfacial properties resulted from too thin and uneven HWO layer.

One of the benefit in MIS structure is decoupling of the electrochemical reaction sites (electrocatalyst) from the photovoltaic material (the Si substrate) by the insulating layer[11]. Figure 4.7 (b) shows that compared to MS samples, both MIS-HWO and MIS-native samples have much higher J_{sat} values even with the same amount of light absorption of Si. Provided that all three structures have the same amount of photogenerated carriers at identical Ni thickness, it is understandable that both MIS structures have better charge separation and transfer due to the additional insulating layer. In other words, the insulating layer blocks majority carriers injected into metal layer and thereby suppresses the recombination process leading to better J_{photo} then J_{sat} values[15]. Also, regardless of Ni thickness, MS samples indicated higher V_{os} values in comparison with both MIS structures as shown in Figure 4.7 (c). V_{os}, the photocurrent on-set potential, in this study is defined by the potential value necessary to obtain 0.1 mA/cm^2 of J_{photo}. Thus higher V_{os} values of MS samples at all Ni thickness confirmed that less

built-in potential is formed and more overpotential required to separate photogenerated electrons and holes in MS structures compared to the MIS structures.

Interestingly, MIS-HWO samples indicated much superior J_{sat} values than MIS-native samples at all Ni thickness (Figure 4.7 (b)) implying improved charge transportation with reduced recombination. However, despite higher J_{sat} values, in terms of J_{photo} at low or moderate overpotential as well as V_{os} values, MIS-HWO samples exhibited inferior values than MIS-native ones as shown in figure 4.6 and 4.7 (c). As mentioned earlier, too thin oxide layer could be created during HWO process leading to inhomogeneous interfacial properties which can obstruct charge separation of photogenerated carriers thereby promote back reactions such as their recombination rates. Therefore, MIS-HWO structures required more overpotential to separate photocarriers leading to higher V_{os} values, which are similar to those of MS samples, and lower J_{photo} values at low or moderate overpotential in MIS-HWO structures. However, with huge overpotential, the back reactions of separated carriers were alleviated but the transportation/transfer were accelerated and consequently, MIS-HWO samples indicated larger J_{sat} than that of MIS-native samples at all Ni thickness (Figure 4.5 (b)) implying better charge transportation. As shown in figure 4.7 (d) and 4.9, compared to MIS-native ones, much lower Tafel slope values of MIS-HWO samples stood for the enhanced charge transportation possibly due to better interfacial conductivity in HWO insulating layer.

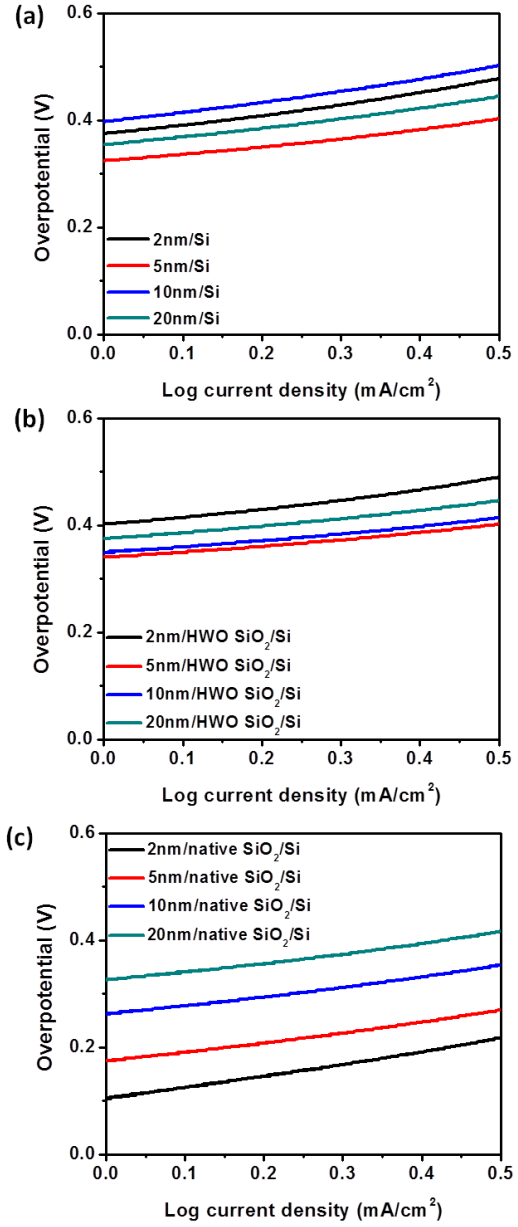

Figure 4.8 Tafel plots of MS (a), MIS-HWO (b) and MIS-native (c) structures.

Independent from the thickness of Ni metal layer, steady V_{os} values as well as Tafel slopes of MS samples (Figure 4.7 (c) and (d)) means a constant recombination rate of separated photo-carriers during charge transportation in Ni layer with different

thickness. This confirmed not only that the oxidized Ni layer is pretty electrically conductive like metal Ni layer but also that Ni thickness doesn't affect built-in potential in MS structures. However, despite the constant recombination rate of separated photo-carriers leading to nearly constant Tafel slopes at all Ni thickness due to conductive metal and metal oxide layer, V_{os} values in case of MIS samples increased in company with the Ni thickness. This confirmed that Ni thickness influences Schottky barrier height in MIS structures probably because the potential drop inside the metal layer can develop over interface states in a Schottky contact leading to metal thickness–dependent screening charges at semiconductor/insulator/metal interfaces[24, 25].

4.3.2.3 Stability and chopped light responses

Figure 4.10 shows J_{sat}-t curves of MS (black), MIS-HWO (red), and MIS-native (blue) structures with Ni layer of 2 nm (a), 5nm (b), 10 nm (c, c'), and 20 nm (d, d') to display the stability properties of them. As stated earlier, the poor stability of the 2nm MIS-HWO sample is probably because of inhomogeneous interfacial properties caused by unevenly formed too thin HWO oxide layer. Except for the unstable 2nm MIS-HWO sample, J values of all samples initially dropped to a certain degree but they became very constant. As expected, regardless of structure types, the samples with thick Ni metal layer had better stability since Si surface or uneven insulating layer were perfectly covered. Compared to those of MIS-native and MS structures, J values of MIS-HWO samples dropped more quickly at the beginning but stabilized J values were the highest among them as shown in figure 4.10. Particularly in case of thick metal layer (≥ 10 nm) (Figure 4.10 (c) and (d)), all samples show less than 1% reduction from 500s to 1800s

demonstrating very stable photoelectrodes. Figure 4.11 shows J-V cures of the best samples in each structure type under chopped light. The best samples such as 5nm MS (a), 5nm MIS-HWO (b) and 2nm MIS-native (c) samples were chosen by considering comprehensive PEC performance parameters, namely photoelectrodes with higher J_{sat}, lower V_{os} and Tafel slope, and superior stability. In all best samples, J values were quickly stabilized under chopped light indicating rapid charge separation of photogenerated carriers particularly at more positive potentials.

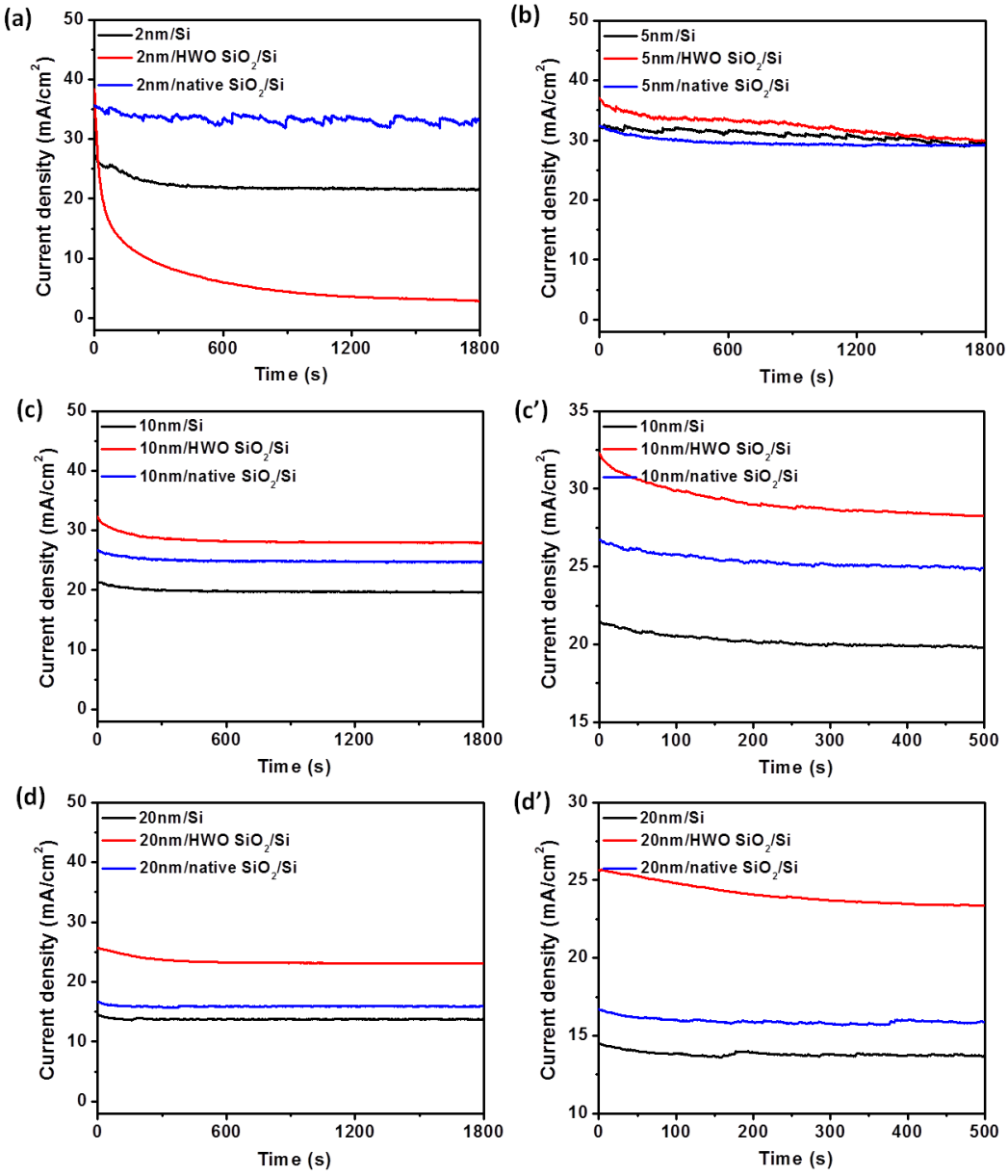

Figure 4.9 J_{sat}-t curves of of MS, MIS-HWO and MIS-native structures with different Ni thickness (2nm (a), 5nm (b), 10nm (c, c'), and 20nm (d, d').

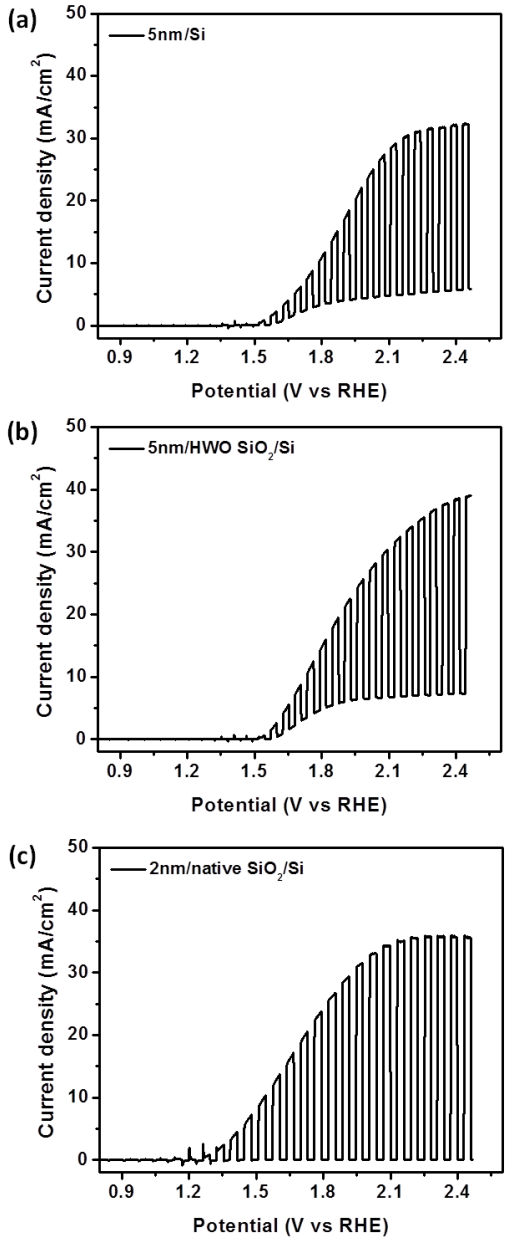

Figure 4.10 J_{photo}-V curves of the best samples in MS (a), MIS-HWO (b) and MIS-native (c) structures.

4.4 Conclusions

We developed cost-effective and efficient Si-based photoelectrodes employing MS and MIS structures with earth abundant and superior Ni electrocatalyst. During PEC performance tests, the oxidized Ni layer was formed but it didn't deteriorate PEC performances due to its excellent conductivity and oxygen evolution catalytic properties. Compared to MS structures, both MIS-native and MIS-HWO structures show much better PEC performances like high photocurrent density, low on-set potential and outstanding stability because the insulator lowers thermionic emission of the extra majority-carrier current path and also it blocked injection of majority carriers into metal layer, suppressed surface recombination by tunneling of electron transfer. Although MIS-native structures exhibit much lower dark current density and exceptional stability, MIS-HWO structures, except 2nm samples, indicate the best performances in terms of saturated current density values after stability test. Therefore, we concluded that HWO insulating layer have better interfacial conductivity/quality than native silicon oxide layer. The performances of MIS samples can be further enhanced by optimizing the quality of insulating layer such as Si_3N_4 and Al_2O_3 or introducing nanoscale metal patterning design.

4.5 Note

This chapter, in full, is currently being prepared for submission for publication of Energy & Environmental Science. Sun Young Noh, Chulmin Choi, Yuanyuan Chen, Sungho Jin, and Deli Wang. The dissertation author was the primary researcher and first author of this paper.

4.6 References

1. Hisatomi, T., Kubota, J. & Domen, K. Recent advances in semiconductors for photocatalytic and photoelectrochemical water splitting. *Chemical Society Reviews* (2014).

2. Walter, M.G., Warren, E.L., McKone, J.R., Boettcher, S.W., Mi, Q. Santori, E.A., and Lewis, N.S., Solar Water Splitting Cells. *Chemical Reviews* **110**, 6446-6473 (2010).

3. Bak, T., Nowotny, J., Rekas, M. & Sorrell, C.C. Photo-electrochemical hydrogen generation from water using solar energy. Materials-related aspects. *International Journal of Hydrogen Energy* **27**, 991-1022 (2002).

4. Lévy-Clément, C., Lagoubi, A., Neumann-Spallart, M., Rodot, M. & Tenne, R. Efficiency and Stability Enhancement of n-Si Photoelectrodes in Aqueous Solution. *Journal of The Electrochemical Society* **138**, L69-L71 (1991).

5. Sun, K., Park, N., Sun, Z., Zhou, J., Wang, J., Pang, X., Shen, S., Noh, S. Y., Jing, Y., Jin, S., Yu, P.K.L., and Wang, D., Nickel oxide functionalized silicon for efficient photo-oxidation of water. *Energy & Environmental Science* **5**, 7872-7877 (2012).

6. Hwang, Y.J., Boukai, A. & Yang, P. High Density n-Si/n-TiO2 Core/Shell Nanowire Arrays with Enhanced Photoactivity. *Nano Letters* **9**, 410-415 (2008).

7. Kargar, A., Sun, K., Jing, Y., Choi, C., Jeong, H., Jung, G.Y., Jin, S., and Wang, D., 3D Branched Nanowire Photoelectrochemical Electrodes for Efficient Solar Water Splitting. *ACS Nano* **7**, 9407-9415 (2013).

8. Noh, S.Y., Sun, K., Choi, C., Niu, M., Yang, M., Xu, K., Jin, S., and Wang, D., Branched TiO2/Si nanostructures for enhanced photoelectrochemical water splitting. *Nano Energy* **2**, 351-360 (2013).

9. Sun, K., Jing, Y., Li, C., Zhang, X., Aguinaldo, R., Kargar, a., Madsen, K., Banu, K., Zhou, Y., Bando, Y., Liua, Z., and Wang, D., 3D branched nanowire heterojunction photoelectrodes for high-efficiency solar water splitting and H2 generation. *Nanoscale* **4**, 1515-1521 (2012).

10. McKone, J.R., Warren, E.L., Bierman, M.J., Boettcher, S.W., Brunschwig, B.S., Lewis, N.S., and Gray, H.B., Evaluation of Pt, Ni, and Ni-Mo electrocatalysts for hydrogen evolution on crystalline Si electrodes. *Energy & Environmental Science* **4**, 3573-3583 (2011).

11. Chen, Y.W., Prange, J.D., Dühnen, S., Park, Y., Gunji, M., Chidsey, C.E.D., and McIntyre, P.C., Atomic layer-deposited tunnel oxide stabilizes silicon photoanodes for water oxidation. *Nat Mater* **10**, 539-544 (2011).

12. Lin, F. & Boettcher, S.W. Adaptive semiconductor/electrocatalyst junctions in water-splitting photoanodes. *Nat Mater* **13**, 81-86 (2014).

13. Hezel, R. Recent progress in MIS solar cells. *Progress in Photovoltaics: Research and Applications* **5**, 109-120 (1997).

14. Scheuermann, A.G., Prange, J.D., Gunji, M., Chidsey, C.E.D. & McIntyre, P.C. Effects of catalyst material and atomic layer deposited TiO2 oxide thickness on the water oxidation performance of metal-insulator-silicon anodes. *Energy & Environmental Science* **6**, 2487-2496 (2013).

15. Esposito, D.V., Levin, I., Moffat, T.P. & Talin, A.A. H2 evolution at Si-based metal–insulator–semiconductor photoelectrodes enhanced by inversion channel charge collection and H spillover. *Nat Mater* **12**, 562-568 (2013).

16. Ghosh, A.K., Fishman, C. & Feng, T. SnO2/Si solar cells—heterostructure or Schottky-barrier or MIS-type device. *Journal of Applied Physics* **49**, 3490-3498 (1978).

17. Wang, C.-Y. & Hwu, J.-G. Metal–Oxide–Semiconductor Structure Solar Cell Prepared by Low-Temperature ($< 400\,^{\circ}\mathrm{C}$) Anodization Technique. *Journal of The Electrochemical Society* **156**, H181-H183 (2009).

18. Palik, E.D. Handbook of Optical Constants of Solids. (Elsevier Science, 1985).

19. Kibria, M.F. & Mridha, M.S. Electrochemical studies of the nickel electrode for the oxygen evolution reaction. *International Journal of Hydrogen Energy* **21**, 179-182 (1996).

20. Medway, S.L., Lucas, C.A., Kowal, A., Nichols, R.J. & Johnson, D. In situ studies of the oxidation of nickel electrodes in alkaline solution. *Journal of Electroanalytical Chemistry* **587**, 172-181 (2006).

21. Cox, C.R., Winkler, M.T., Pijpers, J.J.H., Buonassisi, T. & Nocera, D.G. Interfaces between water splitting catalysts and buried silicon junctions. *Energy & Environmental Science* **6**, 532-538 (2013).

22. Card, H.C. Photovoltaic properties of MIS-Schottky barriers. *Solid-State Electronics* **20**, 971-976 (1977).

23. Sun, K., Madsen, K., Andersen, P., Bao, W.,, Sun, Z., and Wang, D., Metal on metal oxide nanowire Co-catalyzed Si photocathode for solar water splitting. *Nanotechnology* **23**, 194013 (2012).

24. Kenney, M.J., Gong, M., Li, Y. Wu, J.Z., Feng, J., Lanza, M. and Dai, H., High-Performance Silicon Photoanodes Passivated with Ultrathin Nickel Films for Water Oxidation. *Science* **342**, 836-840 (2013).

25. Wu, X. & Yang, E.S. Effective metal screening and Schottky-barrier formation in metal-GaAs structures. *Electron Device Letters, IEEE* **11**, 315-317 (1990).

Chapter 5: Systematic Study of Metal Enabled Si Photocathodes for Efficient Photoelectrochemical Water Reduction

5.1 Introduction

In order to sustainably use sun as a alternative energy, energy storage technologies for a future solar energy infrastructure should be developed although only solar energy can satisfy the current global human energy consumption among various renewable energy resources[1]. Photoelectrochemical (PEC) water splitting process of semiconducting materials can be one of the storage technologies because PEC process efficiently converts solar energy with water to storable and transportable hydrogen fuel[2, 3]. Si with a narrow band gap (~1.1 eV) is an attractive material for efficient solar energy harvesting but it is not an suitable photoelectrode material for PEC cells due to its inappropriate band edge positions and poor photochemical stability as well as its poor kinetics a huge overpotential[4, 5]. To solve these issues and develop efficient Si based photoelectrodes, Si has been integrated with other materials which can produce internal photovoltage for zero bias or low overpotential or improve photochemical stability[5-7].

It has been reported that metal-silicon (MS) structure or metal-insulator-silicon (MIS) in photovoltaic cells offers Schottky junction at the interface which causes to increase band bending then further reduce charge recombination[8]. In addition, MIS structure provides quantum mechanical tunneling process for better transportation rate of minority charge carriers by blocking the majority carriers transfer at the junctions[9]. Thus, efficient charge separation and transfer occur in the MIS structure leading to less

overpotential required for water splitting[7, 10] provided that the MIS structures have less than 2 nm thick and uniform insulating layer with high quality[11, 12]. Note that in both MS and MIS structures, the thickness of a metal electrocatalyst layer should be a compromise between transparency and voltage drop caused by series resistance.

Even though it has exceptional hydrogen evolution catalytic properties particularly in an acidic electrolyte and considerably lowers the overpotential of p-type Si required to evolve H_2, Pt causes low photovoltages owing to a high work function[2, 6, 13]. Also, the high cost of Pt limits the economic viability of PEC water splitting cells. For p-type Si, a low work function metal catalyst produces a rectifying contact to enhance photovoltages[14]. Therefore, for Si-based photoelectrodes, a bimetal layer design can satisfy advanced catalytic and photovoltaic properties by consisting of Pt as an outstanding electrocatalyst for hydrogen evolution and Ti as a Schottky contact metal. Besides, Ti is a cost-effective material and serves as a good adhesion layer for the top Pt layer[10, 13].

Therefore, in order to develop cost-effective and high efficient Si-based photoelectrodes, we chose MS and MIS structures with bimetal layer (Pt/Ti) to investigate the effects of structure/interfacial junction type on PEC performance parameters. Firstly, to choose the best oxide layer for MIS structures, three different insulating layers were compared by PEC performance test. Also, we fabricated MS and MIS samples with three different bimetal layer designs which have various covering or opening for better light absorption of Si and examined the effects of junction types as well as metal pattering types on PEC performance parameters. Moreover, we further

explored the influences of different Pt/Ti thickness ratio in MIS contacts with the three designs.

5.2 Experiments

5.2.1 Fabrication MS and MIS photocathodes with different bimetal designs

Boron doped p-type silicon wafers (University Wafer, single side polished, 0.3~0.5 Ω-cm resistivity) were cut into sample size (half inch × half inch) and were cleaned by 10% nitric acid solution, acetone, isopropanol alcohol, deionized water, and then blow-dried by nitrogen gas. Before metal deposition, we pre-treated Si to prepare MS or MIS structures. Except for MIS-native structure, the native oxide layer in Si was intentionally removed by immersing in buffered HF etchant (BOE) then rinsing with deionized water. The oxide removed Si was directly used for MS structure samples while it was oxidized by hot water oxidation (HWO) (80 °C for 1 min) or rapid thermal oxidation method[10] (950 °C in 8% O_2/N_2, 1,000 °C in a pure N_2, then 10% H_2/N_2) for MIS-HWO samples and MIS-T samples, respectively.

For MS or MIS with planar bimetal layer (or pl), Pt/Ti bimetal layers with different thickness (typical 5nm Pt and 8nm Ti) were directly deposited on the pre-treated Si samples by RF magnetron sputtering (Denton Discovery, 18 Sputter System) at 400 W under 3 mTorr in an argon environment in order of Ti and Pt. Meanwhile, patterned (or pt) and reversed patterned (or rpt) were fabricated by a photolithography process with the pre-treated Si samples using a mask consisting of rectangular opening (450 μm length x 300 μm width) and grid (45 μm row x 15 μm column). Specifically, a photoresist (NR9-3000 for rpt or S1813 for pt) was spin-coated on the pre-treated Si. After baking at 100

^{0}C for 1min, the photolithography was carried out using an UV exposure machine (Karl Suss MA6 Mask Aligner). In case of NR9-3000, post-curing was performed. The UV exposed samples were developed in RD6 for NR9-3000 or MIF-319 for S1813. After RF magnetron sputtering of Pt/Ti bimetal layer, they were subsequently lift-off processed using acetone and rinsed with deionized water. A scanning electron microscope (SEM, Phillips XL30 ESEM), energy-dispersive X-ray spectroscopy (EDS), and its elemental mapping analyses confirmed that Pt/Ti bimetal layer was deposited uniformly on the surface of differently patterned Si samples like pl, pt, and rpt (Figure 5.1 and 5.2). Also, the absorption properties of MS and MIS with different bimetal designs and various Pt/Ti thickness ratios were simulated by the transfer matrix method (TMM). The refractive indices of platinum, titanium and silicon are taken from the experimental data reported in a book and previous paper[15, 16] and the refractive index of silicon dioxide is set to be 1.5. As shown in figure 5.3, there are no differences of Si absorption values with and without $SiO_{2,}$ 0.65 at 650 nm wavelength, indicating that MS and MIS photoanodes have same absorption properties at identical metal design and thickness. As expected, the absorption values of small metal opening samples like pl and pt decreased as total metal thickness increased while large opening samples (rpt) have similar absorption values despite having different metal thickness.

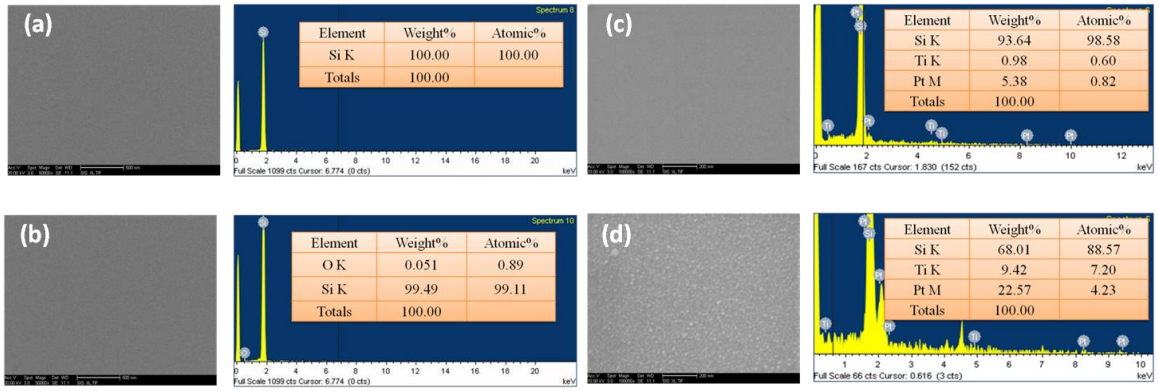

Figure 5.1 SEM images and EDX analysis of BOE treated Si (a), HWO treated Si (b), MS-pl with 5 nm Pt/8nm Ti (c) and 20 nm Pt/30nm Ti (d).

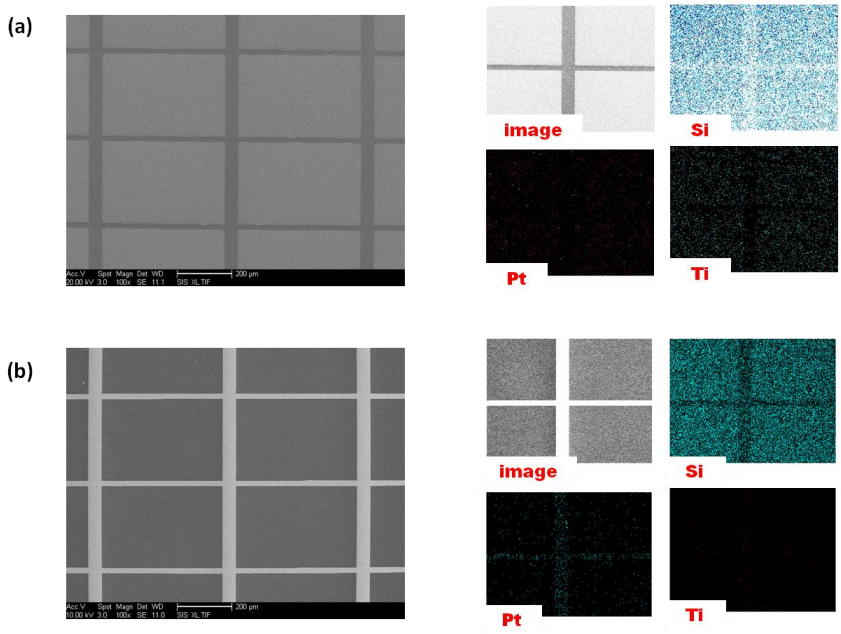

Figure 5.2 SEM images and EDX mappings of pt (a) and rpt (b) metal layer designs

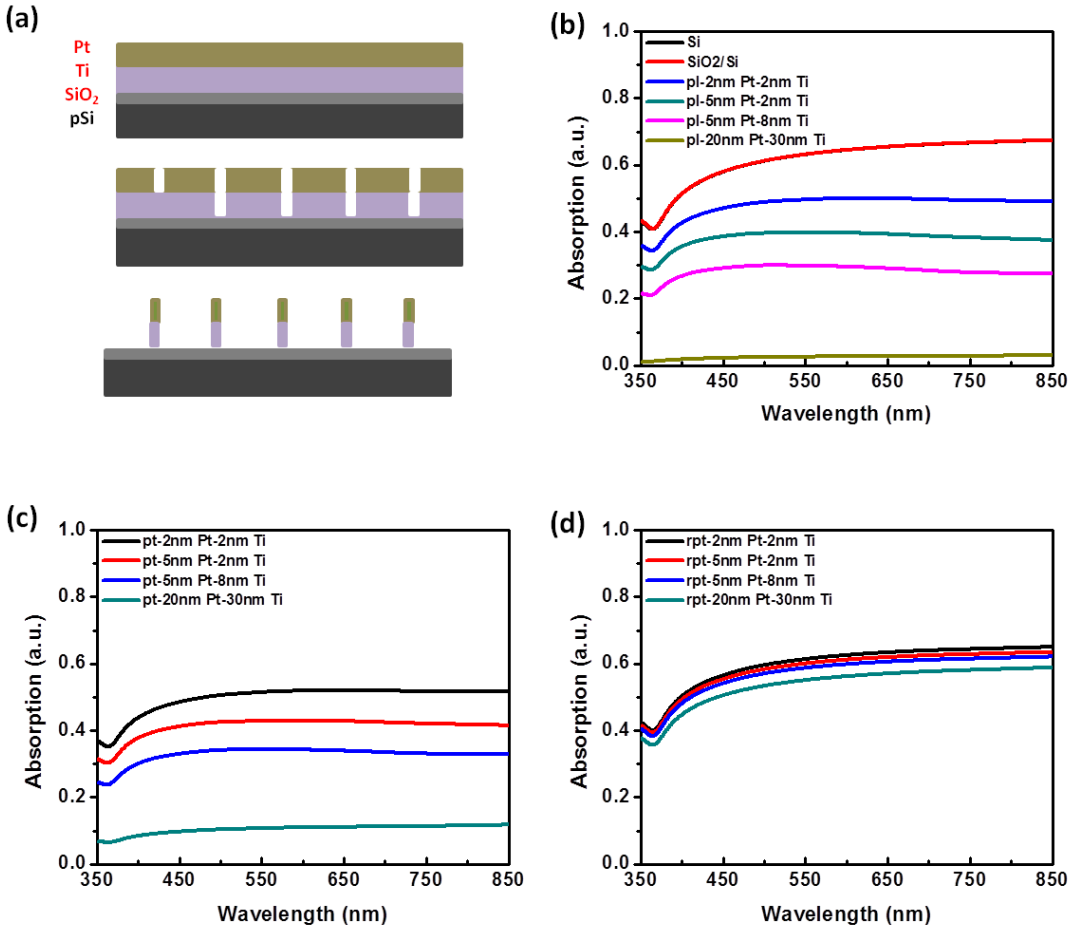

Figure 5.3 Simulated absorption properties of MS and MIS photocathodes with different bimetal designs and various Pt/Ti thickness ratios.

5.2.2 PEC performance measurements of MS and MIS photocathodes with different bimetal designs

PEC performance measurements[5, 17] were carried out in a 0.5 M H_2SO_4 electrolyte solution (pH = 0) in a three-electrode configuration, where the different patterned and structured photoanode serves as the working electrode, a platinum coil as the counter electrode, and Ag/AgCl electrode (1 M NaOH) as the reference electrode. All three electrodes were in a glass apparatus with a quartz window, through which the

photoanodes were illuminated by a solar simulator (Newport) equipped with a 150 W Xe lamp and an AM 1.5 filter (100 mW/cm^2). During the measurement, the electrolyte solution is saturated with nitrogen gas to remove the dissolved oxygen and hydrogen. Steady-state current density-voltage (J–V) measurements were performed using a potentiostat (Digi-ivy Inc., DY2300) with a sweep rate of 10 mV/s and all data were recorded using software DY2300.

5.3 Results and Discussion

5.3.1 MIS structures with different insulating layer and metal layer design

In this study, three different types of metal layer patterning were employed to investigate the light absorption properties of Si as shown in Figure 5.3 (a), including planar bimetal layer (labeled as MS- or MIS-pl) samples without the lithography process, samples with rectangular island shaped bimetal layer (450 μm length x 300 μm width) (labeled MS- or MIS-pt), and samples with grid shaped spacing (45 μm row x 15 μm column) (labeled as MS- or MIS-rpt samples which have the reversed patterning of pt samples).

The thickness and quality of an insulating layer determine the PEC performances, specifically J in MIS structures to efficiently intercede minority carrier transport across the MIS junction with minimal recombination[11, 12]. Particularly, the insulating layer in patterned structures plays another critical role of simultaneous protection to the semiconductor from the corrosive electrolyte. Thus, prior to study on the effects of different metal ratio of Pt/Ti, all different patterned MIS samples with the fixed Pt/Ti thickness (5nm Pt and 8nm Ti) but different oxide layer were prepared. The quality of

each Si oxide layer was evaluated by J-V measurement to compare their effects on PEC performances. Compared to other oxide layer, MIS-HWO samples exhibited the best PEC performances for all patterned structures in terms of $J_{V=0}$ and $J_{V=-0.5}$ demonstrating that the quality of HWO layer is the best (Figure 5.5). Figure 5.4 (a) show J-V curves of MIS-HWO-pl (black), MIS-HWO-pt (red), and MIS-HWO-rpt (blue) samples measured under dark (dot line) and illumination (straight line). J_{dark} values result from intrinsic Pt catalytic properties or interface states at Si/metal junctions. MIS-HWO-pl had the highest J_{dark} values because of the largest amount of Pt electrocatalyst. However, MIS-HWO-pt with only 13.4 % opening showed almost zero dark current even with large amount of Pt electrocatalyst. The carriers which were generated by catalytic reactions of Pt with the electrolyte cannot be collected via Si to back contact by slipping through the opening in the pt design leading to almost zero dark current. Similarly, MIS-HWO-rpt also had nearly zero dark current. As expected, it showed the greatly improved $J_{V=-0.5}$ value because huge opening of 86.6% allows Si to absorb much more light.

Interestingly, regarding the photocurrent on-set potential, V_{os}, which is defined here by the potential at $J_{photo} = 0.1$ mA/cm^2, MIS-HWO-pt has superior values than MIS-HWO-rpt and thereby higher $J_{V=0}$ value. This can be explained by the effect of the metal covered area on the potential drop and band bending at the junction. At the MIS-contacts, the electrons can transfer by tunneling through the oxide film at the conduction band edge or via the occupied interface states. Upon light illumination, an interfacial excess of charge occurs, which induces an increase of the potential drop in the oxide film causing a decrease of the semiconductor band bending. It is probable that the concentration of charged interface states in the metal covered parts of MIS structure is substantially lower

than in the non-covered parts. Therefore, although p-Si has large diffusion lengths for electrons in the range of several hundred μm which develops longer mutual distance of the metal islands[18], bigger portion of the metal covered area in MIS-HWO-pt samples results in smaller efficiency loss with lower charged interface states (Figure 5.4 (b))[19]. Despite whole metal covering, MIS-HWO-pl samples had smaller V_{os} value than the other samples due to large dark current.

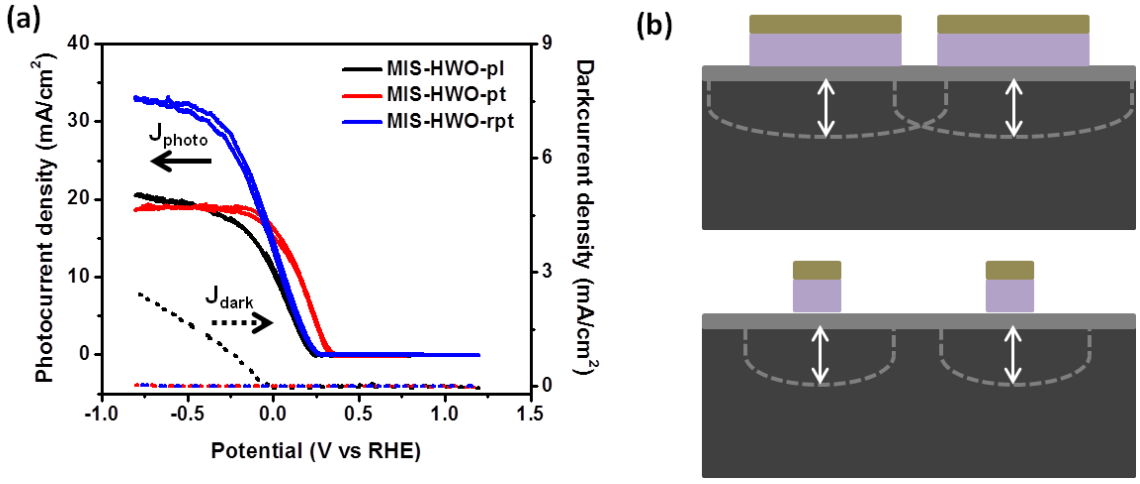

Figure 5.4 J-V curves of MIS-HWO with pl, pt, and rpt metal designs under dark and illuminations (a), and schematic side view of a MIS structures with pt and rpt designs (b).

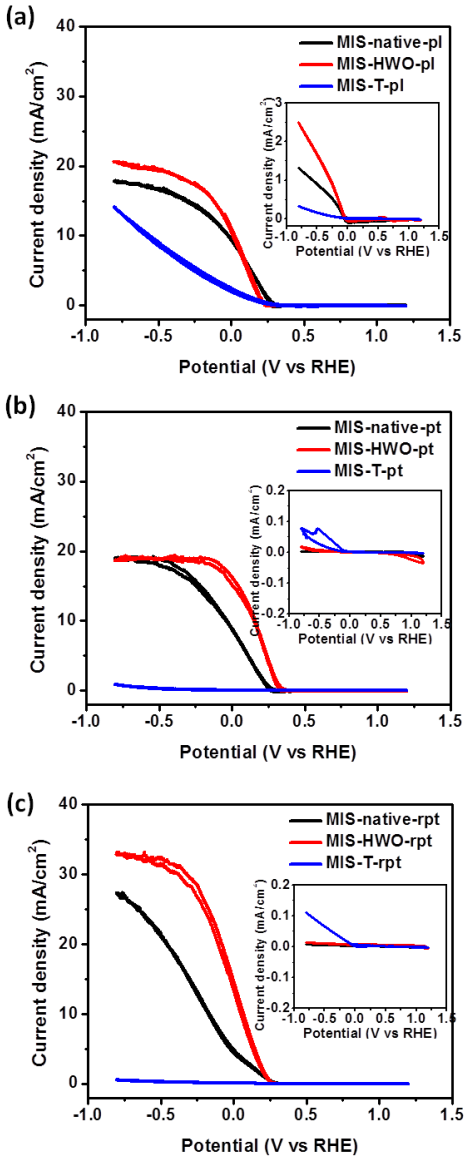

Figure 5.5 J-V curves of MIS structures with different types of insulating layer and metal design under dark (inset) and illumination.

5.3.2 Comparative studies of MS and MIS structures with different metal layer designs

Figure 5.6 shows the comparative study on MS and MIS-HWO samples with differently patterned bimetal layers. We will MIS, instead of MIS-HWO, because all of MIS samples have HWO layer from here. Figure 5.6 (a) and (b) display energy band

diagram of photo-induced reduction processes in MS and MIS contacts, respectively. Under illumination, photogenerated electrons in Si drift across the junction by the built-in potential in MS (figure 5.6 (a)) or by both the built-in potential and tunneling in MIS ((figure 5.6 (b)) to Pt electrocatalyst and the transferred electrons in Pt participate directly in water oxidation reaction at potentials significantly higher than that under dark due to developed photovoltage. Meanwhile, photogenerated holes in Si are blocked by a high Schottky barrier at the junction between Si and Ti and flow to the back-contact. Figure 5.6 (d)-(f) exhibit J_{photo}-V curves of MS and MIS samples with pl, pt and rpt bimetal layers, respectively and inset show their J_{dark}-V curves while figure 5.6 (c) exhibits the PEC performance parameters of MS and MIS samples as a function of bimetal layer design. The pl samples in both MS and MIS structures had the highest J_{dark} values while pt and rpt samples indicated almost zero. As mentioned earlier, this is because the carriers generated by catalytic reactions of Pt with the electrolyte can slip through the opening in the pt and rpt designs resulting in almost zero dark current. However, even though identical bimetal layers were deposited, J_{dark} value of MS-pl sample was much bigger than that of MIS-pl. It has been reported that MIS structure in photovoltaic cells has lower J_{dark} than MS structure without decreasing J_{photo} values because the insulator lowers thermionic emission of the extra majority-carrier current path[20, 21]. In both MS and MIS contacts, V_{os} values of pt samples had superior than that of rpt design due to wider metal covered area on the potential drop and band bending at the junctions. In spite of equal bimetal layers used, V_{os} values of MIS samples were much improved than those of MS samples and hence $J_{V=0}$ values were also greatly enhanced. In comparison with MS, the insulating layer in MIS blocked injection of majority carriers into metal layer, suppressed

surface recombination by tunneling of electron transfer and hence produced higher internal voltage (V_{os}) and much improved current flow at low or moderated applied bias[22]. Also, the resistance of Si Schottky contacts can be considerably lowered by the thin insulating layer leading to enhanced J values[23, 24].

However, at more negative bias, J values of MS samples were much higher than that of MIS samples while as the opening in the bimetal layer designs increased, the differences of J_{sat} between MS and MIS decreased and subsequently MIS samples in rpt had higher J_{sat} value. There is a larger probability that photo induced carriers reach first the space charge layer under the metal collectors than in the remaining non-covered surface, where photo-induced electrons can recombine at interface states[19]. Nonetheless, compared to that of MS sample, higher J_{sat} value of MIS sample in rpt design demonstrated good quality of the insulating layer in MIS samples. Also, the decreased differences of J_{sat} between MS and MIS with opening of bimetal designs as well as superior J_{sat} value of MIS-rpt can be explained by the lateral transport of photogenerated electrons at highly negative bias[10]. It is well known that recombination within the inversion layer in MIS photovoltaic cells can be considerably suppressed[9, 25]. An electrolyte-induced inversion layer can be formed near the SiO_2/Si interface at highly negative bias which results in long-distance lateral collection of photogenerated electrons due to significantly reduced recombination within the inversion layer. Moreover, we expected that pt design allowed higher J_{sat} values than in pl samples due to larger light absorption of Si. Curiously, however, for both MS and MIS structures, pl samples indicated better J_{sat} values. With very large overpotential, the back reactions of separated carriers were alleviated but the transportation/transfer was accelerated. Consequently, for

both MS and MIS contacts, pl samples indicated larger J_{sat} than that of pt samples implying pl design produced extra carriers by thermionic emission at a high overpotential as well as by catalytic reactions of Pt. Similarly, at an extremely overpotential, compared to MIS, higher J_{sat} values of the MS samples in both pl and pt designs created by spare carrier generations via thermionic emission showing very poor fill factor.

To compare stability properties of MS vs MIS contacts with different bimetal designs like pl, pt, and rpt, we carried out J-t measurements at V = 0 V vs. RHE for 30min (Figure 5.6 (g)-(i)). In pl design, both MS and MIS samples show good stabilities because whole metal covering can block Si exposure to electrolyte. However, the high resistance of pl design causes cell performance degradation, particularly in MS structures indicating more reduction of J. Meanwhile, as opening of bimetal designs increased from pt to rpt, stabilities of both MS and MIS samples became worse implying that the insulating layer in MIS was not perfect but good enough to work. Specially, MS-rpt sample revealed 36.2 % reduction of J value, which is two times higher than MIS-rpt demonstrating very thin insulating layer in MIS can protect Si from oxidation reactions with electrolyte well. Interestingly, J value of MIS-pt sample first increased then decreased thus after 30min test, overall a little bit higher J was obtained than initial value. Further experiments are necessary to investigate the reason for the improvement of J in pt design.

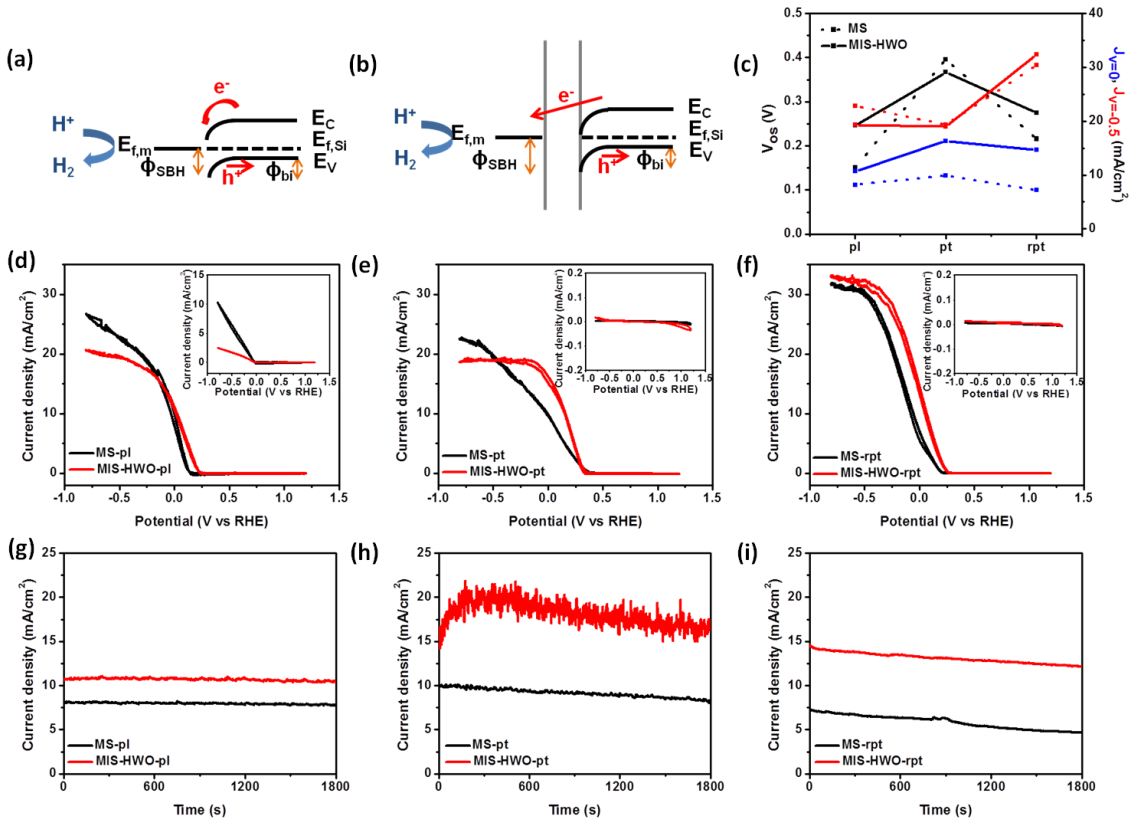

Figure 5.6 Energy band diagrams of MS (a) and MIS (b) structures, J-V curves and stability properties of both MS and MIS structures with pl (d, g), pt (e,h) and rpt (f, i) and PEC performance parameters curves of MS and MIS samples as a function of different metal designs.

5.3.3 Effects of different bimetal ratio (Pt/Ti) in MIS structures with different metal layer designs

Pt has been shown to provide the highest electrochemical activity toward the HER while it has a cost issue and low photovoltaic property due to high work function. Therefore, it is important to reduce the thickness of Pt on the electrode and optimize bimetal ratio to develop a cost-effective and high efficient photoelectrodes. We further

investigated the effects of various metal ratio of electrolyte (Pt) and collector (Ti) in MIS structures with three bimetal designs on PEC performances as shown in Figure 5.7.

Regardless of different metal ratio of Pt and Ti, J_{dark} values decreased as opening portion of metal design increased due to less Pt amount for catalytic reactions as well as reduced carriers to be collected to back contact by slipping through opening. Also, as the total thickness of the bimetal layer increased, J_{sat} values in pl and pt designs gradually decreased but J_{sat} values in rpt designs were independent from the metal thickness due to large opening (86.6 %) implying that metal ratio is also an important factor in current flow as well as photovoltage (Figure 5.7 (c)). When Ti layer was much thicker than Pt layer, V_{os} values improved more for all bimetal design allowing $J_{V=0}$ to be enhanced because of low work function of Ti. However, at too thick bimetal layer like 20 nm Pt/30 nm Ti, the effects of low work function on PEC performance parameter such as V_{os} and $J_{V=0}$ values were offset by decreasing a large amount of light absorption of Si in pl and pt designs. Interestingly, there were not significantly differences of V_{os} and $J_{V=0}$ values in rpt samples between 5 nm Pt/8 nm Ti and 20 nm Pt/30 nm Ti because the amount of light absorption in Si was not much reduced due to large opening of rpt design, demonstrating that both V_{os} and $J_{V=0}$ values were deeply dependant on not only the amount of light absorption but also metal ratio effects.

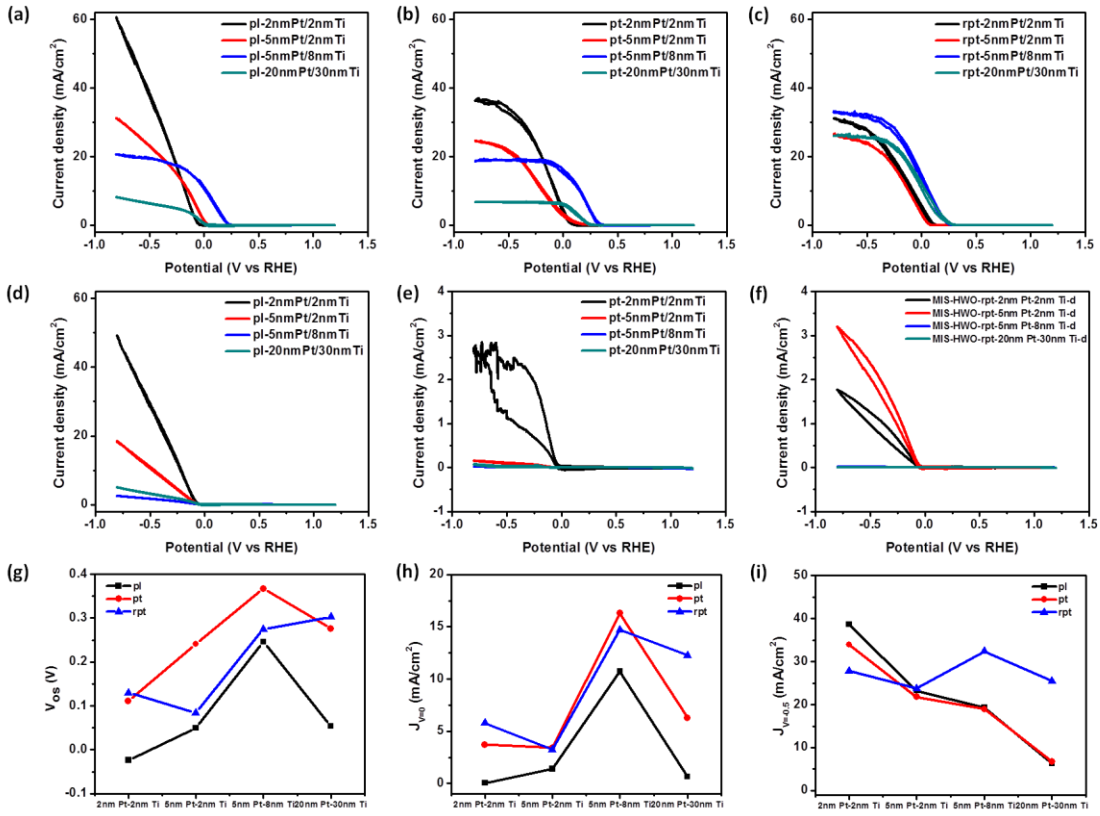

Figure 5.7 J-V curves of MIS structures with different types of insulating layer and metal design under dark (d-f) and illumination (a-c) and the trend of PEC parameters (g-i).

5.4 Conclusions

We developed cost-effective and high efficient Si-based photocathodes by introduction of MS and MIS structures with bimetal layer (Pt/Ti) and investigated the effects of structure/interfacial junction type on PEC performance parameters. Compared to other oxide layer, MIS-HWO samples exhibited the best PEC performances for all patterned structures in terms of $J_{V=0}$ and $J_{V=-0.5}$ demonstrating that the quality of HWO layer is the best. Compared to MS structures, MIS structures show much better PEC performances like lower dark current density, high photocurrent density, low on-set

potential and outstanding stability because the insulator lowers thermionic emission of the extra majority-carrier current path and also it blocked injection of majority carriers into metal layer, suppressed surface recombination by tunneling of electron transfer. In both MS and MIS contacts, while pt and rpt indicated almost zero J_{dark} values due to the opening which allows the carriers produced by Pt catalyst to escape toward electrolyte, large amount of Pt in pl developed carriers via catalytic reactions leading to the highest J_{dark} values. Compared to rpt design, pt samples had wider metal covered area which influences the potential drop and band bending at the junctions thereby superior V_{os} values. The lateral transport of photogenerated electrons at highly negative bias caused reduction of J_{sat} differences between MS and MIS as opening of bimetal designs increased, hence MIS-rpt indicated superior J_{sat} value. MIS structures with patterned bimetal layer will be further optimized by control of metal covering and patterning dimensions to enhance their PEC performances.

5.5 Note

This chapter, in full, is currently being prepared for submission for publication of Energy & Environmental Science. Sun Young Noh, Namseok Park, Li Chen, Zhaowei Liu, and Deli Wang. The dissertation author was the primary researcher and first author of this paper.

5.6 References

1. Hisatomi, T., Kubota, J. & Domen, K. Recent advances in semiconductors for photocatalytic and photoelectrochemical water splitting. *Chemical Society Reviews* (2014).

2. Walter, M.G., Warren, E.L., McKone, J.R., Boettcher, S.W., Mi, Q. Santori, E.A., and Lewis, N.S., Solar Water Splitting Cells. *Chemical Reviews* **110**, 6446-6473 (2010).

3. Bak, T., Nowotny, J., Rekas, M. & Sorrell, C.C. Photo-electrochemical hydrogen generation from water using solar energy. Materials-related aspects. *International Journal of Hydrogen Energy* **27**, 991-1022 (2002).

4. Lévy-Clément, C., Lagoubi, A., Neumann-Spallart, M., Rodot, M. & Tenne, R. Efficiency and Stability Enhancement of n-Si Photoelectrodes in Aqueous Solution. *Journal of The Electrochemical Society* **138**, L69-L71 (1991).

5. Sun, K., Park, N., Sun, Z., Zhou, J., Wang, J., Pang, X., Shen, S., Noh, S. Y., Jing, Y., Jin, S., Yu, P.K.L., and Wang, D., Nickel oxide functionalized silicon for efficient photo-oxidation of water. *Energy & Environmental Science* **5**, 7872-7877 (2012).

6. McKone, J.R., Warren, E.L., Bierman, M.J., Boettcher, S.W., Brunschwig, B.S., Lewis, N.S., and Gray, H.B., Evaluation of Pt, Ni, and Ni-Mo electrocatalysts for hydrogen evolution on crystalline Si electrodes. *Energy & Environmental Science* **4**, 3573-3583 (2011).

7. Scheuermann, A.G., Prange, J.D., Gunji, M., Chidsey, C.E.D. & McIntyre, P.C. Effects of catalyst material and atomic layer deposited TiO2 oxide thickness on the water oxidation performance of metal-insulator-silicon anodes. *Energy & Environmental Science* **6**, 2487-2496 (2013).

8. Lin, F. & Boettcher, S.W. Adaptive semiconductor/electrocatalyst junctions in water-splitting photoanodes. *Nat Mater* **13**, 81-86 (2014).

9. Hezel, R. Recent progress in MIS solar cells. *Progress in Photovoltaics: Research and Applications* **5**, 109-120 (1997).

10. Esposito, D.V., Levin, I., Moffat, T.P. & Talin, A.A. H2 evolution at Si-based metal–insulator–semiconductor photoelectrodes enhanced by inversion channel charge collection and H spillover. *Nat Mater* **12**, 562-568 (2013).

11. Ghosh, A.K., Fishman, C. & Feng, T. SnO2/Si solar cells—heterostructure or Schottky-barrier or MIS-type device. *Journal of Applied Physics* **49**, 3490-3498 (1978).

12. Wang, C.-Y. & Hwu, J.-G. Metal–Oxide–Semiconductor Structure Solar Cell Prepared by Low-Temperature ($< 400\,^{\circ}\mathrm{C}$) Anodization Technique. *Journal of The Electrochemical Society* **156**, H181-H183 (2009).

13. Dasgupta, N.P., Liu, C., Andrews, S., Prinz, F.B. & Yang, P. Atomic Layer Deposition of Platinum Catalysts on Nanowire Surfaces for Photoelectrochemical Water Reduction. *Journal of the American Chemical Society* **135**, 12932-12935 (2013).

14. Green, M.A. & Blakers, A.W. Advantages of metal-insulator-semiconductor structures for silicon solar cells. *Solar Cells* **8**, 3-16 (1983).

15. Palik, E.D. Handbook of Optical Constants of Solids. (Elsevier Science, 1985).

16. Rakic, A.D., Djuri?ic, A.B., Elazar, J.M. & Majewski, M.L. Optical Properties of Metallic Films for Vertical-Cavity Optoelectronic Devices. *Appl. Opt.* **37**, 5271-5283 (1998).

17. Noh, S.Y., Sun, K., Choi, C., Niu, M., Yang, M., Xu, K., Jin, S., and Wang, D., Branched TiO2/Si nanostructures for enhanced photoelectrochemical water splitting. *Nano Energy* **2**, 351-360 (2013).

18. Lewerenz, H.J., Skorupska, K., Muñoz, A.G., Stempel, T., Nüsse, N., Lublow, M., Vo-Dinh, T., and Kulesza, P., Micro- and nanotopographies for photoelectrochemical energy conversion. II: Photoelectrocatalysis – Classical and advanced systems. *Electrochimica Acta* **56**, 10726-10736 (2011).

19. Muñoz, A.G. & Lewerenz, H.J. Advances in Photoelectrocatalysis with Nanotopographical Photoelectrodes. *ChemPhysChem* **11**, 1603-1615 (2010).

20. Pulfrey, D.L. MIS solar cells: A review. *Electron Devices, IEEE Transactions on* **25**, 1308-1317 (1978).

21. Card, H.C. Photovoltaic properties of MIS-Schottky barriers. *Solid-State Electronics* **20**, 971-976 (1977).

22. Liu, C.P., Hui, Y.Y., Chen, Z.H., Ren, J.G., Zhou, Y., Tang, L., Tang, Y.B., Zapien, J.A., and Lau, S.P., Solution-processable graphene oxide as an insulator layer for metal-insulator-semiconductor silicon solar cells. *RSC Advances* **3**, 17918-17923 (2013).

23. Mönch, W. On the alleviation of Fermi-level pinning by ultrathin insulator layers in Schottky contacts. *Journal of Applied Physics* **111**, - (2012).

24. Green, M.A. Effects of pinholes, oxide traps, and surface states on MIS solar cells. *Applied Physics Letters* **33**, 178-180 (1978).

25. Beyer, A., Ebest, G. & Reich, R. Metal-insulator-semiconductor solar cells with silicon oxynitride tunnel insulator by using rapid thermal processing. *Applied Physics Letters* **68**, 508-510 (1996).

CHAPTER 6: Conclusions and Future Works

6.1 Summary

Solar energy conversion into storable and transportable chemical fuels via PEC water splitting cell is an attractive scientific and technological goal to address the increasing worldwide demand for energy and to reduce the impact of energy production on climate change. In order to build up economically competitive and highly efficient PEC water splitting cells, we selected suitable and cost-effective photoelectrodes, electrocatalyst or co-catalyst materials, and engineered and developed well-designed structures.

First, we prepared rutile TiO_2 NWs by hydrothermal method which is low cost fabrication process and further modified them by straightforward post growth-treatment methods like hydrogenation (forming gas (FG) treatment), atomic layer deposition (ALD), or their co-treatments to improve PEC performances of rutile TiO_2 NWs. FG treatment increased donor density (oxygen vacancies) in TiO_2 NWs leading to much higher IPCE value and J_{sc} and visible response. On the other hand, the additional ALD layer indicated two opposite effects like a protecting layer as well as a blocking layer. Consequently, even though they had improved J_{sc} and IPCE value, NW samples with ALD layer exhibited similar or smaller efficiency than those without ALD due to very low FF. Therefore, both types and sequences of post growth treatments should be carefully considered to improve the properties and performances of TiO_2 NWs.

Second, we fabricated core/shell nanowire (cs-NW) and three-dimensional branched nanowire (b-NW) structures with two low cost materials, TiO_2 and Si, to achieve increased surface area for enhanced light absorption and more reaction sites and short diffusion length of minority carriers for higher reaction rate. The TiO_2/Si b-NWs arrays noticeably improved the PEC performance compared to cs-NW arrays. IPCE study confirmed an operation of a two-photon-one-electron process model. Therefore, we concluded that photo current of TiO_2/Si heterojunction structure is limited by the recombination at the TiO_2/Si junctions or the properties of TiO_2.

Third, we developed cost-effective and efficient Si-based photoelectrodes employing MS and MIS structures with earth abundant and superior Ni electrocatalys. During PEC performance tests, the oxidized Ni layer was formed but it didn't deteriorate PEC performances due to its excellent conductivity and oxygen evolution catalytic properties. Compared to MS structures, both MIS-native and MIS-HWO structures indicated much better PEC performances like high photocurrent density, low on-set potential and outstanding stability because the insulator lowers thermionic emission of the extra majority-carrier current path and also it blocked injection of majority carriers into metal layer, suppressed surface recombination by tunneling of electron transfer. Although MIS-native structures exhibit much low dark current density and exceptional stability, MIS-HWO structures, except 2nm samples, indicate the best performances in terms of saturated current density values after stability test. These excellent performances of MIS samples can be further enhanced by optimized insulating layer quality.

Lastly, with bimetal layer (Pt/Ti), we also introduced MS and MIS structures for PEC photocathodes and investigated the effects of metal designs (planar (pl), patterned

(pt), reversely patterned (rpt)) and interfacial junction type on PEC performance parameters. Similar to photoanodes study, MIS-HWO samples exhibited the best PEC performances for all patterned structures in terms of $J_{V=0}$ and $J_{V=-0.5}$ demonstrating that the quality of HWO layer is the best in our system. Also, MIS structures had much better PEC performances compared to MS structures because of insulating layer effects. In both MS and MIS contacts, while pt and rpt indicated almost zero J_{dark} values, large resistance of pl thermally developed carriers leading to the highest J_{dark} values as well as poorer stability due to thermal cell degradation. Compared to rpt design, pt samples had wider metal covered area which influences the potential drop and band bending at the junctions thereby superior V_{os} values. The lateral transport of photogenerated electrons at highly negative bias caused reduction of J_{sat} differences between MS and MIS as opening of bimetal designs increased, hence MIS-rpt indicated superior J_{sat} value. MIS structures with patterned bimetal layer will be further optimized by control of metal covering and patterning dimensions to enhance their PEC performances.

6.2 Future work

There are several possible approaches to improve the PEC performances of photoelectrodes presented in each chapter, which are discussed in details below related to each of the chapters.

As presented in chapter 2, we modified rutile TiO_2 NWs by coating with same material by ALD method. Instead, coating with different materials like p-type NiO or CuO can make a pn junction which provides an internal voltage leading to fast charge separation thereby enhanced PEC performance of rutile TiO_2 NWs. Also, we can add co-

catalysts or plasmonic nanoparticles on the hydrogenated TiO_2 NWs to improve their PEC performances.

In chapter 3, we concluded that photo current of TiO_2/Si heterojunction structure is limited by the recombination at the TiO_2/Si junctions, or TiO_2 properties. Therefore, the post growth treated TiO_2 NWs, which show the improved PEC performances, can be applied to TiO_2/Si heterojunction structure for further enhancement. Also, the dimensions of Si NWs in multi-branched TiO_2/Si NWs can be easily changed by using different mask designs for the nanoimprinting process to prevent recombination possibility in such long Si NWs or limitation of TiO_2 NW growth. Hence, optimized dimensions are required to increase the PEC performances. Moreover, instead of n-Si, p-Si can be used to produce a pn junction giving an extra voltage for better charge separations.

In chapter 4 and 5, MS and MIS were employed to contacts to provide photovoltaic effects in PEC photoelectrodes. MIS junction properties can be further improved by optimizing silicon oxide layer quality or by using superior insulating materials like ultrathin Si_3N_4 layers. Also, to further improve PEC performances of MS and MIS structures, metal pattern dimensions should be optimized to suppress resistance and increase light absorption of Si substrate. Moreover, we can apply same MS and MIS junction into only Si NW or cs- TiO_2/Si structures fabricated in chapter 2. In case of cs-TiO_2/Si structure, ultrathin TiO_2 layer, which can be prepared by ALD technique, can be used as an insulating layer.

Furthermore, an embedded pn junction can be used for PEC photoelectrodes, which is similar to the concept of MIS, in terms of the coupling of water-splitting catalysts to silicon photovoltaics but possibly more practical and electrochemically stable.

This is because the fabrication of ultrathin and highly qualified insulating layer in MIS is challenging and pin holes of the thin oxide layer in MIS are possibly developed during PEC operation. Using transparent conductive oxide glasses for photoanodes with a buried pn junction has been demonstrated before[1, 2]. However, a traditional n-type TCO like FTO or ITO has a large hole effective mass and a low hole conductivity. Very recently, we reported a Si photoanode with a buried junction which is protected by an improved ITO layer with an intermediate metal, Au, and eventually catalyzed by an ultrathin NiO_x catalyst[3]. A stable semi-transparent ITO/Au/ITO hole conducting oxide layer, sandwiched between the NiO_x catalyst and the Si photoanode, is used to protect the Si from corrosion in an alkaline electrolyte, enhance the hole transportation, and provide a preactivation contact to the NiO_x catalyst. Although it is currently low, energy conversion efficiency can be much more improved by using an optimized Si pn junction with higher photovoltage and long wavelength response for device integration purpose. Also, instead of NiO_x catalyst, we can apply earth abundant transition metals, Mn, Fe, Co and Ni, for electrocatalysts, which have been demonstrated a high activity in alkaline conditions.

6.3 References

1. Cox, C.R., Winkler, M.T., Pijpers, J.J.H., Buonassisi, T. & Nocera, D.G. Interfaces between water splitting catalysts and buried silicon junctions. *Energy & Environmental Science* **6**, 532-538 (2013).

2. Pijpers, J.J.H., Winkler, M.T., Surendranath, Y., Buonassisi, T. & Nocera, D.G. Light-induced water oxidation at silicon electrodes functionalized with a cobalt oxygen-evolving catalyst. *Proceedings of the National Academy of Sciences* **108**, 10056-10061 (2011).

3. Sun, K., Shen, S., Cheung, J.S., Pang, X., Park, N., Zhou, J., Hu, Y., Sun, Z., Noh, S.Y., Riley, C.T., Yu, P.K.L., Jin, S., and Wang, D., Si photoanode protected by a metal modified ITO layer with ultrathin NiOx for solar water oxidation. *Physical Chemistry Chemical Physics* **16**, 4612-4625 (2014).